ABSTRACT

Title of dissertation:	MICROFABRICATED ELASTOMER TACTILE SENSORS FOR ROBOTIC FINGERTIP SYSTEMS
	Alexandros Charalambides Doctor of Philosophy, 2016
Dissertation directed by:	Associate Professor Sarah Bergbreiter Department of Mechanical Engineering

Tactile sensing is an important aspect of robotic systems, and enables safe, dexterous robot-environment interaction. The design and implementation of tactile sensors on robots has been a topic of research over the past 30 years, and current challenges include mechanically flexible "sensing skins", high dynamic range (DR) sensing (i.e.: high force range and fine force resolution), multi-axis sensing, and integration between the sensors and robot. This dissertation focuses on addressing some of these challenges through a novel manufacturing process that incorporates conductive and dielectric elastomers in a reusable, multilength-scale mold, and new sensor designs for multi-axis sensing that improve force range without sacrificing resolution. A single taxel was integrated into a 1 degree of freedom robotic gripper for closed-loop slip detection.

Manufacturing involved casting a composite silicone rubber, polydimethylsiloxane (PDMS) filled with conductive particles such as carbon nanotubes, into a mold to produce microscale flexible features on the order of 10s of microns. Molds

were produced via microfabrication of silicon wafers, but were limited in sensing area and were costly. An improved technique was developed that produced molds of acrylic using a computer numerical controlled (CNC) milling machine. This maintained the ability to produce microscale features, and increased the sensing area while reducing costs. New sensing skins had features as small as 20 µm over an area as large as a human hand.

Sensor architectures capable of sensing both shear and normal force sensing with high dynamic range were produced. Using this architecture, two sensing modalities were developed: a capacitive approach and a contact resistive approach. The capacitive approach demonstrated better dynamic range, while the contact resistive approach used more simple circuitry. Using the contact resistive approach, normal force range and resolution were 8,000 mN and 1,000 mN, respectively, and shear force range and resolution were 450 mN and 100 mN, respectively. Using the capacitive approach, normal force range and resolution were 10,000 mN and 100 mN, respectively, and shear force range and resolution were 1,500 mN and 50 mN, respectively.

MICROFABRICATED ELASTOMER TACTILE SENSORS FOR ROBOTIC FINGERTIP SYSTEMS

by

Alexandros Charalambides

Dissertation submitted to the Faculty of the Graduate School of the
University of Maryland, College Park in partial fulfillment
of the requirements for the degree of
Doctor of Philosophy
2016

Advisory Committee:
Associate Professor Sarah Bergbreiter, Advisor
Associate Professor Pamela Abshire, Dean's Representative
Professor Elisabeth Smela
Professor Hugh Bruck
Assistant Professor Ryan Sochol

Acknowledgments

This material was supported by the National Aeronautics and Space Administration (NASA) under National Robotics Initiative (NRI) award #NNX12AM02G.

Table of Contents

List of Tables

List of Figures

Chapter 1

Introduction

1.1 Motivation

In robotics, sensing the environment is a critical challenge to move towards smarter, more autonomous systems to aid human beings [10]. Using information such as touch, robots can respond to stimuli in a way which is safe [11] and perform more complex operations like fine grasping [12]. Tactile data is also useful in human-robot systems such as bionic gloves [13], prosthetics [14], and minimally invasive surgery [15]. By having a distribution of force or strain measurements on a human hand, for example, a robotic glove can be instructed to assist the human user for stronger grasping [13]. In another example, a tactile sensor on a robotic fingertip would be able to detect if an object was slipping from its clutch, which is especially important for NASA robots handling tools outside of the International Space Station [16]. However, these applications and other modern uses require a tactile sensor that has a flexible form factor in order to accommodate curved surfaces and withstand high strains (up to 20%) [17] .

Ideally, a flexible tactile sensor would be able to mimic the abilities of human skin [17], and a list of target properties based on [17, 18] are shown in Table 1.1. To achieve these performance metrics, a variety of notable tactile sensors have been developed that utilize polymer materials [19], capacitive [20] and resistive-based

Table 1.1: Target Properties for Tactile Sensing in Robots

Property	*Target*
Force Range	10 N
Force Resolution	50 mN
Force Accuracy	±10 mN
Spatial Density	1 mm spacing
Sensing Axes	3 (Normal and Shear)
Geometry	Thin (<500 µm)
Material	Compliant, Conductive ($\rho \leq 100\ \Omega \cdot \mu m$)
Electronics	Power <10mW, 1's of Wires
Bandwidth	>1 kHz

sensing [21], novel architectures for multi-axis sensing [22, 23, 24], and wiring and low level computation for integration with larger robot systems [25].

1.2 MEMS Tactile Sensors

A common approach to tactile sensing originates from the semiconductor industry. Using microfabrication techniques pioneered by silicon chip manufacturers, devices called microelectromechanical systems (MEMS) sensors can be created which have several attractive advantages with regards to tactile sensing. The most prominent factor is size; MEMS sensors can be small (less than 1 mm) and can therefore be implemented in a wide range of sensing applications [26]. Another advantage is batch fabrication; many sensors (greater than a thousand on a 4 in wafer) can be

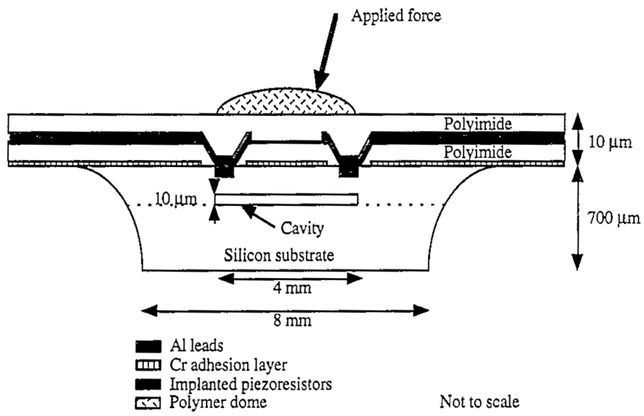

Figure 1.1: An early (1995) cavity-based MEMS normal force sensor. A diaphragm is compressed which elongates a silicon piezoresistor [1].

made at a time, reducing the overall cost of the sensor [26]. Silicon is also a good material for resistive-based sensing, and can be manufactured in serpentine shapes so that as it elongates or compresses the overall resistance increases or decrease, respectively [26]. Silicon can also be patterned to form interdigitated capacitors with electrode gaps that deform as force is applied [2]. Early work in tactile sensing used silicon or polysilicon suspended over a cavity or diaphragm, Fig. 1.1. More sophisticated systems embedded complementary metal-on-oxide (CMOS) circuits to combine both the sensor and signal processing into one package [27, 28, 29, 30], or bonded silicon sensors onto a printed circuit board, Fig. 1.2.

1.3 Conductive Polymers for Microfabrication

A primary challenge for MEMS sensors in robotics is integrating a silicon sensor, which is mechanically stiff and brittle, onto a curved surface [31]. For this reason, polymer MEMS has become an emerging field in the past 10 years and utilizes

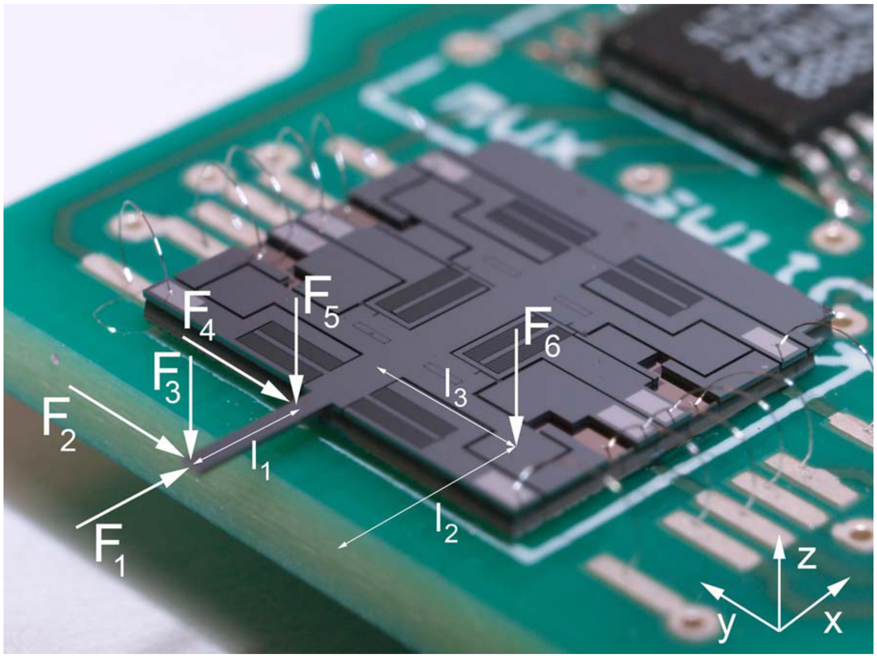

Figure 1.2: A 6-axis capacitive force/torque sensor packaged onto a PCB [2].

flexible silicones like polydimethylsiloxane (PDMS) or Ecoflex along with conductive filler particles like carbon nanotubes [32], exfoliated graphite [33], carbon black [34], silver nanowires [35, 36], or silver platelets [34] to create conductive polymer composites. Many examples exist which employ polymer composites in flexible applications including strain sensing on flapping wings [37], zipping dielectric elastomer actuators [38], and tactile sensors [4, 39]. When integrating conductive polymers with microfabrication processes, the composite is generally deposited as a thin film through a shadow mask [40], spray-coated through a stencil [32], transfered through microcontact printing [41], or patterned via lift off [24].

1.4 Transduction Methods

1.4.1 Resistive Sensing

Resistive sensing operates by passing a current through a strip of material with a known resistance, and measuring the change in resistance as deformation is applied. This apporach is most commonly used in strain sensing. Changes in resistance can be caused by a change in the material's resistivity (i.e., piezoresitivity), a shape change of the sensor geometry, or even by a sliding contact (i.e., potentiometer). Strain gauges made of semiconductors like silicon are dominated by piezoresistivity and are useful for sensing small strains (<1%), while strain gauges made of metals tend to be dominated by geometry effects. In a potentiometer, displacement causes a contact to slide across a resistive material, so that the distance between terminals shortens or lengthens effectively changing the resistance.

Polysilicon and metallic resistive strain gauges are a popular architecture for strain sensing due to their simple design and reliability [42, 43]. Strain gauges can be as simple as single strips of material, or serpentine geometries for enhanced sensitivity. These geometries have low cross talk across out-of-plane sensing directions due to the orientation of the serpentine structure [44], and due to a low Poisson's ratio (0.2 - 0.3) that limits out-of-plane deformation. However, silicon strain gauges are rigid and are difficult to incorporate onto flexible objects.

In the domain of flexible sensors, there exists a group of resistive pressure sensors which employ microfluidic channels filled with a conductive liquid, such as eutectic gallium-indium (eGaIn), which measure a change in resistance as the

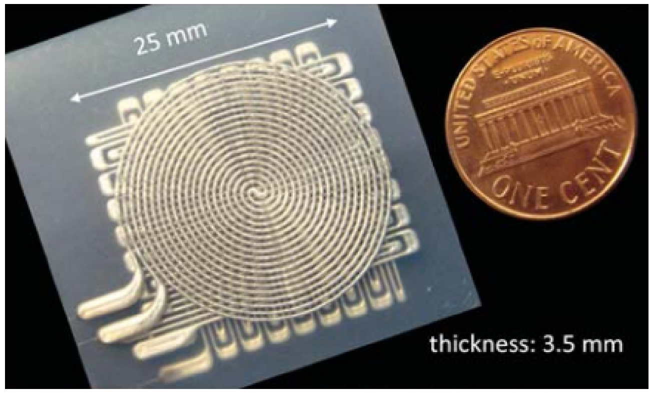

Figure 1.3: An eGaIn-based normal force tactile sensor. As the microfluidic channels are compressed, the channel area decreases which increases its electrical resistance. [3].

channels compress [45, 3]. Microchannels can have diameters ranging from 10's to 100's of μm, and can be configured in various shapes, like spirals or serpentines, Fig. 1.3, depending on the sensor application. However, eGaIn-based pressure sensors are too large to be used for fingertip-scale sensing, and are potentially dangerous due to the corrosivity of eGaIn on human eyes and skin.

Other approaches utilize conductive polymers as the piezoresistive material [37, 21]. Latex mixed with exfoliated graphite and stenciled into rectangular strips demonstrated strain resolution on the order of 100's of microstrain up to 2% compressive and tensile strain [37]. Higher strains have been shown to result in resistance hysteresis in several conductive polymers [33, 46, 39]. Although the sensors in [37] are larger scale (5 mm by 4 cm), the fabrication method has the added benefit of sensors being directly created onto the wing surface to minimize delamination. A fingertip-scale tactile sensor was developed using serpentine structures of carbon nanotubes at the base of PDMS bumps but had limited sensing area [21].

1.4.2 Capacitive Sensing

Capacitive sensing is another common modality for tactile sensing, and is widely utilized in polymer MEMS sensors [15]. This modality is employed by placing two electrodes in a strategic fashion such that when the sensor mechanically deforms, the electrode gap or area of overlap changes causing a change in capacitance. Knowing the mechanical properties of the electrode and gap materials, the change in capacitance can be related to force applied [47]. Many published capacitive tactile sensors utilize two parallel plates oriented normal to the direction of applied force. As a force is applied, the sensor compresses, the parallel plate gap decreases, and the capacitance increases according to a parallel plate model, Eq. 1.1,

$$C = \varepsilon_r \varepsilon_0 \frac{A}{g} \tag{1.1}$$

where C is capacitance, ε_r is relative permittivity, ε_0 is the dielectric constant, A is plate area, and g is the gap between the plates. Since C is inversely proportional to g, a small g is desired to maximize sensor sensitivity. For example, if a parallel plate capacitive sensor undergoes 10 µm of deformation, a gap change from 20 µm to 10 µm results in a larger change in capacitance than a sensor whose gap changes from 120 µm to 110 µm, and therefore results in a larger sensitivity.

Capacitive sensors are typically fabricated utilizing MEMS processing to achieve high sensor area density and low cost per sensor [17]. However, electrodes are usu-

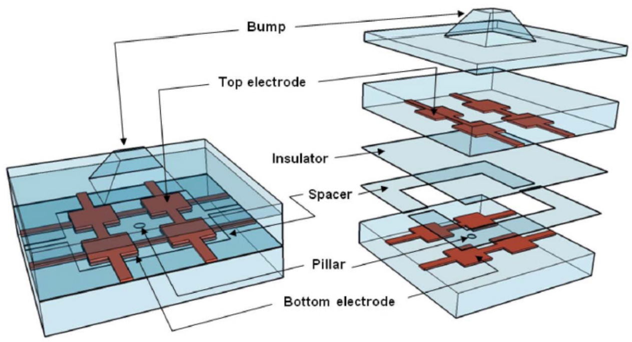

Figure 1.4: A flexible normal and shear tactile sensor, which utilizes arrays of parallel plate capacitors coupled with a "bump" layer to induce unique modes of deformation [4].

ally made of metal which hinders sensor compliance [20, 22]. A multi-layered design with air-gap capacitors demonstrated a shear and normal force resolution as low as 2.5 mN, but was limited to a 10 mN force range due to the collapse of the air-gap, Fig. 1.4 [4]. By increasing the air gap size, the force range can be improved up to a factor of 4 [22]. In piezoresistive sensing, wiring to sensors is often subject to the same applied pressures and strains as the sensors which can cause false readings; capacitive sensing can be used to minimize this complication. However, the wiring to the capacitive sensors is susceptible to parasitic capacitance (i.e., interference from the environment), and a shielding layer is important to mitigate this [48].

1.4.3 Optical Sensing

Optical sensing is another popular modality of force sensing especially within the medical community [49, 50, 51], specifically due to its ability to be integrated with magnetic resonance imaging (MRI). MRIs use a strong magnetic field, and ferrous materials within the MRI machine distort the images produced. Optical sensing can be accomplished using nonferrous equipment, like fiber optic cables and titanium or brass components, that don't interfere with the imaging process. Optical sensing operates by firing photons at a reflective material, which deforms as a force is applied, and then measuring the returning light intensity or waveform (i.e., interferometry). For a single fiber, as the distance between the fiber and reflective material decreases, the light intensity increases. Multiple fibers can be integrated into a scheme to produce multiple degree of freedom (DoF) sensors, Fig. 1.5.

Several optical sensors for minimally invasive surgery (MIS) with MRI compatibility have been demonstrated. A 2-DoF torque and 1-DoF force sensor has been demonstrated with a force sensing range of 0-20 N with sub-mN resolution [52]. A 6-DoF optical sensor was developed for brain surgery [53], but suffered from large hysteresis. Another 2-DoF optical sensor for haptic feedback was developed [54]. This particular device was not meant for MIS, but rather a tool for neuroscientists; patients undergoing an MRI and would be asked to manipulate the robot, so that a relationship between brain activity and motor control could be established. Similar research recently published involved an MRI compatible cello with optical sensing to record the notes being played while a musician underwent an MRI [55]. Arrays of normal force sensors consisting of urethane foam were developed using optical sensing [25], which were modular and could easily be rearranged depending on the application. However, the foams suffered from hysteresis when subject to pressures as low as 50 kPa.

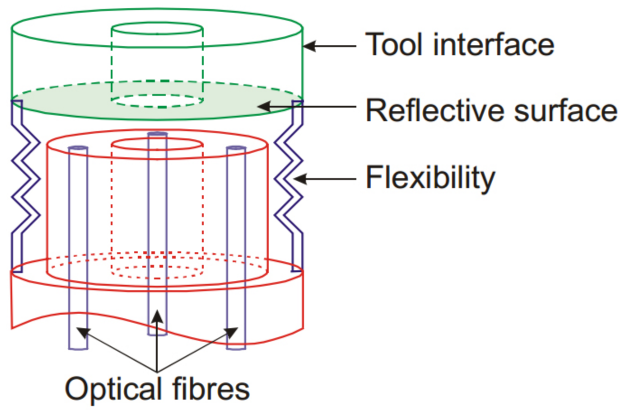

Figure 1.5: Working principle behind multi-DoF optical sensing: three fiber optical cables reflect photons off of a deformable material, and the intensity of the reflected light is used approximate the applied force [5].

1.5 Shear Force Sensing Approach

Shear force sensing is an important feature in detecting incipient slip [56]. Among the polymer-based piezoresistive and capacitive sensors, there exist several notable examples which were able to achieve not just normal force sensing but shear force sensing as well. Carbon nanotubes were patterned in serpentine shapes, and placed in groups of 2 x 2 arrays; for each array, a PDMS bump was placed on the outer most layer to induce predictable changes in resistance when subject to shear forces [24]. PDMS bumps are a popular technique among multi-axis polymer tactile sensors [19, 20, 22, 21, 23]. However, this technique requires multi-layer assembly and increases the fabrication complexity. Bumps can also be made of a more rigid material than the substrate, risking feature delamination [23]. In another design, four metallic serpentine strain gauges were fabricated on a polymer substrate and were also covered with a PDMS bump [19]. High sensor density was achieved, with sensors spaced every 2 mm. Recent work with the highest dynamic range so far reported used piezeresistive sensing of carbon nanotubes patterned around PDMS bumps [21]; shear force range and resolution were 500 mN and 25 mN, while normal force range and resolution were 5000 mN and 150 mN, respectively.

1.6 Robotic Applications

There has been considerable work integrating tactile sensors into robotic systems [57, 58, 59]. A common challenge in these systems is the large amount of wiring needed to interface the sensors with the microcontroller [60]. An anthropomorphic robotic hand for grasping, the Gifu II, was outfitted with 624 tactile sensors covering the fingers, palm, and back of palm with a bandwidth of 1 kHz but had hundreds of wires [61]. Systems often simplify and use 1-3 normal force sensors on each finger, but are unable to detect slip or location with millimeter accuracy [62]. Ideally, local processing could be nearby the sensors in order to reduce wiring and system level complexity as demonstrated in [63]: A human-worn glove with piezoresistive silver fabrics utilized small PCBs wrapped in a wrist band for local signal processing to minimize wiring. Another challenge is detecting slip of a grasped object. Algorithms for detection of incipient slip have focused on the signal response of a normal force sensor during slip, and have also utilized finely tuned geometric ridges to induce predictable sensor response [64].

Ultimately, a mechanoreceptive skin for a robotic hand capable of detecting slip and contact location is desired. To achieve this, there is a need to design a sensor using entirely flexible materials, which can sense normal and shear force over a large area, can be manufactured with high areal density similar to a fingertip, and can be easily integrated into a system for incipient slip detection.

1.7 Dissertation Organization

The remaining chapters are organized as follows:

2. Microfabrication of a new all-elastomer capacitive sensor for normal force detection, including a basic analytical model with experimental validation

3. Finite element modeling, microfabrication, and characterization of another new all-elastomer capacitive sensor for both shear and normal force sensing with high dynamic range

4. Novel manufacturing of a large area skin with 3-axis sensing, and demonstration of slip detection in a closed-loop robotic gripper

Chapter 2

Normal Force Sensing

This chapter presents the first step towards a novel flexible tactile sensor; this is the first sensor of its kind to utilize in-plane conductive elastomer capacitors and enables nonplanar electrode geometries. A basic linear model is presented along with comparison to experimental data. This work was presented at the IEEE Sensors 2013 conference in Baltimore, MD [65]. Additional experimentation was carried out, and is accompanied by a nonlinear analytical model developed by Kalayeh et. al. This work has been accepted to the IEEE Sensors Journal [7], and is currently in revisions as of May 2016.

2.1 Introduction

Tactile sensing in robots has been a topic of growing interest due to the need for increased dexterity to interact safely with humans and other objects [66, 67, 68, 18]. Effective grasping of soft objects, including people, in home-care or medical contexts requires knowledge of the forces that the robot is applying to the object [69]. Safe interaction between humans and robots working together on manufacturing tasks requires better knowledge of contact and proximity [70, 71].

Previous research in tactile sensing has yet to come close to emulating the sensing and integration of human skin [67, 18]. MEMS offers the possibility of future integration with CMOS for local signal processing as well as the advantages of batch fabrication and high spatial resolution (< 1 sensor/mm^2). Elastomers provide the sensor compliance and conformability necessary for curved surfaces such as robotic fingers. Capacitive sensing is less affected by resistive hysteresis seen in previous elastomer-based tactile sensors [72], since resistance isn't used as the sensing modality. Previous research has shown that capacitive tactile sensors can been fabricated using spray-on carbon nanotubes embedded in elastomer, but these sensors were larger (millimeters in size) and lacked high force sensitivities [73].

In this work, the above challenges were addressed using an all-elastomer batch fabrication process based on work by Gerratt [74]. This fabrication process orients capacitive sensors in-plane so that capacitor plates are vertical. As a result, non-planar electrode geometries can be easily fabricated and used to increase the net interface area, thus improving capacitance and force sensitivity.

2.2 Sensor Design

2.2.1 Reduced Order Solid Mechanics Model

A schematic of a single sensor is shown in Fig. 2.1. A rectangular sensor geometry that undergoes a uniform compressive stress will compress in the direction of the applied force and expand perpendicularly to the applied force as governed by Poisson's ratio. By modeling the deformation of the dielectric in between the capacitor, based on [75], a relationship between applied pressure and change in capacitance can be established. For a linear isotropic material under compression, where the

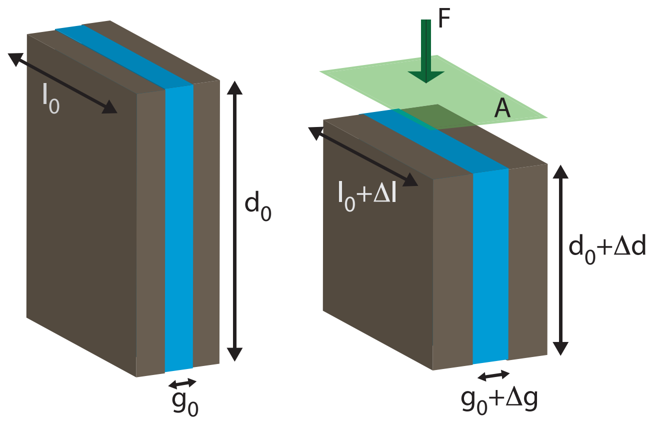

Figure 2.1: Applied pressure compresses and expands the sensor, resulting in a decrease in capacitance across the electrodes.

Z-axis is in the compression direction, the relationship between the three Cartesian strains is given by,

$$\epsilon_x = \epsilon_y = \nu\epsilon_z \tag{2.1}$$

The deformed dimensions of the dielectric are therefore,

$$l = l_0 + \Delta l = l_0(1 + \nu\epsilon_z) \tag{2.2}$$

$$g = g_0 + \Delta g = g_0(1 + \nu\epsilon_z) \tag{2.3}$$

$$d = d_0 + \Delta d = d_0(1 + \epsilon_z) \tag{2.4}$$

where l_0, g_0, and d_0 are the length, gap (or thickness), and depth of the dielectric, respectively. From the flat plate capacitance equation, the initial capacitance is given by,

$$C_0 = \epsilon_0 \epsilon_r \frac{l_0 d_0}{g_0} \tag{2.5}$$

where ϵ_0 and ϵ_r are vacuum and relative permittivity, respectively. The deformed capacitance is given by,

$$C = \epsilon_0 \epsilon_r \frac{ld}{g} \tag{2.6}$$

$$= \epsilon_0 \epsilon_r \frac{l_0(1+\nu\epsilon_z) d_0 (1+\epsilon_z)}{g_0(1+\nu\epsilon_z)} \tag{2.7}$$

$$= \epsilon_0 \epsilon_r \frac{ld}{g}(1+\epsilon_z) \tag{2.8}$$

Therefore the change in capacitance is given by,

$$\Delta C = C - C_0 \tag{2.9}$$

$$= \epsilon_0 \epsilon_r \frac{ld}{g} \epsilon_z \tag{2.10}$$

Lastly, for a linear elastic material under uniaxial compression, the relationship between stress and strain is given by,

$$\epsilon_z = \frac{\sigma_z}{E} = \frac{F}{EA} \tag{2.11}$$

where F is the applied force, E is the Young's modulus of the elastomer, and A is the area over which the force is applied. Combining the above two equations yields the relationship between applied force and change in capacitance,

$$\Delta C = \epsilon_0 \epsilon_r \frac{Fld}{EAg} \tag{2.12}$$

Although PDMS behaves hyperelastically and is incompressible ($\nu = 0.5$), this model describes behavior at low strains where behavior can be assumed to be linear. Sensor sensitivity is then defined as S,

$$S = \frac{\Delta C}{F} \tag{2.13}$$

In the case of a fabricated planar capacitor, where $l_0 = 1$ mm, $d_0 = 100$ μm, $g_0 = 10$ μm, $E = 1$ MPa, and $A = 2.5$ mm^2, a sensor sensitivity of 85 fF/N is predicted.

2.2.2 Fabrication Materials

Polydimethylsiloxane (PDMS) was selected as the bulk material due to its low modulus, which can increase electrode gap displacement as well as overall sensor conformability. In order to create a conductive elastomer, conductive filler particles were mixed with PDMS. Metallic filler particles were chosen over carbon used in previous work [76] to reduce the resistance of wiring to the sensors, although carbon can certainly be used in this process.

Silver nanopowder of 80-100 nm particle size (US Research Nanomaterials, Inc.) was mixed with 10:1 base to curing agent PDMS using a weight ratio of 72% silver, 28% PDMS (or 19% silver by volume). However, the mixture of the two proved too viscous to be mixed alone, therefore hexane was added at a ratio of 3 parts hexane to 1 part PDMS. The hexane would then be evaporated during the fabrication process under vacuum. Preliminary measurements showed resistivities

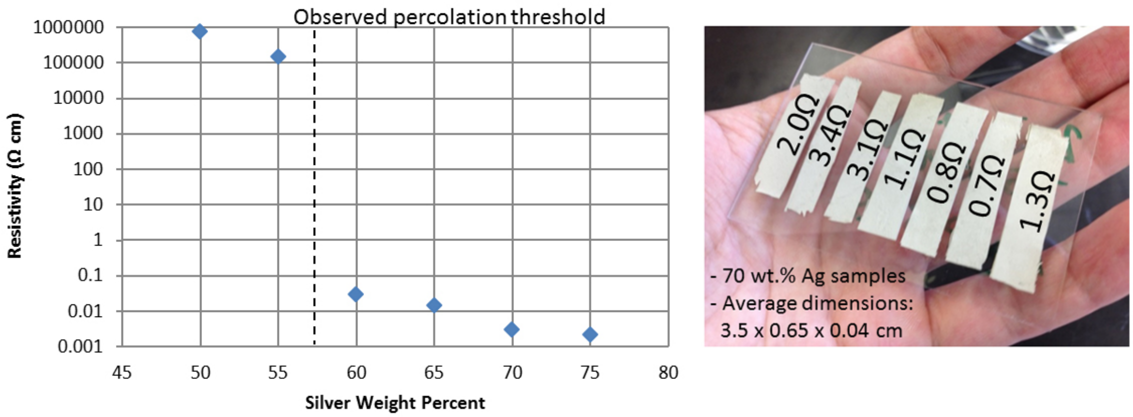

Figure 2.2: (Left) Material resistivity as a function of silver (particle size of 2-3.5 µm) weight percent in PDMS. (Right) 70 wt.% Ag/PDMS samples in-hand.

of 0.1 Ωcm, which was more than sufficient to avoid errors in capacitance measurements.

Larger silver micropowder was also investigated due to being more cost effective. Silver powder with a particle size of 2-3.5 µm was acquired from Sigma Aldrich (327085). A percolation threshold between 55 wt.% and 60 wt.% silver was observed, and resistivities below 0.01 Ωcm were observed above 65 wt.%, Fig. 2.2.

Both the nano and micropowders were difficult to mix with PDMS, and resulted in low yield during fabrication. This may have been due to silver's high mass density (about 4-5 times more dense than carbon) or due to its different surface chemistry (PDMS contains carbon, hence carbon powder may mix more favorably than silver). In the future, a conductive elastomer with higher yield than silver/PDMS and lower resistivity than carbon black/PDMS is needed.

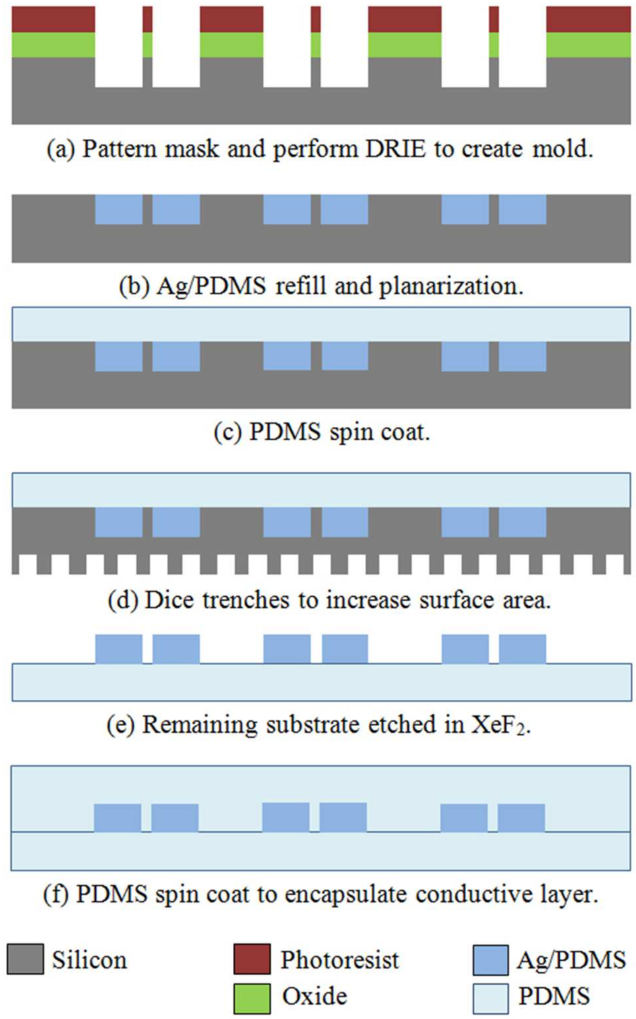

Figure 2.3: Microfabrication process used to create all-elastomer in-plane capacitors.

2.2.3 Microfabrication

The fabrication process shown in Fig. 2.3, based on [74], uses a silicon mold to pour and cure conductive and dielectric elastomers. The process requires a minimal number of fabrication steps and enables gaps down to 2 μm with 20:1 aspect ratios.

First, a 200 nm layer of oxide was deposited using plasma enhanced chemical vapor deposition on a bare silicon [100] wafer. Next, a 1.2 μm layer of photoresist was

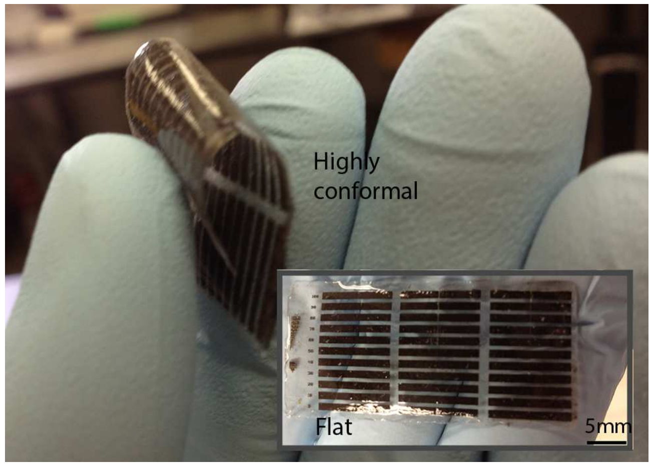

Figure 2.4: Completed tactile sensor in-hand. Resolution marks can be seen on the far left of the device [inset], while each black bar is a set of electrodes.

spin coated, masked, exposed, and developed. The oxide mask was then removed in fluorine plasma. A 100 μm deep reactive ion etch (DRIE) was used to create the silicon mold, and any remaining masking layers were removed. Upon completion of the mold, the Ag/PDMS mixture was poured over the wafer and vacuumed for 30 min to evaporate the hexane, remove air bubbles, and ensure the mixture was conformal to the mold. It was cured on a hot plate at 120°C for 15 min, and planarized using a razor blade. Next, PDMS was spin coated over the wafer at 500 rpm for 60 s to create a 150 μm layer. The wafer's unprocessed backside was diced to create trenches in order to increase surface area, and thus decrease etch time in the subsequent xenon difluoride isotropic silicon etch. Upon removal of the silicon, the backside was spin coated with PDMS in the same manner as the front to encapsulate the conductive elastomeric patterns.

A sample of some test sensors and a nonplanar electrode interface can be seen

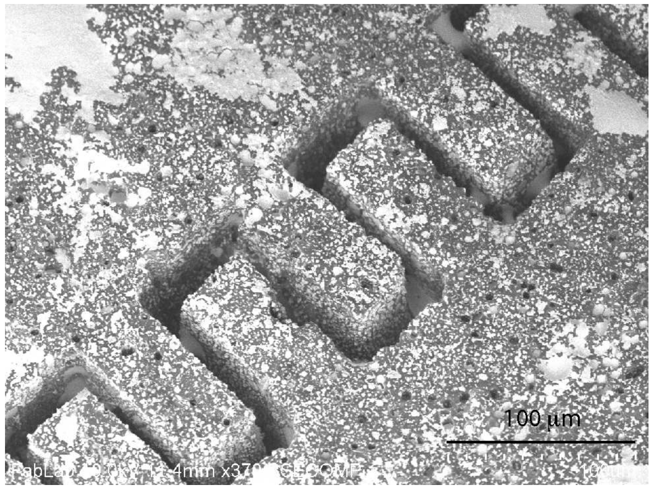

Figure 2.5: Scanning electron microscope (SEM) image of the "interdigitated" nonplanar electrodes.

in Figs. 2.4 and 2.5, respectively. The sensors can easily be wrapped around round surfaces. Using calipers, the total device thickness was found to be 400 μm. This fabrication process was able to produce features as small as 10 µm with aspect ratios of 10:1, Fig. 2.6.

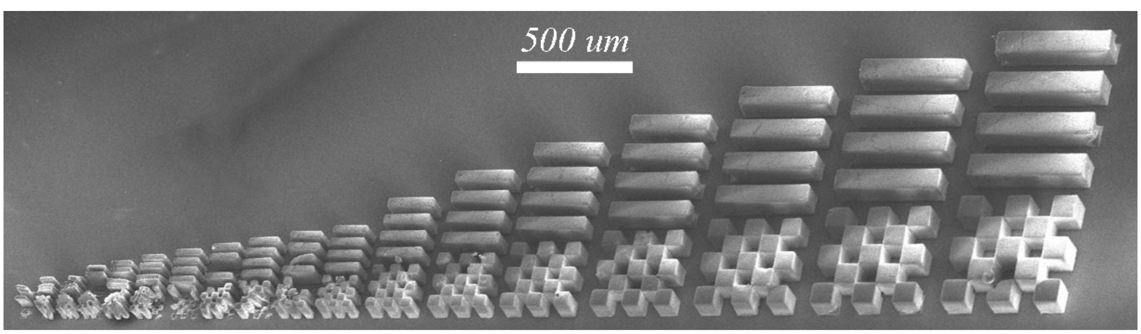

Figure 2.6: SEM image of the resolution marks. Ag/PDMS features as small as 10 µm were fabricated with aspect ratios of 10:1.

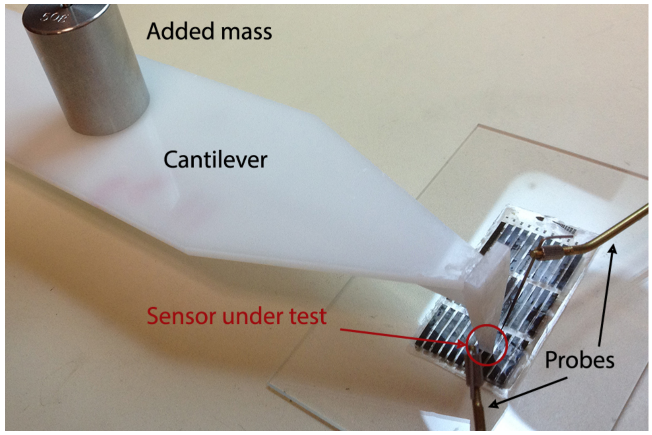

Figure 2.7: Tactile sensor test setup using a rapid prototyped beam, weights, and an Analog Devices evaluation board (only probes present in figure).

2.3 Sensor Performance

2.3.1 Test Setup

In order to apply a controlled load over a known area, a beam of Delrin was rapid prototyped using Creo (formally Pro/Engineer) and a desktop laser cutter (Versalaser 3.50 60W). To apply the load, a known mass was placed at the center of the beam so that half of the mass was transferred to the beam tip, which had a fabricated area of 2.5 mm^2. The beam tip was centered over the electrode interface, so that the entire interface was covered (Fig 2.7). Capacitance was then measured using an Analog Devices evaluation board (AD7745/46) by applying the board probes to each electrode. Testing was conducted for a range of electrode gap sizes (10, 50, and 100 μm) and weights. One limitation of the test setup was the minimum weight that could be applied, the force of the stand-alone beam (113 mN).

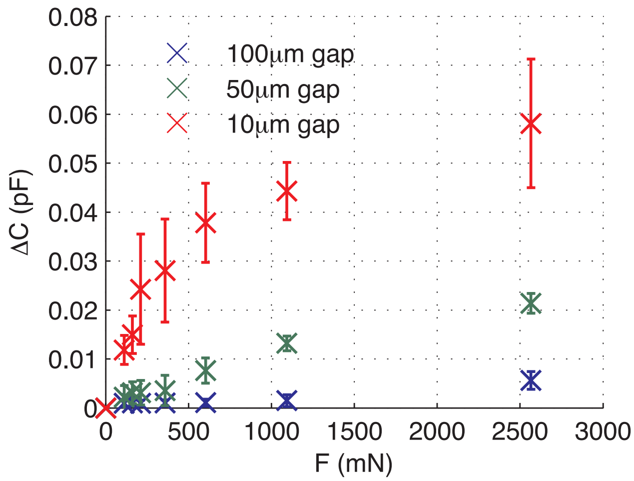

Figure 2.8: Change in capacitance as a function of force applied for flat plate capacitors of various dielectric gaps. Standard deviations are computed for 6 tests of the same sensor.

2.3.2 Results

Planar "flat plate" capacitors of various electrode gaps were tested up to approximately 2500 mN (Fig. 2.8). As electrode gap decreased, the sensor sensitivity increased, with the 10 μm gap being most sensitive. After sufficient loading, a decrease can be seen in sensitivity, and is most prominent in the 10 μm gap. This may be due to the hyperelastic behavior of the PDMS, as well as the material reaching a saturated state in which it cannot compress further.

A linear region was observed below 350 mN, corresponding to 15% strain (assuming a 1 MPa modulus for the elastomer), as shown in Fig. 2.9. This region matched the linear-elastic predicted sensitivities of 8.5 fF/N, 17 fF/N, and 85 fF/N for the 100 μm, 50 μm, and 10 μm gaps, respectively.

Cyclic testing of these "flat plate" sensors was conducted for two scenarios: a)

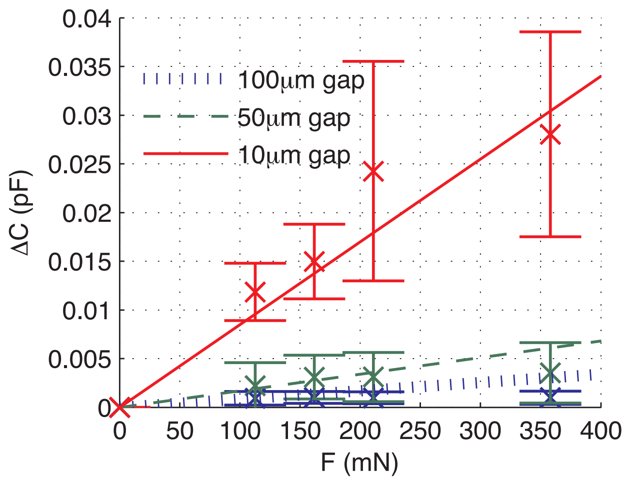

Figure 2.9: Linear region (less than 15% strain) of sensor behavior from Fig. 2.8. Lines are the analytical prediction for each electrode gap.

a fixed force of 358 mN applied to sensors with multiple gap widths (Fig. 2.10), and b) forces ranging from 358 mN to 2565 mN applied to a single sensor (Fig. 2.11). In both scenarios, sensor response times less than 0.1 s were apparent in all cases. For a fixed force, the 10 μm gap had the greatest change in capacitance, as expected. Similarly for a fixed gap of 80 μm, increasingly large forces increased the change in capacitance. Hysteresis could be seen upon the removal of a very large load (2565 mN), and resulted in a 7% decrease in initial capacitance after 4 cycles. Meanwhile, the capacitance while under load remained constant each cycle.

Lastly, Fig. 2.12 shows the response of a nonplanar interdigitated electrode (Fig. 2.5), with finger dimensions of 100 μm by 50 μm, and a uniform gap of 30 μm. Below 400 mN, a linear best fit of 1.1 pF/N was found, which is over an order of magnitude improvement in sensitivity when compared to the "flat plate" capacitor of 10 μm gap.

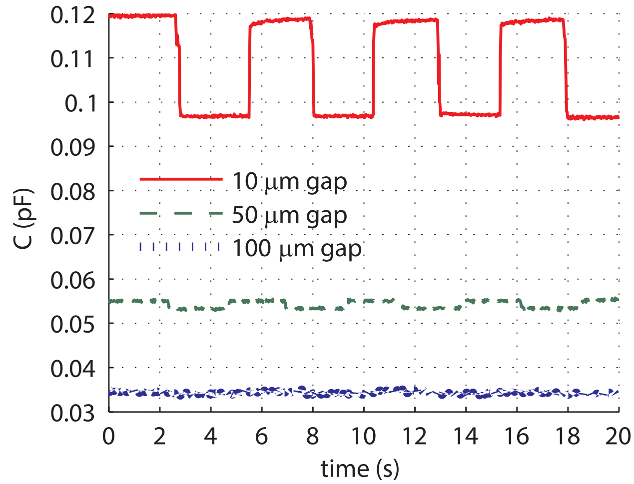

Figure 2.10: Capacitance as a function of time, where a 358 mN force was applied and removed repeatedly (all tests began with force removed).

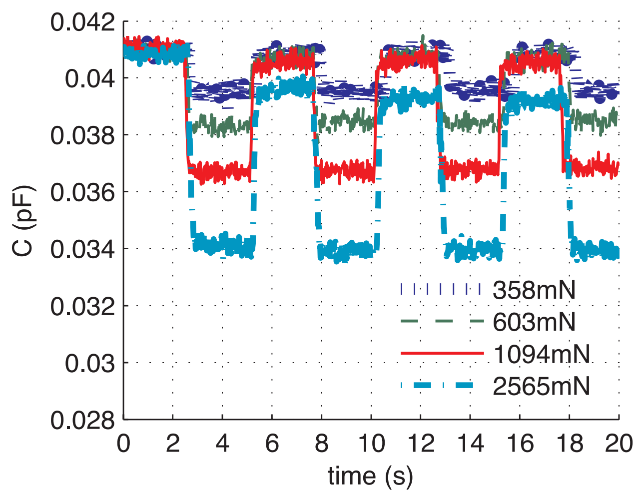

Figure 2.11: A flat plate capacitor of 80 μm gap was tested for a range of forces. Hysteresis can be seen for the highest load case. Signal noise is due to an accuracy of 0.4fF of the Analog Devices evaluation board.

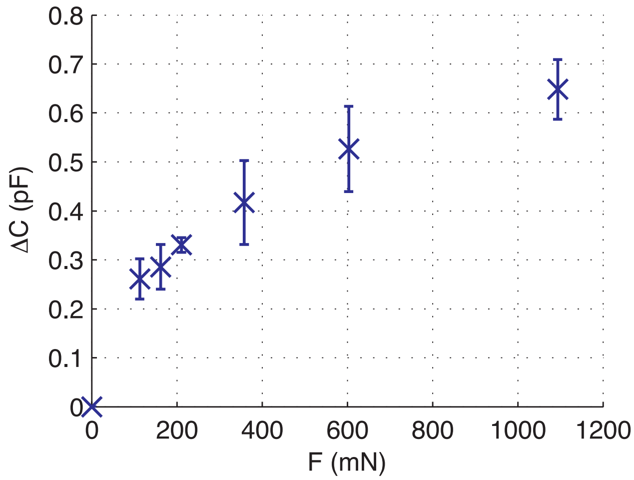

Figure 2.12: Load testing for a nonplanar “interdigitated” electrode interface, demonstrating a sensitivity over an order of magnitude greater than any planar “flat plate” electrode. Standard deviations are computed for 3 tests of the same sensor.

2.4 Improved Methods

2.4.1 Manufacturing

For the sake of manufacturing throughput, the fabrication process was modified to use silane as an anti-stick agent rather than etching away the mold in xenon difluoride, Fig. 2.13, and was able to yeild capacitors with gaps as small as 20 μm, Fig. 2.14. Silane is commonly used in the development of PDMS microfluidics [77] and was adopted in this work .

Using xenon difluoride to release the sensors from the silicon mold was not only a destructive (i.e., one time use) process, but also had the side effect of producing hydrofluoric acid (HF) [6]. After etching the mold with xenon difluoride, remnant

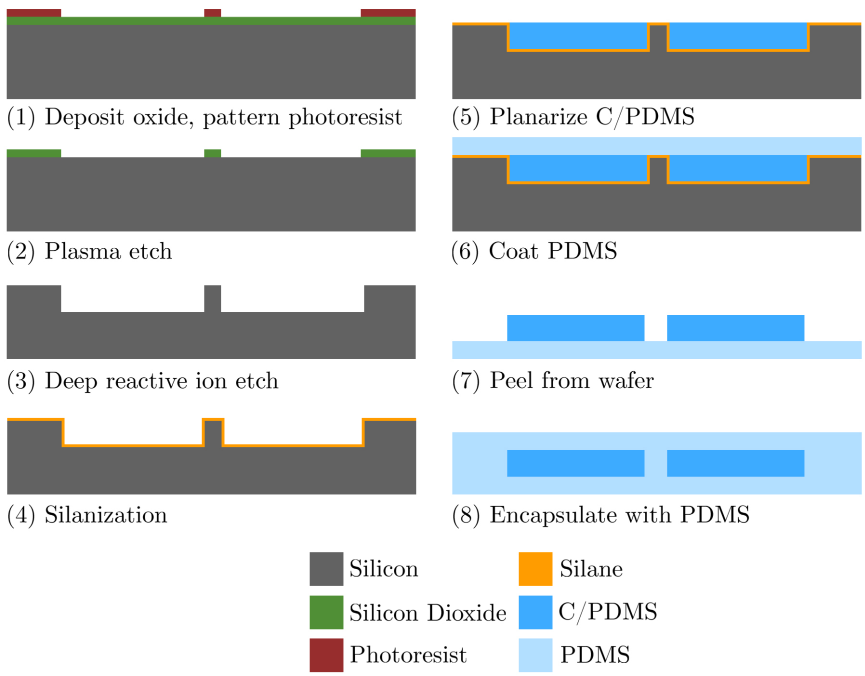

Figure 2.13: Updated microfabrication process with nondesctructive molding using silane as an anti-stick agent.

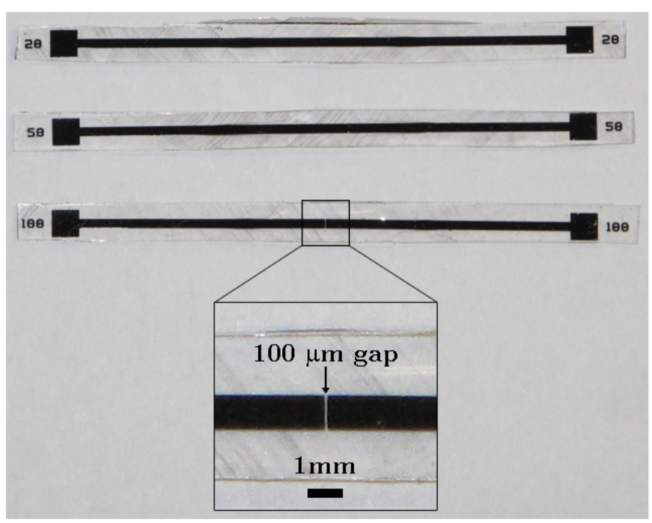

Figure 2.14: Macro photo of the normal force sensors using the updated fabrication process.

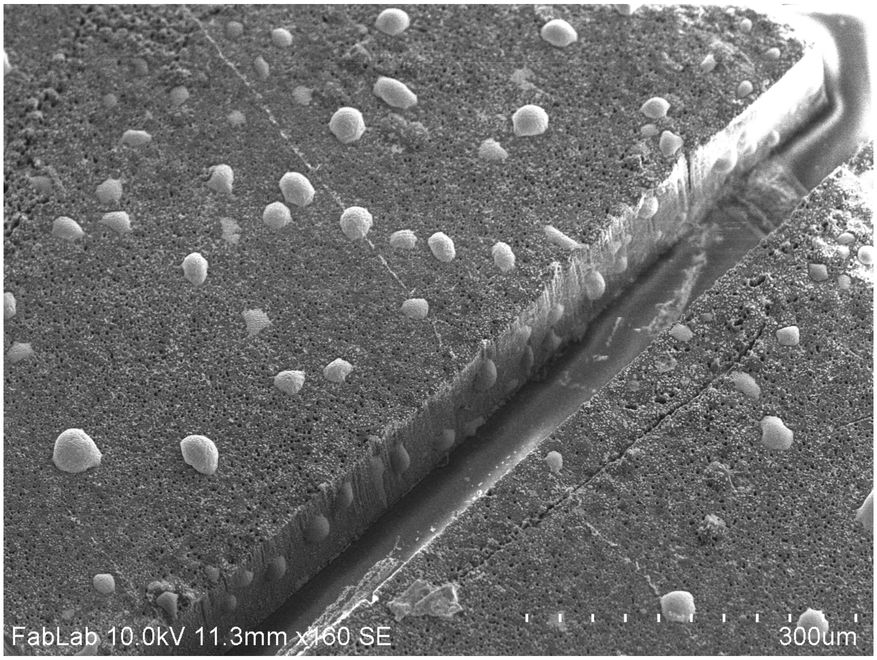

Figure 2.15: SEM image of droplets that formed on the Ag/PDMS sensor after being released from the silicon mold via xenon difluoride. The droplets were found to be hydrofluoric acid via a litmus test and EDS, and has also been seen in other work [6].

xenon difluoride became trapped within PDMS, which is porous to gases. As the PDMS was exposed to air, xenon difluoride interacted with moisture in the air to produce HF droplets. This was confirmed by a litmus test yielding a pH of less than 2, and through energy-dispersive x-ray spectroscopy (EDS) that revealed high concentrations on hydrogen and fluorine in the droplets, Fig. 2.15.

2.4.2 Test Setup

A more robust test setup was developed to minimize deviations between trials, Fig. 2.16, which utilized a Thorlabs stage and ATI force sensor to apply micron-

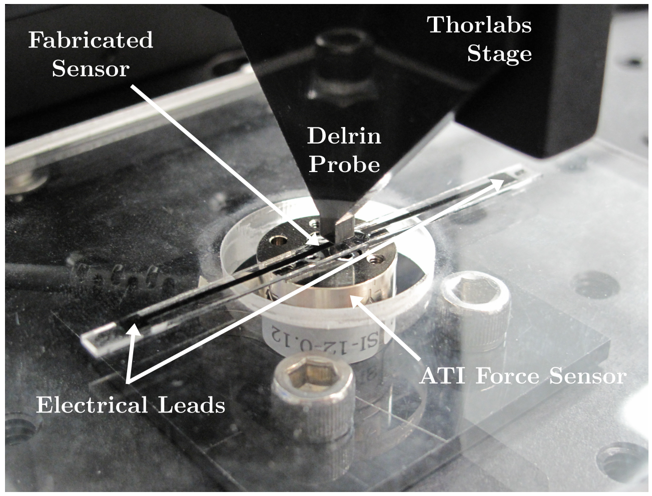

Figure 2.16: Thorlabs-ATI test setup for recharacterization of the normal force sensors.

scale displacements and sense mN to N forces, respectively. This avoided manual perturbations and inconsistencies due to loading and unloading the Delrin beam. The data was found to perform similarly to the trends previously collected, and had low deviations between trials, Fig. 2.17. A nonlinear analytical model was developed by co-authors Kalayeh et. al. [7], and was found to fit the experimental data.

2.4.3 Hysteresis Results

Cyclic loading of approximately 2250 mN of normal force was applied to the 20 µm gap sensor, Fig. 2.18. Testing was conducted by displacing the probe 25 µm into the sensor then pausing for 1 s, and repeating until 150 µm. Unloading was done in the same manner. This cycling process was carried out for 10 cycles, and each cycle took about 12 s. While testing, the pauses were necessary to sync capacitance and

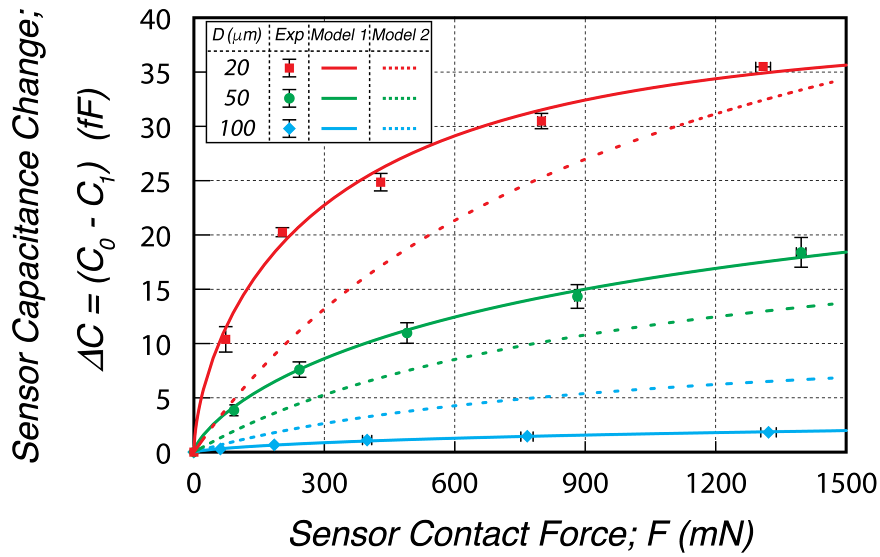

Figure 2.17: Updated data from various normal force sensors collected over 5 trials each. A nonlinear analytical model was developed by Kalayeh et. al. [7], and has a good agreement with the experimental data.

force data during post-processing.

The first cycle had a different loading curve than the remainder of cycles, as described by the Mullins effect [78], while after the sixth cycle the overall behavior followed a consistent path. Around 750 mN, the loading and unloading curves crossed indicating two distinct hysteresis domains. In the sub 750 mN domain, the unloading curve was above the loading curve which may be due to a larger dielectric gap during unloading. Above 750 mN, the unloading curve was below the loading curve which may be due to a smaller electrode height during unloading. The observed hysteretic behavior, similar to human skin, could be accounted for in a robotic system [79].

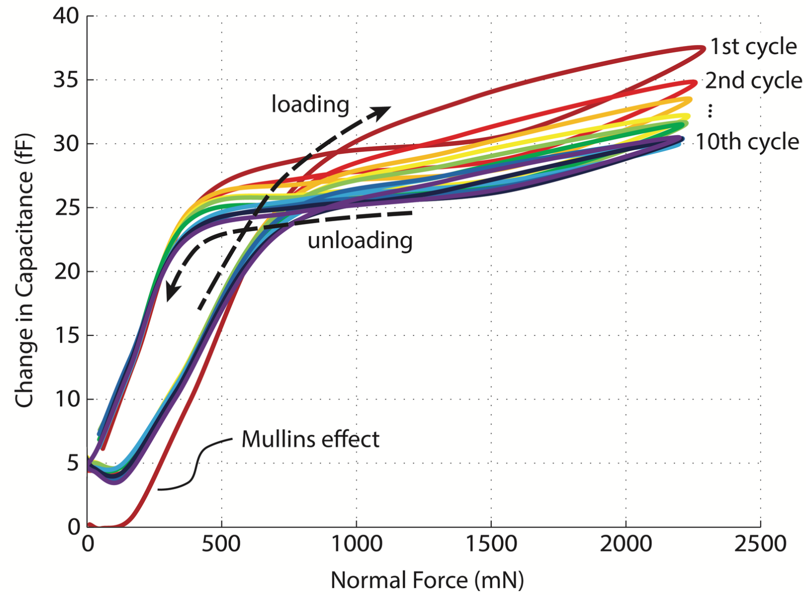

Figure 2.18: Hysteresis data obtained by applying cyclic loading of approximately 2250 mN of normal force to the 20 µm gap sensor.

2.5 Conclusions

An all-elastomer MEMS sensor was designed and fabricated to detect an applied normal force by measuring a change in capacitance. A new fabrication method using conductive and dielectric elastomers poured and cured in a silicon mold was developed, enabling in-plane capacitors as well as nonplanar electrode geometries for the first time. A reduced order model for planar electrode geometries was developed, and was accurate for strains below 15%, or approximately 400 mN. A nonlinear analytical model was also developed by co-authors Kalayeh et. al. Sensor sensitivities increased as electrode gaps decreased, as expected. Hysteresis testing exhibited two distinct behavior domains, and a marked Mullins effect after the first cycle. A nonplanar "interdigitated" electrode geometry showed an order of magnitude improvement in sensitivity over the planar “flat plate” capacitors, with a low strain linear best fit sensitivity of 1.1 pF/N.

Chapter 3

Shear and Normal Force Sensing

A novel all-elastomer MEMS tactile sensor with high dynamic force range is presented in this chapter. Conductive elastomeric capacitors formed from electrodes of varying heights enable robust sensing in both shear and normal directions without the need for multi-layered assembly. Sensor geometry has been tailored to maximize shear force sensitivity using multi-physics finite element simulations. A simple molding microfabrication process is presented to rapidly create the sensing skins with electrode gaps of 20 µm and sensor spacing of 3 mm. Shear force resolution was found to be as small as 50 mN and tested up to a range of 2 N (dynamic range of 40:1). Normal force resolution was found to be 190 mN with a tested range of 8 N (dynamic range of 42:1). Single load and multiload tests were conducted and the sensor exhibited intended behavior with low deviations between trials. Spatial tests were conducted on a 2 x 2 sensor array and a spatial resolution of 1.5 mm was found. This work was presented at IEEE MEMS 2015 conference in Estoril, Portugal [80], and after additional work was published in the Journal of Micromechanics and Microengineering [8]. Special thanks to Jian Cheng and Dr. Teng Li for their initial help with ANSYS.

3.1 Introduction

With recent advances in robotic manipulators, tactile sensing has had an increasing emphasis on compliant designs to accommodate curved surfaces such as robotic fingers. Remarkable progress has been made in the design and fabrication of flexible tactile sensors including multi-axis sensing, high sensor area density, and integration of elastomers with microfabrication [18, 17]. Some notable examples are presented in Table 3.1 which contains performance metrics of each sensor.

One of the remaining challenges related to flexible tactile sensing is maintaining high dynamic range (DR) force sensing in both the shear and normal directions, where DR is defined in this work as force range divided by force resolution. As seen in Table 3.1, achieving a large sensing range and small resolution in a single axis (shear or normal) is difficult, and achieving this in both sensing axes (shear and normal) has yet to be demonstrated. For in-hand manipulation tasks, Yousef defines an ideal sensor range up to 10 N with a resolution of 10 mN (DR = 1000:1) [18]. Typical ranges in Table 3.1 are generally < 1 N for shear force sensing and up to 5 N for normal force sensing. Dynamic ranges are even smaller for capacitive sensors (typical DR = 4:1).

Another challenge is to simplify fabrication in order to increase robustness, reduce costs, and improve manufacturing yield. The referenced tactile sensors in Table 3.1 each have a multi-layered assembly which relies on an out-of-plane "bump" structure to transfer shear forces to the sensing elements. This increases fabrication complexity, and can lead to failure at higher forces when the bump is made from a different, more rigid material [23].

The goal of this work is to create a tactile sensor capable of multi-axis sensing with high dynamic range while maintaining a compliant design with high spatial resolution similar to the human fingertip (1-2 mm [11]). To approach the above challenges, a rapid and simple microfabrication process is presented to reduce time and costs associated with previous tactile sensors while preserving high sensor area density. It improves the state-of-the-art by using electrode geometries of varying heights for capacitive sensing to improve force resolution and range, while maintaining 3-axis (shear and normal) force sensing without the need of an out-of-plane bump structure. It was designed using a multi-physics finite element model and tailored for shear sensing to achieve high dynamic range force sensing.

This paper builds on previous work [80], and presents a more detailed investigation of sensor material properties, governing geometric parameters, and the operation principle of shear sensing. Additional characterization of the sensor is also presented including 3-axis performance, combined loading behavior, spatial resolution tests, and incipient slip tests.

Table 3.1: Metrics of Recent Elastomeric Shear and Normal Tactile Sensors.

Publication	*Type*	*Shear Force*			*Normal Force*			*Sensor*	*Bump*
		Range	*Resolution*	*DR*	*Range*	*Resolution*	*DR*	*Spacing*	*Layer*
ES Hwang [19]	Resistive	*1470 mN	*100 mN	15:1	4000 mN	*250 mN	16:1	*2 mm	Yes
HK Lee [20]	Capacitive	20 mN	*3 mN	6.5:1	20 mN	*3 mN	6.5:1	2 mm	Yes
MY Cheng [22]	Capacitive	108 mN	26 mN	4:1	108 mN	26 mN	4:1	8 mm	Yes
CF Hu [21]	Resistive	500 mN	*25 mN	20:1	5000 mN	*150 mN	33:1	*4.5 mm	Yes
S Pyo [23]	Resistive	500 mN	*100 mN	5:1	2000 mN	*310 mN	6.5:1	*8 mm	Yes
CW Ma [24]	Resistive	*500 mN	*50 mN	10:1	*5000 mN	*250 mN	20:1	*4.5 mm	Yes
This Work	Capacitive	2000 mN	50 mN	40:1	8000 mN	190 mN	42:1	3 mm	No

*Value estimated based on figure or plot within publication

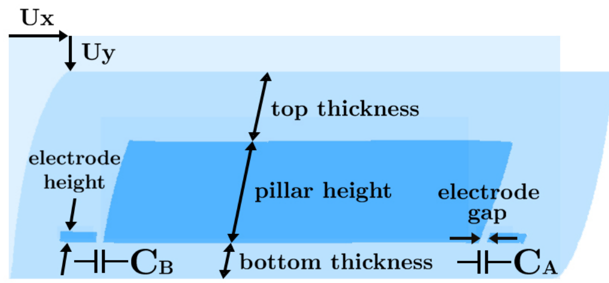

Figure 3.1: Proposed sensor architecture. Displacements U_x and U_y induce predictable changes in capacitance of C_A and C_B in order to detect normal and shear deformation modes.

3.2 Sensor Design

3.2.1 Architecture

Elastomeric materials were selected for the sensor due to their low elastic modulus and ability to withstand high strains. An inexpensive filler particle such as carbon can be added to create a conductive elastomer for the sensor electrodes. This alleviates the need for the deposition of a stiff metallic layer seen in previous sensors [4, 19, 22]. However, conductive elastomers suffer from resistance hysteresis when subject to strain [46, 39], and wiring to sensors is often subject to the same applied pressures and strains as the sensors; therefore capacitive sensing was selected as the preferred sensing method.

Capacitive tactile sensors have typically utilized parallel-plate style electrodes oriented orthogonal to the direction of applied force to transduce normal force or pressure; as a normal displacement is applied to the sensor, the distance between the two plates decreases and therefore increases capacitance [81, 82, 83, 4, 22].

Naturally, this technique requires multiple layers which can increase fabrication complexity. Capacitors with micron-scale air gaps between the electrodes are also limited in force range due to the collapse of the channel at low (sub 100 mN) forces [4, 22]. Sensor architecture is further complicated by the need for an out-of-plane bump structure to induce asymmetric deformation when the sensor is subject to shear forces.

In order to circumvent these complications, the proposed tactile sensor utilizes conductive elastomeric features of varying heights, *pillars* and *electrodes*, which enable predictable shear and normal deformation modes detectable using capacitive sensing. Under shear loading, the pillar deforms towards one electrode and away from the other, Fig. 4.1, while under normal loading, the sensor flattens through Poisson's effect and the electrode gaps uniformly increase. Thus, the *capacitance differential* between the two electrode pairs, $C_B - C_A$, indicates the type of deformation occurring. These pairs of electrodes are placed in both shear directions in order to achieve 3-axis force sensing (2 shear, 1 normal). The conductive features are encased in a dielectric material with additional material on the top and bottom of the sensor for ease of fabrication and to protect the sensing elements. By avoiding air-gap capacitors the sensing range is only limited by the sensor material yield stress rather than the collapse of the air-gap. This feature substantially increases dynamic range over previous capacitive sensor designs (Table 3.1).

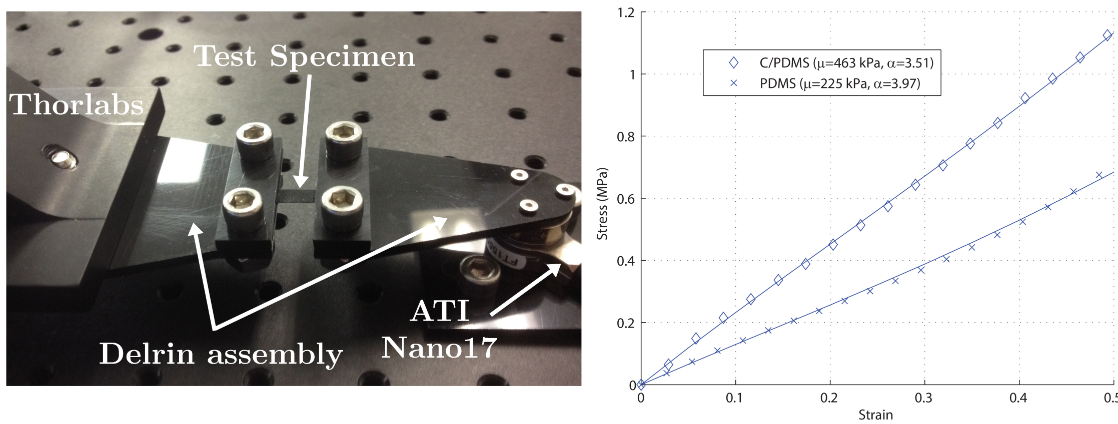

Figure 3.2: (Left) Uniaxial test setup for characterization of polymer composites. (Right) Stress-strain data for C/PDMS and PDMS with fitted 1st-order Ogden curves.

3.2.2 Material Properties

Uniaxial tension tests up to 50% strain were conducted for 10 wt.% carbon-polydimethylsiloxane (C/PDMS) composite and plain PDMS, Fig. 3.2, and were fit with first-order Ogden hyperelastic constitutive models [84] (materials and preperation can be found in Section 3.3). Specifically, the material was displaced by roughly 3 % strain, followed by a 1 second pause (so that force and displacement data could be easily synced during post-processing), and repeated up to 50 % strain. The Ogden model was found to fit the experimental data more accurately than the Neo-Hookean or Mooney-Rivlin hyperelastic material models. The relationship between stress and strain (stretch ratio) is given by Eq. 3.1 and 3.2,

$$\sigma_{Ogden} = \mu(\lambda^{\alpha-1} - \lambda^{-0.5\alpha-1}) \tag{3.1}$$

$$\lambda = \varepsilon + 1 \tag{3.2}$$

where σ_{Ogden} is Ogden stress, μ and α are first-order Ogden material properties, λ is stretch ratio, and ε is strain. The C/PDMS was found to have a slightly stiffer response than the PDMS which is consistent with the presence of a filler particle [85, 86]. A fairly linear response was observed in each material for these relatively low strains. For C/PDMS, a μ and α of 463 kPa and 3.51 were found, respectively, while for PDMS values of 225 kPa and 3.97 were found. These material properties were used in the subsequent finite element simulations.

3.2.3 Multiphysics Finite Element Modeling

To guide design, 2D nonlinear large deformation finite element simulations were conducted using ANSYS to study the effect of sensor geometry on capacitance. An uncoupled multiphysics simulation based on [87] was developed such that: first, the geometry was mechanically deformed (element type PLANE182), and secondly, capacitance was solved using the CMATRIX command in the deformed configuration (element type PLANE121). A dielectric permittivity of 2.5 was assumed for PDMS. A fixed boundary condition was applied to the bottom edge, while X and Y displacements were applied to the top edge simulating shear and normal displacements respectively, Fig. 4.1.

Three parametric studies were conducted. First, the sensor was sheared and the capacitance differential was studied as a function of pillar and electrode height,

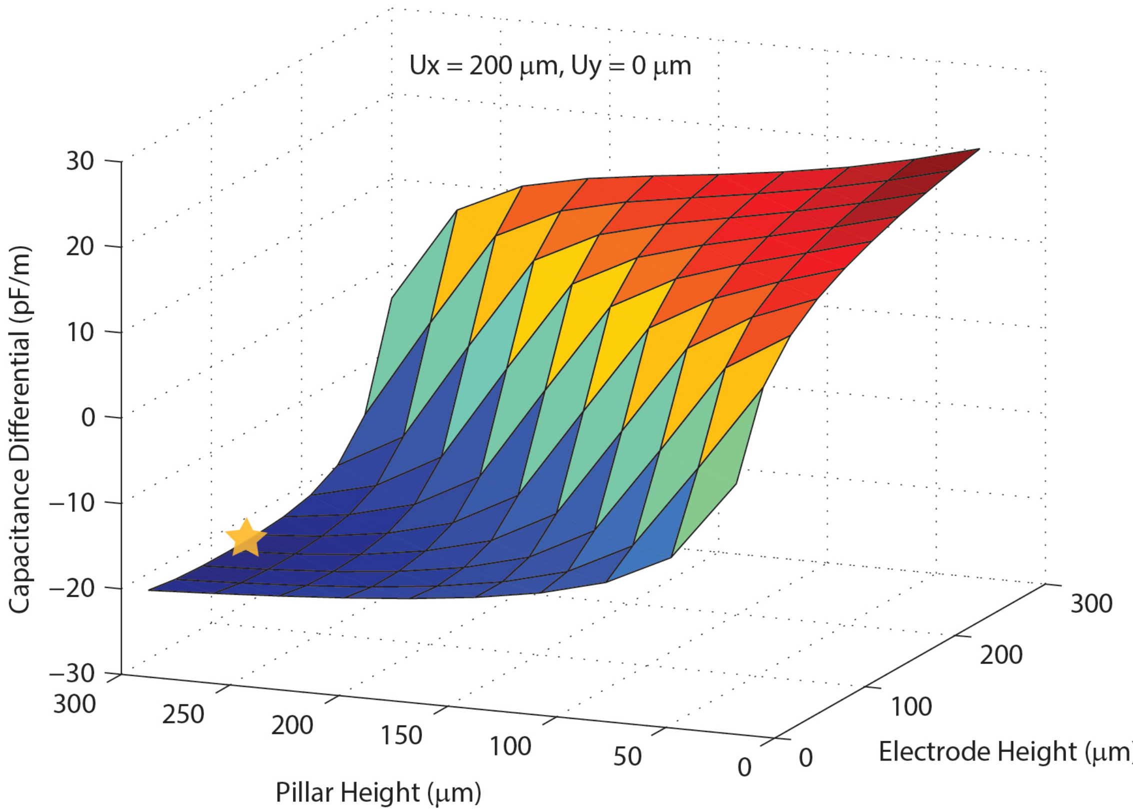

Figure 3.3: Finite element parametric study of the effects of pillar and electrode height on the capacitance differential when subject to shear displacement. The gold star is the geometry selected.

Fig. 3.3. A large capacitance differential is preferable for shear force sensing. Second, the sensor's initial capacitance (i.e.: undeformed capacitance) was studied as a function of pillar and electrode height, Fig. 3.4. A high initial capacitance is preferable for normal force sensing [65]. From these two simulations, specific pillar and electrode heights were selected. Thirdly, the sensor was sheared using the selected pillar and electrode heights and the capacitance differential was studied as a function of the dielectric top and bottom thicknesses, Fig. 3.5.

In each figure, the Z-axis is in pF/m due to the 2D simulation, and the actual

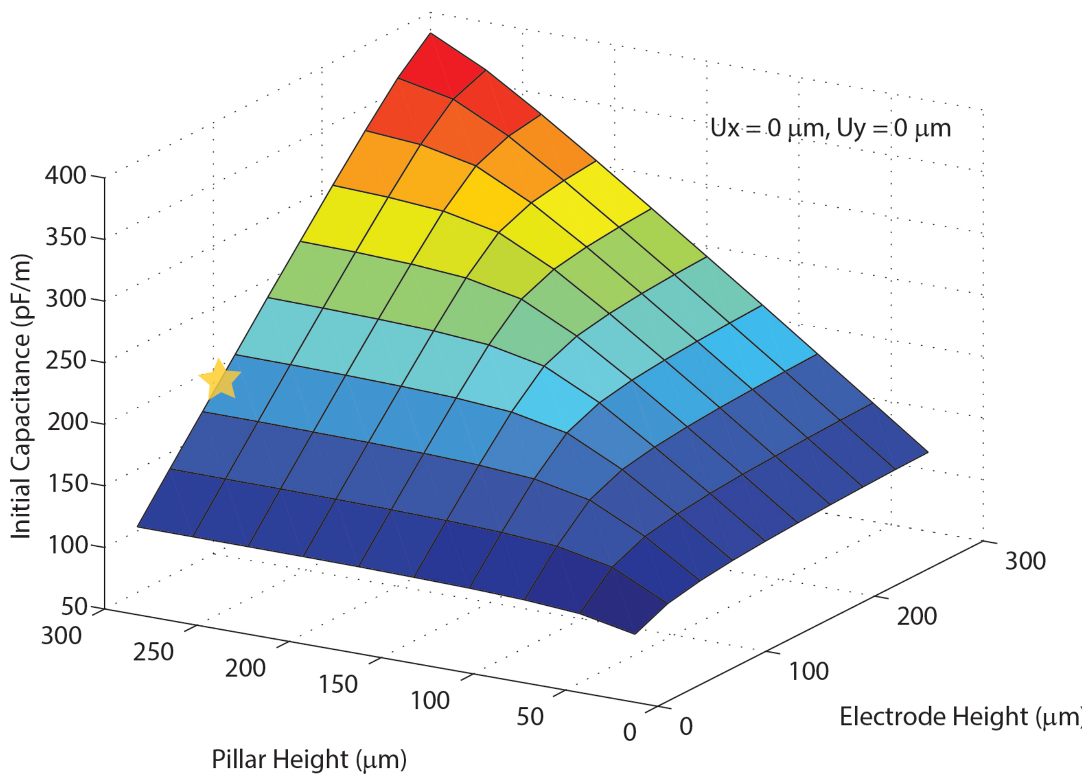

Figure 3.4: Finite element parametric study of the effects of pillar and electrode height on initial (undeformed) capacitance. The gold star is the geometry selected.

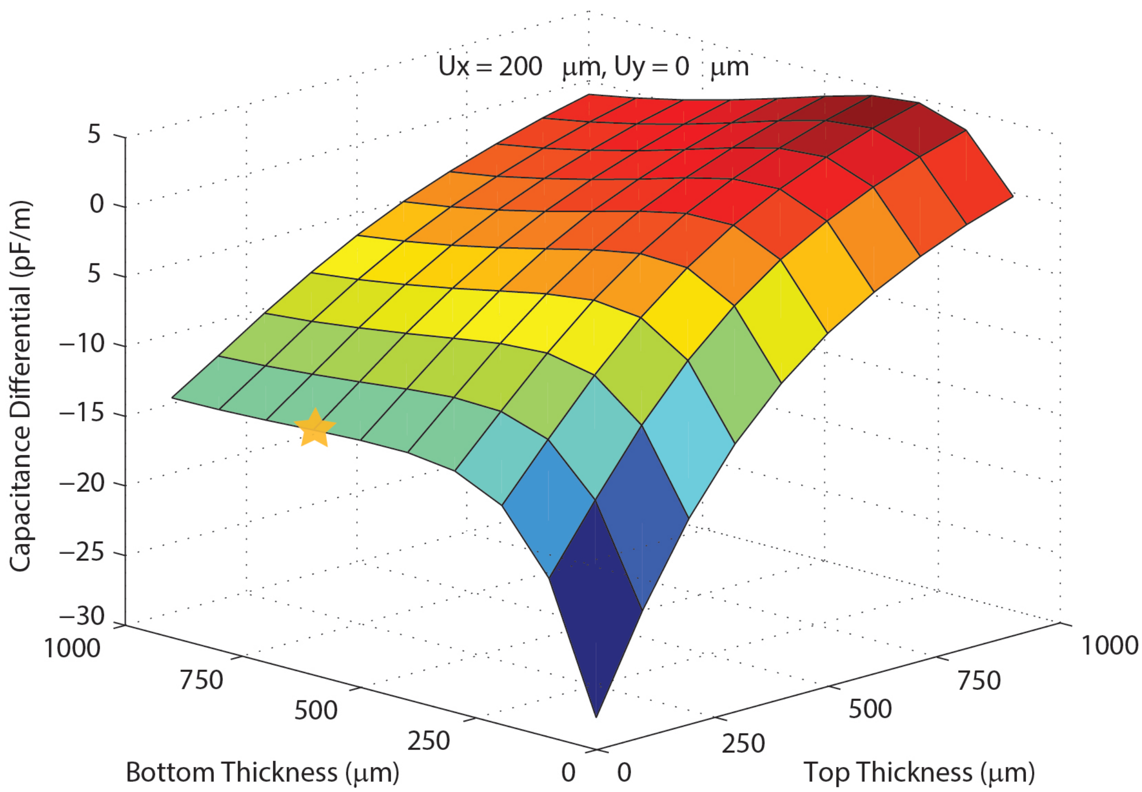

Figure 3.5: Finite element parametric study of the effects of top and bottom thickness on capacitance differential when subject to shear displacement. The gold star is the geometry selected.

capacitance can be found by multiplying the out-of-plane electrode width, which in the fabricated design was 1 mm. Sensor thickness was arbitrarily selected for the simulations in Fig. 3.3 and 3.4; bottom thickness was 100 µm, and the sum of the top thickness and pillar height was held constant at 500 µm. Preliminary simulations revealed that smaller electrode gaps resulted in larger changes in capacitance, so an electrode gap of 20 µm was selected; it was also the smallest gap that could be consistently fabricated. A simulated shear displacement of 200 µm was selected as a benchmark of performance.

In Fig. 3.3, two extreme regions were found: a tall pillar and short electrode (blue region), and vice versa (red region). In addition, when the pillar height equals the electrode height, a capacitance differential of zero is found (green region). Therefore, the difference in height between the pillar and electrode is what enables shear sensing. By contrast, for normal sensing it was found that a large pillar height and electrode height lead to the highest initial capacitance, Fig. 3.4. Due to the competing phenomena, a geometry that maintains both high capacitance differential and sufficient initial capacitance was selected, as represented by the gold stars in Fig. 3.3 and 3.4; electrode height was 100 µm, and pillar height was 300 µm.

In Fig. 3.5, the simulation that exhibited the highest strain of 24% was for a bottom and top thickness equal to 100 µm; this was about half of the maximum strain tested in Section 3.2.2. This point corresponded to the highest capacitance differential. However, a large bottom thickness improves the ability to peel the device from the silicon mold without risking a tear during fabrication, as described in Section 3.3, thus a bottom and top thickness of 600 µm and 100 µm, respectively,

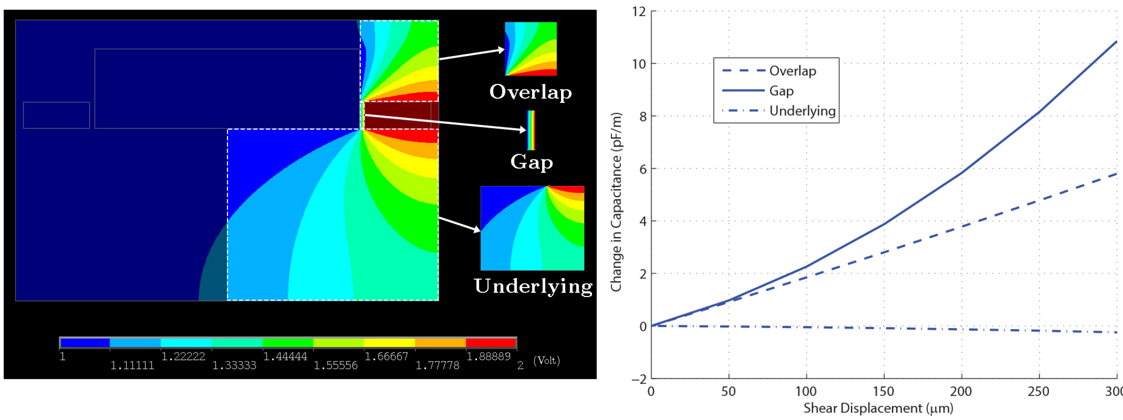

Figure 3.6: (Left) Sensor areas in which electrostatic energy changes as the sensor deforms. (Right) Finite element results of the change in capacitance of each area when subject to shear displacement.

were selected as represented by the gold star in Fig. 3.5.

3.2.4 Shear Sensing Mechanism

To better understand how capacitance changes during shear deformation, the proposed sensor was divided into three areas in which the electrostatic energy changes as a shear displacement is applied, Fig. 3.6. As a shear displacement is applied toward the right, the pillar deforms over the electrode which increases the electrostatic energy in the *Overlap* area while also increasing the energy in between the electrodes, the *Gap* area. The *Underlying* area was found to slightly decrease in energy and makes little contribution to the overall change in capacitance. A linear and nonlinear change in capacitance was observed in the *Overlap* and *Gap* areas, respectively, indicating that at lower shear displacements a relatively linear change in capacitance is expected. The areas on the left side of the pillar in Fig. 3.6 were found to behave similarly, but decrease in capacitance rather than increase.

3.2.5 Element Sensitivity

To evaluate the quality of the mesh (i.e.: does the mesh accurately capture deformations) and how the element size affects the results, the element size was varied while the geometry and boundary conditions were held constant. Ideally, an infinite number of elements would be used to most accurately capture the deformation of the model, but computational resources are limited. Therefore, an element size which accurately captures the deformation with a reasonable solve time (less than 1 hour) was desired. The critical feature in this FEA model was the electrode gap, and a sufficient number of elements had to fit within the gap to accurately model the deformation and capacitance, Fig. 3.7. Therefore, the element size was varied in such a manner that simulations had 1 to 20 elements across the electrode gap, Fig. 3.8. It was found that changes in capacitance were mostly insensitive to element size, while initial capacitance was highly sensitive below 4 elements. In the presented work, 4 elements were used which was sufficient for modeling purposes. Sample results showing the stress, strain, and electric field contours when the number of elements between the gap was 5 can be seen in Fig. 3.9.

3.3 Microfabrication

Sensors were made from a reusable silicon mold, which was fabricated using a two mask microfabrication process, Fig. 3.10. Silicon dioxide was deposited on a silicon

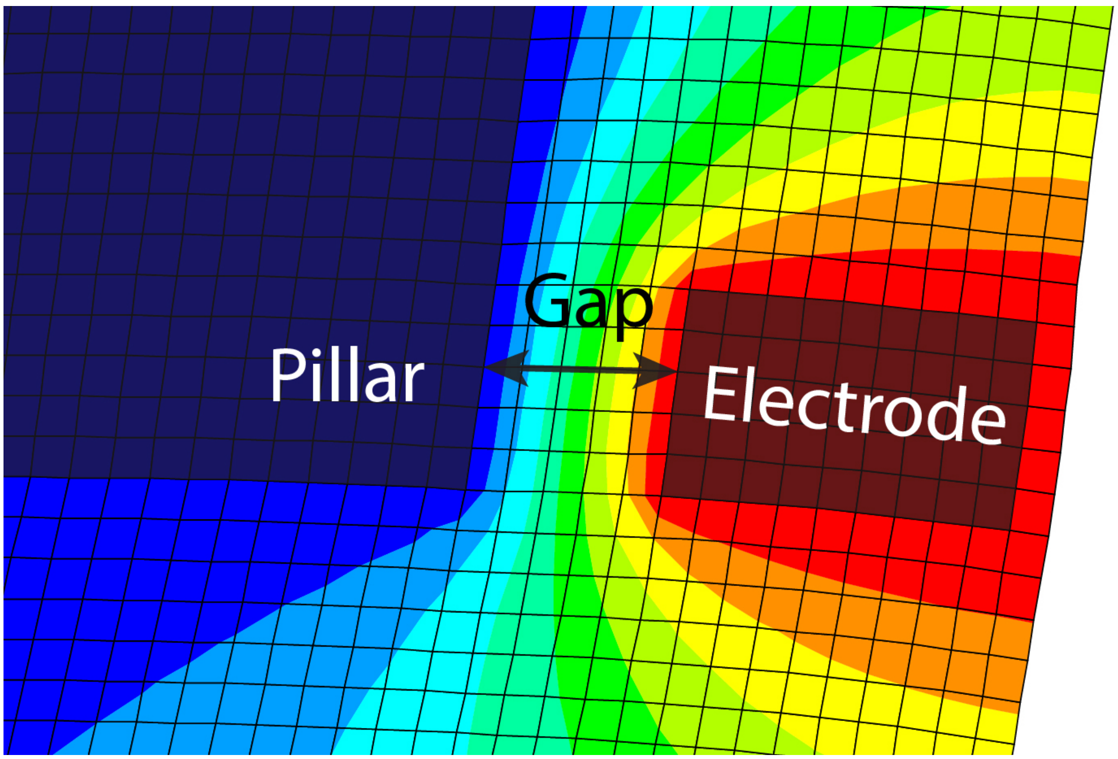

Figure 3.7: Close up image of the mesh. In this model, 5 elements spanned the gap between the pillar and electrode. Simulations varied from 1 to 20 elements across the gap.

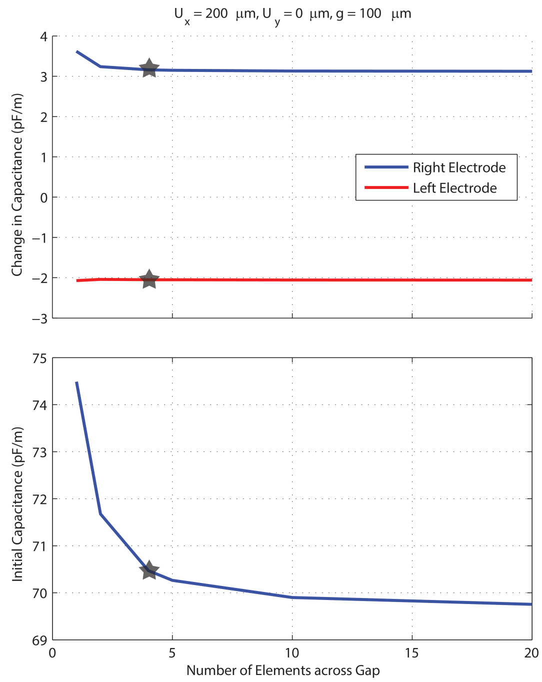

Figure 3.8: Results of the element sensitivity study when the gap was 100 µm, shear displacement was 200 µm, and normal displacement was 0 µm. The x-axis is the number of elements across the gap; as the number of elements across the gap increases, the element size decreases. [Top] The change in capacitance between the pillar and left and right electrode as a function of elements across the gap. The change in capacitance was found to be mostly insensitive to element size. [Bottom] Initial capacitance between the pillar and one of the electrodes (symmetric on both sides of the pillar). Capacitance was seen to asymptote to just under 70 pF/m. Black stars represents the number of elements used in the results presented in this chapter (4 elements).

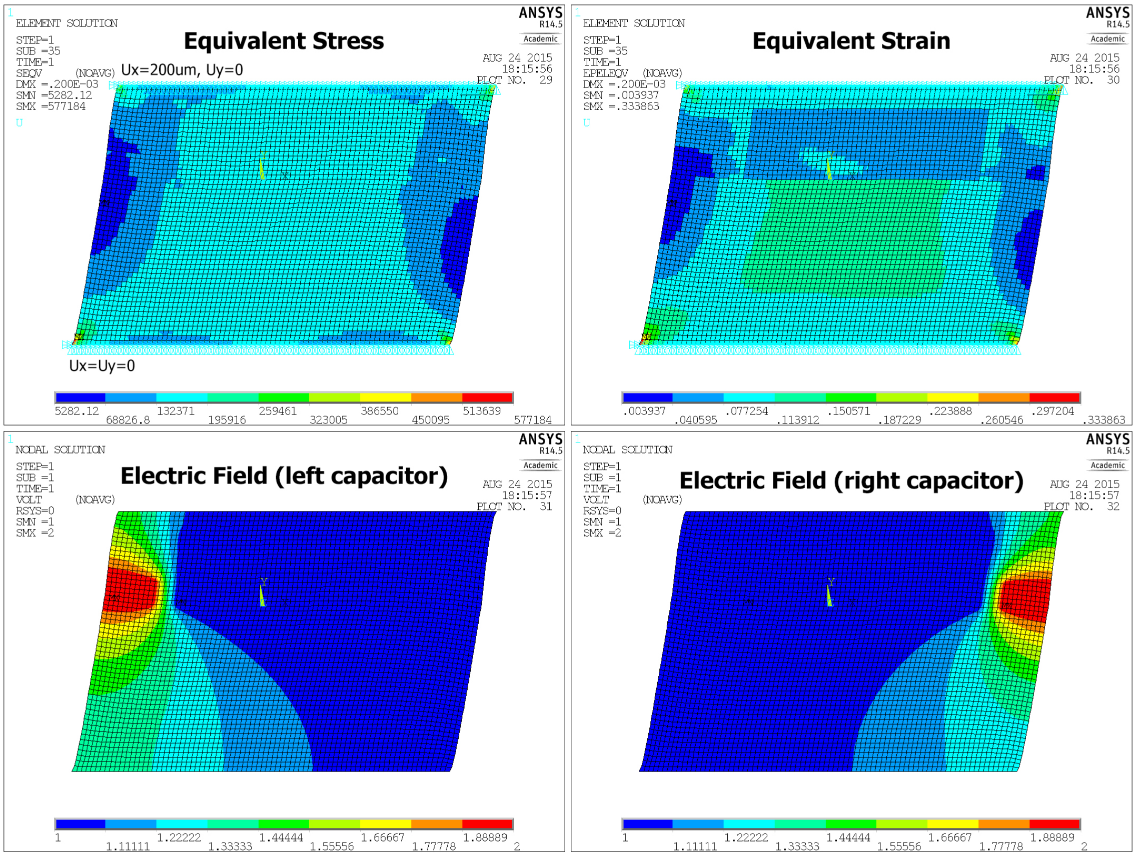

Figure 3.9: Sample contours from the element sensitivity study. In this case, there were 5 elements across the gap.

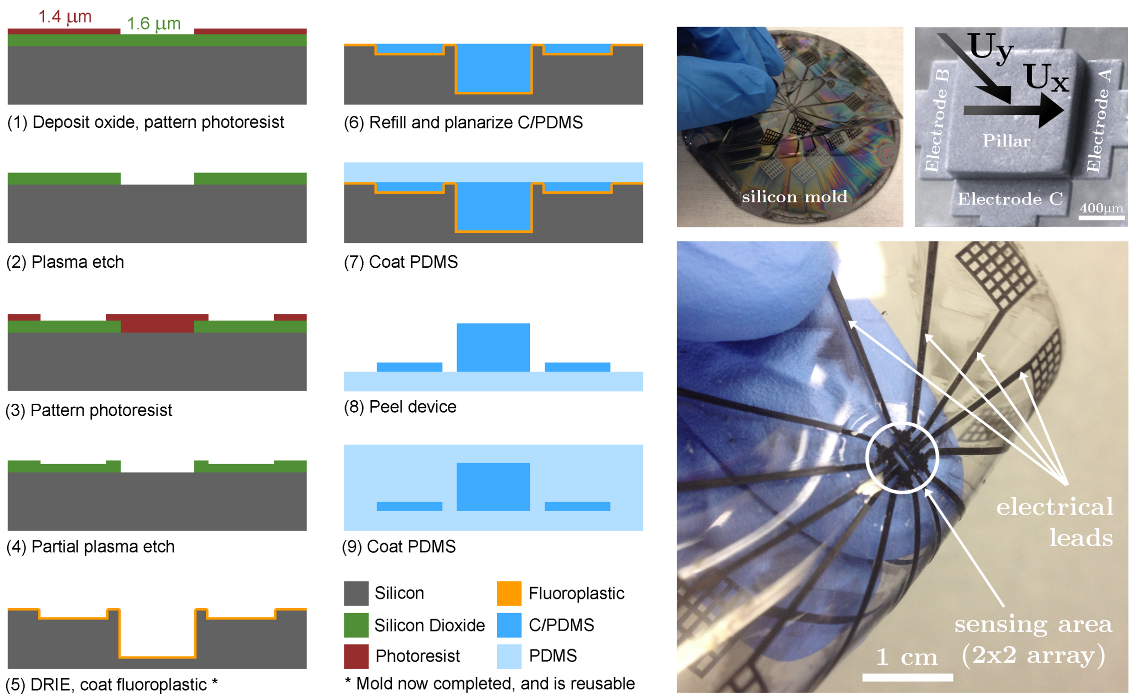

Figure 3.10: (Left) Microfabrication flow chart. (Top off-center) Peeling of the fabricated sensor from the silicon mold. (Top right) Macro photo of a single pillar and surrounding electrodes. This image has been edited for clarity. (Bottom right) Completed sensor in hand.

wafer, patterned, and etched with the first mask containing the pillar geometry. A second pattern and partial oxide etching was done using the second mask, which contained the electrode and electrical lead geometries. Next, an oxygen plasma was used to clean the surface of photoresist, followed by a deep reactive ion etch (DRIE) to create the mold, which was finally coated with a DuPont amorphous fluoroplastic solution (Grade 400S2) as an antistick agent. This completed the reusable silicon mold.

10 wt.% C/PDMS was prepared by mixing 1 g of carbon black powder (39724, Alfa Aesar), 8.18 g of PDMS base and 0.818 g of PDMS curing agent (Sylgard 184, Dow Corning), and 22.5 g of hexane for 30 min. It was poured on the mold, vacuumed for 2 min at 1 Torr, planarized by hand using an industrial screen printing squeegee (Ryonet), and cured on a hot plate for 15 min at 120 °C. After curing, a layer of PDMS was poured on the mold, vacuumed for 15 min at 1 Torr, and cured on a hot plate for 15 min at 120 °C. The vacuum step served to both degas and gravity level the PDMS while controlling the layer thickness. Then, the elastomeric sensor was peeled from the wafer as one whole piece. Lastly, the sensing area was encapsulated in another layer of PDMS using the aforementioned process, and resulted in a total sensor thickness of 1.06 mm. The final all-elastomer sensor can be seen in Fig. 3.10 (Bottom right).

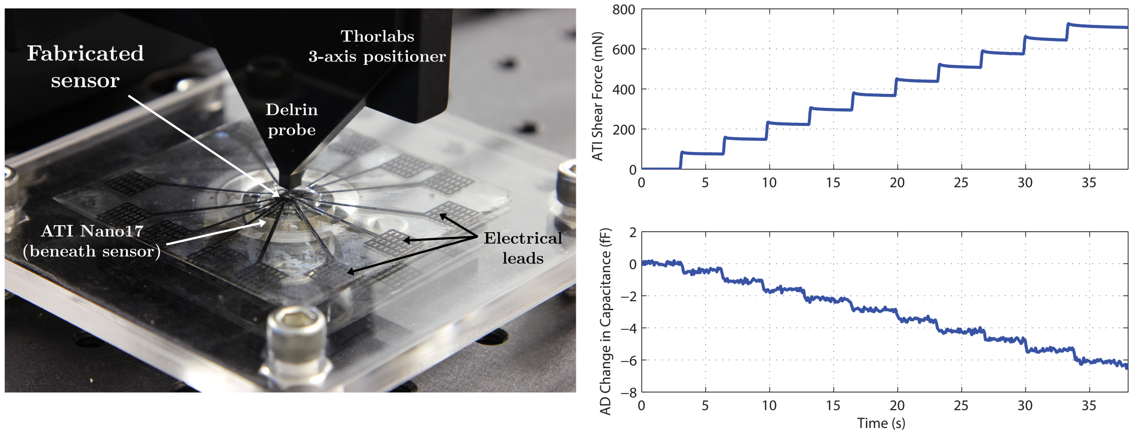

Figure 3.11: (Left) Test setup of the Thorlabs and ATI equipment. The AD7745/46 capacitive board, not shown, has pen-style probes which may be pressed against the fabricated sensor's electrical leads to acquire data. (Right) Sample raw data from the ATI sensor and the AD7745/46 evaluation board. Steps are increments of 10 µm of shear displacement.

3.4 Experimental Results

3.4.1 Test Setup

Testing was conducted by applying a displacement to the sensor and reading the capacitances of each electrode as well as the reaction forces. Micron-scale displacements were applied using a Thorlabs PT3-Z8 3-axis stage equipped with a laser cut Delrin probe which had a square probe tip area of 3 x 3 mm. Capacitance was measured using an AD7745/46 evaluation board with an observed resolution of 0.1 fF at a sampling rate of 16 Hz (unless otherwise noted). Forces were acquired using an ATI Nano17 6-axis force/torque sensor, and the assembled test setup can be seen in Fig. 3.11 (Left).

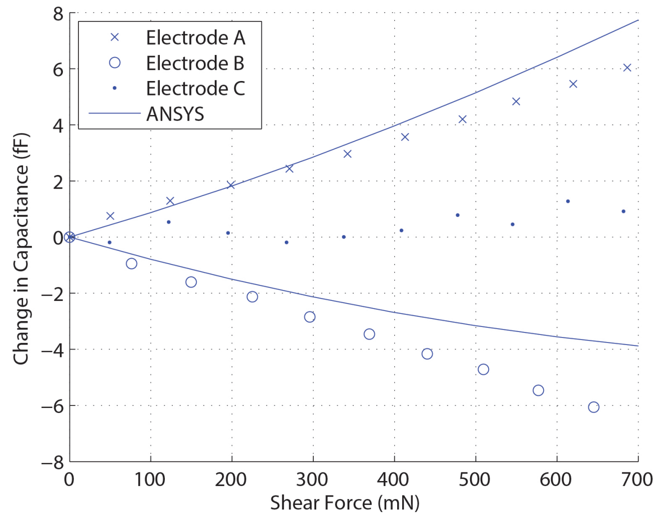

Figure 3.12: High resolution shear testing compared to the finite element model. Each data point was gathered after a shear displacement of 10 µm was applied.

3.4.2 Results

3.4.2.1 Signal Behavior

The data from the ATI sensor and fabricated tactile sensor via the AD evaluation board exhibited step-like behavior in the time domain when subject to incremental displacements, Fig. 3.11 (Right). At higher force readings, a slight decay is apparent in the ATI signal which may be due to polymer relaxation in the sensor, so the median value over the step was used.

3.4.2.2 Shear Force Resolution

Shear force resolution was determined by conducting incremental shear displacement tests. Increments of 10 µm shear displacements were applied up to 100 µm in the positive U_x direction as seen in Fig. 3.10 (Top right).

A pre-applied normal force was necessary to sense shear in order to avoid slip between the probe tip and sensor; without normal force, the probe and sensor are not in contact. In this test and subsequent tests where a normal force preload is used, a normal displacement on the order of 10's of µm was applied to the probe which resulted in normal forces between 1.5 and 2 N. This is a realistic force range seen in robotic grasping [88].

The sensor exhibited a linear capacitive response up to 700 mN shear force, Fig. 3.12. As intended, Electrode A increased in capacitance, Electrode B decreased, while Electrode C remained relatively constant. Fig. 3.12 plots the experimental results along with ANSYS results for the same normal and shear forces. The finite element model predicts a nonlinear response in this range and the deviation between the model and experiment at higher shear force values is possibly due to alignment errors during fabrication or unmodeled changes in material properties. A shear force resolution of 50 mN was observed for Electrode A based on the minimum shear displacement tested (10 µm).

3.4.2.3 Cyclic Loading

Cyclic testing was conducted for a 100 µm shear displacement while a high normal force of 10 N was applied in order to assess any sensor hysteresis, Fig. 3.13, and data from Electrode B was collected. At 100 cycles over 160 s, no hysteresis was observed, and the signal remained clear enough to discern overshoot from the Thorlabs stage controller during the return step of each cycle.

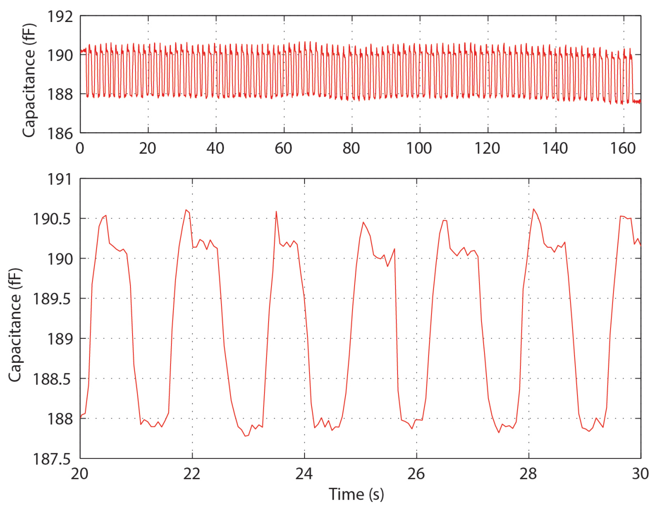

Figure 3.13: Cyclic testing of Electrode B over 100 cycles of 100 µm shear displacement. A detailed view of the signal reveals overshoot from the Thorlabs controller.

3.4.2.4 3-Axis Performance

A single sensor from the tactile skin was selected, and was displaced in 5 Cartesian directions (4 shear, 1 normal) with 5 trials in each direction. Data from each of the 3 electrodes was collected resulting in 75 total capacitance-force relationships, Fig. 3.14.

In the shear tests, Fig. 3.14 (a)-(d), increments of 50 µm displacements were applied up to 250 µm after a normal force preload was applied. As intended, capacitances of electrodes parallel to the direction of applied shear changed little compared to adjacent electrodes. This indicates an ability to differentiate the direction of applied shear force. Measured capacitance and force readings were consistent between trials, suggesting a highly repeatable behavior.

In the normal tests, Fig. 3.14 (e), increments of 30 µm displacements were applied up to 150 µm. A decrease in capacitance was observed in each electrode

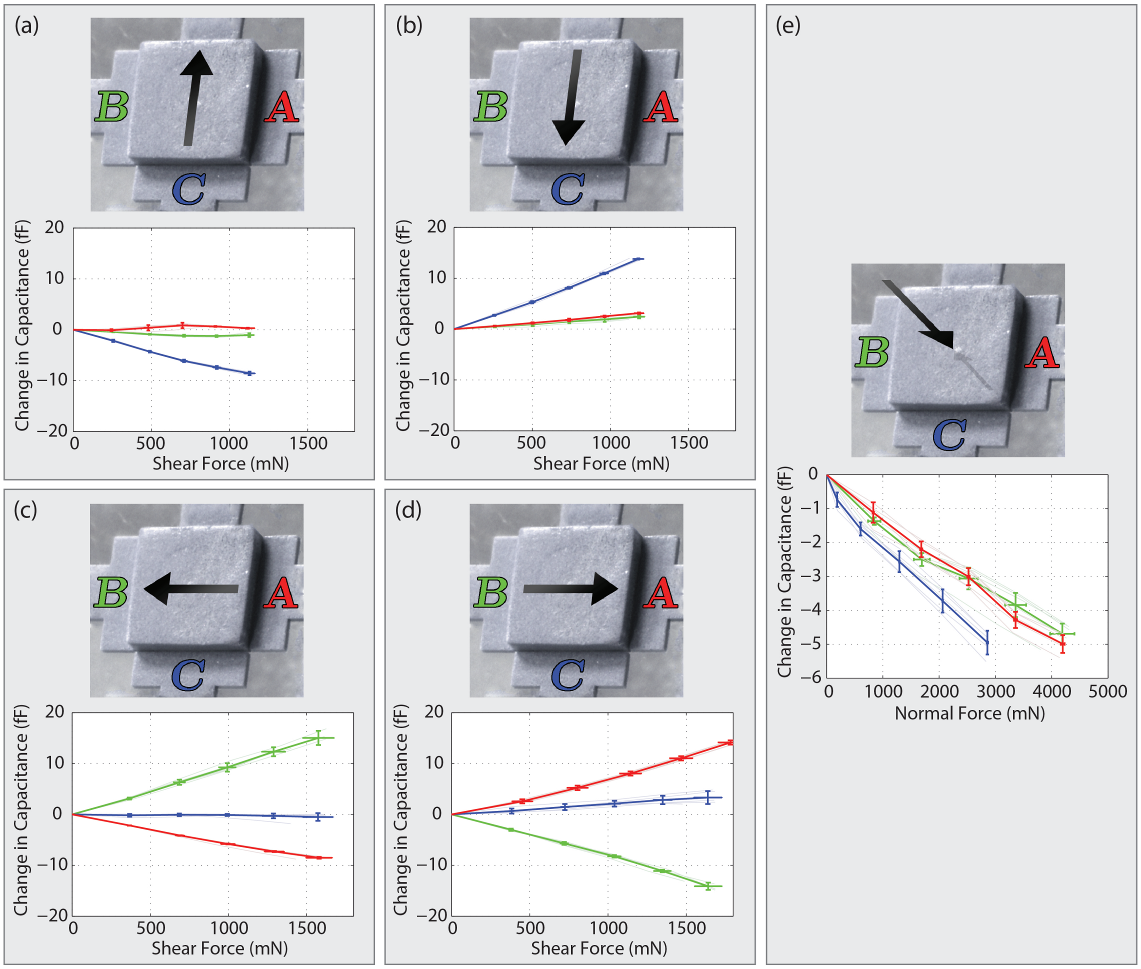

Figure 3.14: 3-axis tests in each direction and the response of each electrode, A (red), B (green), and C (blue). (a)-(d) For shear testing, increments of 50 µm displacement were applied up to 250 µm. (e) For normal testing, increments of 30 µm displacement were applied up to 150 µm. Force (horizontal) and capacitance (vertical) deviation bars are for one pillar tested over 5 trials. The photos adjacent to each plot have been edited for clarity.

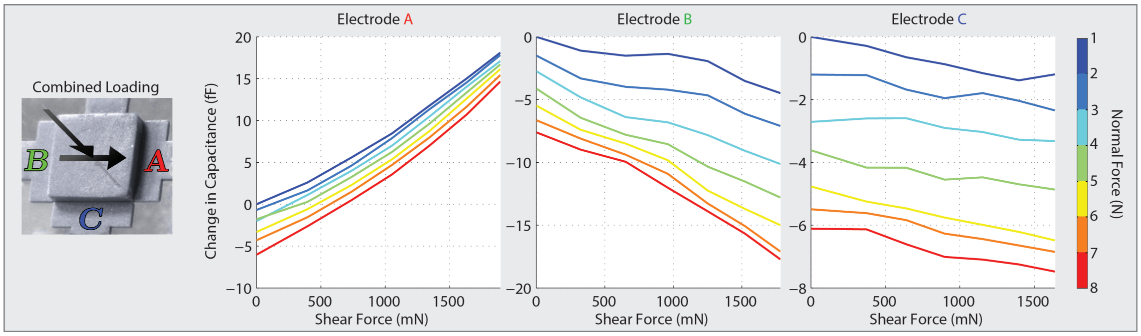

Figure 3.15: Mixed loading performance of each electrode when subject to simultaneous shear and normal forces. One trial per load case was conducted. The adjacent photo has been edited for clarity.

consistent with previously observed behavior [65, 80]. A normal force resolution of 190 mN was observed for Electrode C based on the minimum normal displacement tested (30 µm). The change in capacitance of the normal tests was less than that of the shear tests per force (i.e.: lower sensitivity). This is an expected outcome since the sensor was designed to maximize capacitance differential under shear, and maximizing initial capacitance was secondary (Section 3.2.3).

3.4.2.5 Mixed Loading

Capacitance contours of each electrode were collected over an array of shear and normal forces, Fig. 3.15. This test also included the maximum ranges applied (2 N in shear and 8 N normal), although sensors were not tested to failure. One trial per load case was conducted. A decrease in capacitance was observed in all electrodes as a normal force was applied, as intended. Each electrode behaved as expected when subject to shear regardless of applied normal force. Electrode C, which was oriented

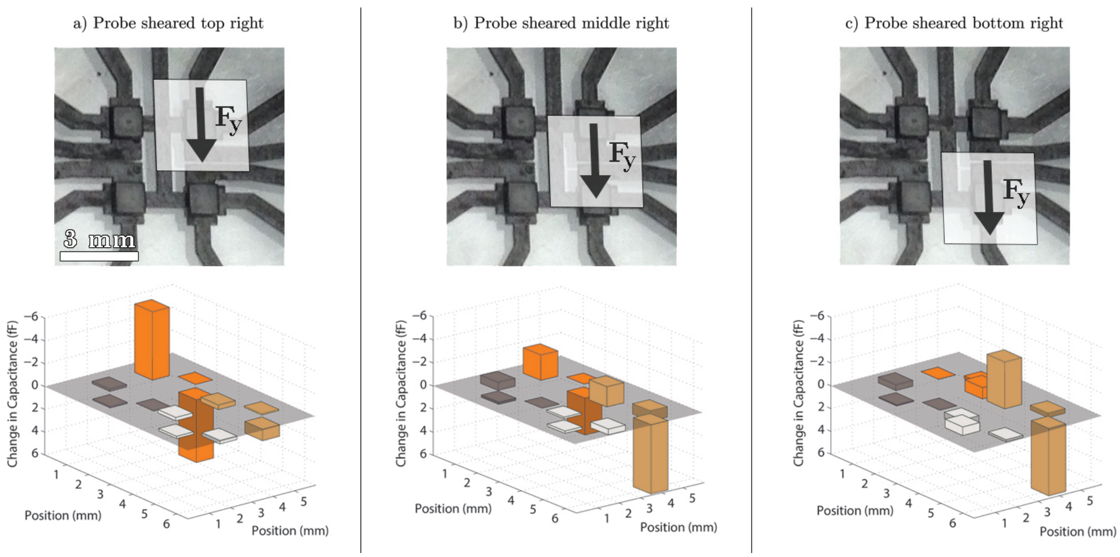

Figure 3.16: Spatial resolution tests in which a 700 mN shear force was applied at three different locations each 1.5 mm apart. (a) Probe centered over the top right pillar. (b) Probe placed between the two right pillars. (c) Probe placed over the bottom right pillar.

parallel to the direction of applied shear, exhibited a slight decrease in capacitance as shear force was applied. Sensor sensitivity to shear was found to be relatively independent of normal force. Using this information, the change in capacitance of each electrode can be used to infer the type of deformation occurring. For example, a nonzero capacitance differential across two opposite electrodes indicates shear occurring, while a net decrease of each electrode indicates the presence of an applied normal force. A detailed predictive model for applied forces given these capacitive changes is subject to further work.

3.4.2.6 Spatial Resolution

A shear force of 700 mN was applied at three locations, each 1.5 mm apart, and the change in capacitance of each electrode was collected, Fig. 3.16. The tactile skin contained 4 pillars with 3 electrodes each yielding 12 total measurements. A preload normal force was applied prior to each test.

The electrodes that experienced changes in capacitance were observed to correspond with the location of the probe, while small changes in capacitance were observed elsewhere. These small changes may have been due to poor electrical connections between the electronics and sensor that resulted in a noisy signal. The results suggests low spatial crosstalk and a minimum spatial resolution of 1.5 mm using the tested probe (i.e.: the minimum change in position of the probe detectable was 1.5 mm).

3.4.2.7 Incipient Slip

In order to investigate the sensor's ability to detect incipient slip which is important to robotic grasping [89], a preload normal force was applied followed by a high shear displacement of greater than 1 mm to induce slip between the sensor and probe, Fig. 3.17. Capacitance was collected from Electrode B at a sampling frequency of 90 Hz, which was the maximum frequency of the AD evaluation board. Upon initial loading, a decrease in capacitance can be seen as expected, Fig. 3.17 Region (II). Then, a sudden increase and oscillation in the signal was observed upon initiation of slip, Fig. 3.17 Region (III). The signal was filtered using an 11-point moving

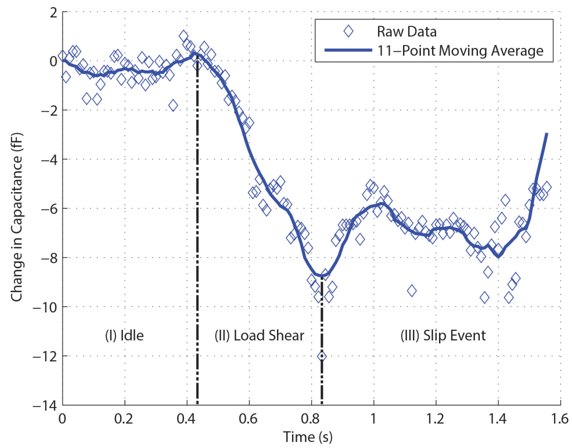

Figure 3.17: Incipient slip test. As the sensor is sheared, Region (II), slip is observed near t = 0.8 s. An 11-point moving average can be seen to jitter over several femptoferrads in Region (III). A sampling rate of 90 Hz was used.

average to more clearly display the data trends.

3.5 Limitations and Future Work

One limitation of this sensor was the lack of a readily available high conductivity composite polymer. For this reason, electrical routing from the electrodes and pillars had to be significantly wider than anticipated, which left no available space for a fourth electrode to oppose Electrode C. A high conductivity composite polymer, such as silver-polydimethylsiloxane (Ag/PDMS) [34], may potentially solve this issue; it was also utilized in previous work [65], but has since been difficult to incorporate in fabrication due to its tendency to separate after mixing.

Another challenge was the use of in-plane wiring which significantly reduced the ability to create an array larger than 2 x 2. An additional backing layer, such as polyimide, with protruding electrical leads to penetrate the C/PDMS may be necessary in the future to expand the array.

3.6 Conclusions

A novel all-elastomer MEMS tactile skin has been presented, which utilizes electrode geometries of varying heights to sense both shear and normal forces without the need of an out-of-plane bump. The tactile skin was fabricated using a simple and rapid molding process while maintaining high sensor area density, with sensors spaced every 3 mm. A high dynamic shear and normal force range was achieved of 40:1 and 42:1, respectively, which is the highest reported of elastomeric 3-axis sensors thus far. This was achieved through the guidance of a finite element model to tune the tactile skin for shear sensing. Future work could utilize a higher conductivity polymer to decrease feature size and increase sensor area density further.

Chapter 4

Rapid manufacturing of mechanoreceptive skins for slip detection in robotic grasping

4.1 Abstract

This chapter presents a major advancement in the manufacturing of the elastomer sensors from the previous chapters and demonstrates these sensors in a basic robotic system. The contents of this chapter are in the process of being submitted to journals as of July 2016.

This work demonstrates a rapid manufacturing process and taxel geometry to create the first large area, all-elastomer "robot skin" capable of 3-axis tactile sensing. The milling-based process avoids clean room time while producing features over multiple length scales, from 10s of microns to 10s of centimeters, and molds all-elastomer materials to create a mechanically flexible skin. Taxels can detect applied loads using either a contact resistive approach that uses simple circuitry, or a capacitive approach that provides high dynamic range. A finite element model was developed to select a taxel geometry favorable for contact resistive sensing. Using the contact resistive approach, normal force range and resolution were 8 N and 1 N, respectively, and shear force range and resolution were 450 mN and 100 mN, respectively. Using the capacitive approach, normal force range and resolution were

10 N and 100 mN, respectively, and shear force range and resolution were 1500 mN and 50 mN, respectively. A robot skin the size of a human hand was manufactured with 12 taxels, and was capable of detecting normal and shear loads over a large area. Finally, a single contact resistive taxel was integrated into a one degree-of-freedom gripper, and was able to detect and prevent slip of a grasped object.

4.2 Introduction

As the field of robotics progresses towards autonomy, advanced tactile sensors are pivotal in enabling safe and dexterous interaction between a robot and it's environment [18, 90]. Robotic tasks that generally rely on vision alone, such as grasping, are greatly enhanced with the addition of tactile sensing [91]. Shear force sensing in addition to normal force sensing is especially important in detecting slip of a grasped object [56]. Other wearable systems such as exoskeletons [14], shoes [92, 93], and gloves [94, 13] also stand to benefit from affordable, sensor rich "robot skins" that provide real-time force vectors over a large area.

Over the past three decades, notable progress has been made in the field of tactile sensing. Camera-based tactile sensors, in which a soft material is pressed and the deformation is processed visually, have been able to achieve microscale spatial resolution but they're typically limited to a small sensing area and have large, specialized hardware [95]. More compact and versatile sheets of tactile sensor arrays have also been developed [8], and leverage MEMS manufacturing to create microscale sensor geometries essential to multi-axis sensing. However, this method typically results in laborious and complicated multilayer assembly with sub newton force ranges [20]. MEMS manufacturing also limits the sensing area to that of a silicon wafer [24]. Other tactile sensors which have large sensing areas have been limited to normal force sensing only [25, 96], or have had limited flexibility [97]. Microfluidic eutectic indium gallium (eGaIn) tactile sensors have achieved remarkable flexibility but are potentially hazardous if ruptured [98]. Therefore, there is a need for a flexible, large area tactile sensor array capable of shear force sensing in addition to normal force sensing.

The transduction method also plays an important role in the design and performance of tactile sensors. Flexible tactile sensor arrays typically utilize parallel-plate style capacitors [22], or resistive serpentines or strips to detect applied loads [23]. Elastomer-based piezoresistive sensors tend to suffer from electromechanical hysteresis [46, 9], Fig. 4.2, and capacitive sensors [8, 48] require significant efforts in shielding. The sensor design in this paper can support multiple transduction methods to trade off performance metrics for simplicity in integration. For example, a prosthetic sensor interface may not require the same dynamic range as a robotic manipulation application.

In this work, an all-elastomer large area robot skin capable of shear and normal force sensing was developed. A contact resistive sensing technique to simplify electronics and minimize hysteresis was proposed and modeled using finite element analysis. Robot skins were created using a novel manufacturing process that facilitated microscale features over a large area, and produced a robot skin as large as a human hand. Force characterization was carried out for both contact resistive and

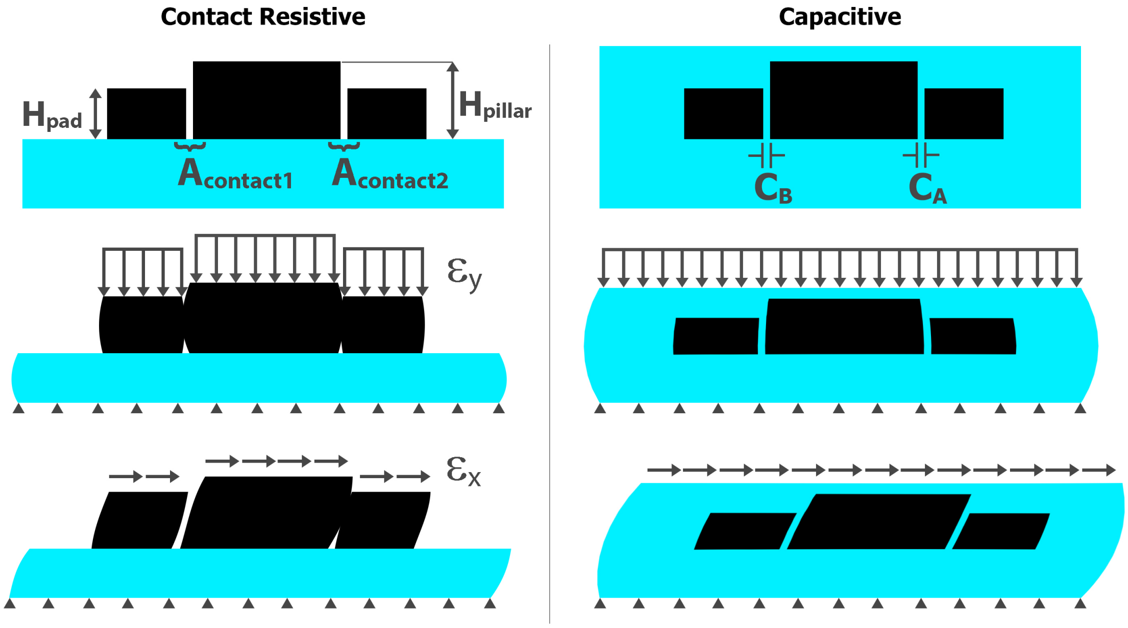

Figure 4.1: Cross-sectional view of the sensor architecture for the contact resistive (left) and capacitive (right) approaches. Blue areas are PDMS, and black are conductive-PDMS. [Left] As forces are applied, the "pillar" and "pads" come into physical contact and cause a measurable change in contact resistance. As a normal force is applied, the pillar and pads come into contact causing a uniform decrease in contact resistance on each side. As a shear force is applied, contact resistance decreases in the direction of shear and increases on the opposite side. [Right] An additional layer of PDMS is used to encapsulate the sensing elements for capacitive sensing [8]. As a normal force is applied, the sensor flattens and expands through Poisson's effect causing a uniform decrease in capacitance. As a shear force is applied, capacitance increases in the direction of shear and decreases on the opposite side.

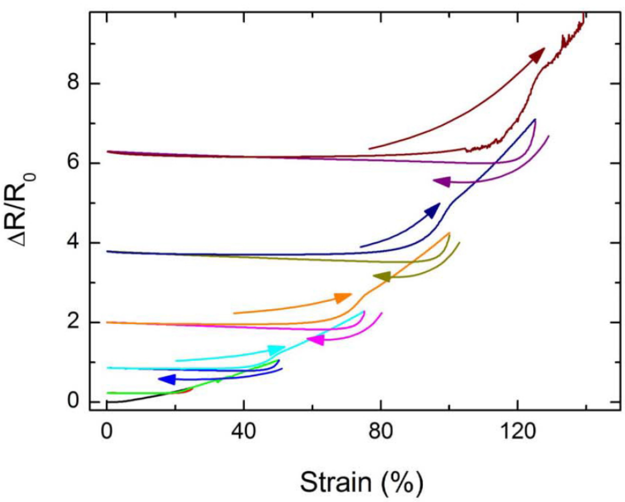

Figure 4.2: A sample of CNT/PDMS was subjected to incrementally higher tensile strains, and the normalized change in resistance is seen to increase after each cycle. This work was conducted by Cai et. al. [9]

capacitive sensing modalities. A single contact resistive taxel was incorporated into a one degree-of-freedom robotic gripper for slip detection and 3-axis sensing was also demonstrated on a robot skin the size of a human hand.

4.3 Taxel Architecture

Two sensing modalities are presented in this work: a *contact resistive* approach to simplify electronics and minimize electromechanical hysteresis, and a high dynamic range *capacitive* approach based on prior work [8], Fig. 4.1. A contact resistive sensing technique was developed in which two conductive features, referred to as the "pillar" and "pad", come into physical contact as loads are applied. As a normal force is applied, the pillar and pads flatten and expand through Poisson's effect, and come into contact causing a uniform decrease in contact resistance on each side. Meanwhile, a shear force results in a differential contact resistance; contact resistance decreases in the direction of shear and increases on the opposite side.

In the capacitive sensing approach, the sensor is encapsulated with a dielectric to form a capacitor between the pillar and pad. As a normal force is applied, the sensor flattens and expands through Poisson's effect, the capacitor gap increases, and the capacitance decreases on each side uniformly. Meanwhile, a shear force results in an increase in capacitance in the direction of loading, and a decrease in capacitance on the opposite side.

Elastomers such as polydimethylsiloxane (PDMS) are especially favorable for these architectures since they are incompressible (Poissons ratio near 0.5), which maximizes lateral expansion under normal deformation. The contact resistive approach differs from previous contact resistive work [99] in that the sensor circuit is open in the unloaded state and becomes closed as forces are applied, rather than being continuously closed.

4.4 Finite Element Modeling

A 2D nonlinear, large deformation finite element model was written in ANSYS Mechanical APDL 14.5 to evaluate the effects of sensor geometry on contact area between the pillar and pads when subject to shear and normal deformation modes. As contact area increases the contact resistance decreases; therefore, a sensor architecture that maximizes contact area under normal deformation while maximizing

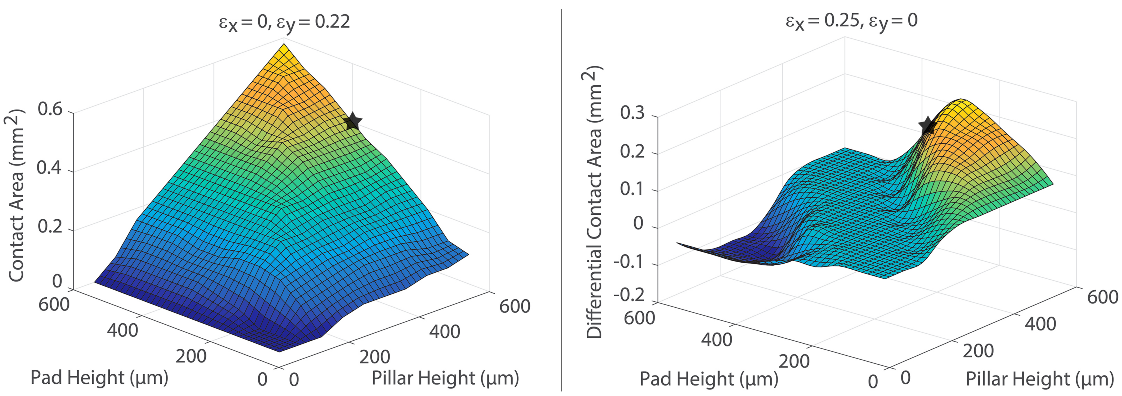

Figure 4.3: Parametric study of the contact resistive geometry using finite element analysis. Normal (left) or shear (right) displacements are applied, and the contact area is shown as a function of pillar and pad heights. The black star is the selected geometry. In the case of shear, differential contact area is plotted and is defined as $A_{contact2} - A_{contact1}$.

differential contact area under shear deformation was desired (where differential contact area was defined as $A_{contact2} - A_{contact1}$, Fig. 4.1).

In this study, the heights of the pillar, H_{pillar}, and pads, H_{pad}, were varied from 60 µm to 600 µm, Fig. 4.3. Preliminary simulations showed that the smallest gap between the pillar and pads enabled the highest contact area. Therefore, the smallest gap that could be reliably fabricated was selected, which was 30 µm (20 µm and 10 µm gaps were also producible but with lower yield). A fixed boundary condition was applied to the bottom edge in both normal and shear simulations. Normal and shear displacements were applied on top of the pillar and pads, and were proportional to the total thickness of the sensor. In essence, this created a strain-controlled boundary condition, and was an important technique in normalizing the data because the total thickness of the sensor varied between simulations. In normal simulations, a displacement was applied that resulted in a net normal strain, ε_y, of 0.22, while in shear simulations a displacement was applied that resulted in a net shear strain, ε_x, of 0.25. A linear-elastic material model based on prior work [8] was used for the PDMS and conductive-PDMS with moduli of 1 MPa and 1.5 MPa, respectively, and both with a Poisson's ratio of 0.49.

Two competing phenomenon were observed. In normal displacement simulations, contact area increased as both the pillar and pad heights increased and was maximal when they were equal. Meanwhile in shear displacement simulations, when the heights were equal a differential contact area of zero was observed due to both pads being in contact with the pillar equally. A maximum was observed at $H_{pillar} = 600\ \mu m$ and $H_{pad} = 300\ \mu m$. Therefore, a geometry that was selected as a compromise between normal and shear force sensing as represented by the black star: $H_{pillar} = 600\ \mu m$ and $H_{pad} = 400\ \mu m$.

4.5 Manufacturing

Computerized numerical control (CNC) milling and micromachining has been widely used to fabricate lab-on-a-chip devices [100, 101], PDMS microstructures and adhesives [102, 103], and even pneumatic logic circuits [104]. In this work, a milling process to cast a conductive elastomer was developed to achieve microscale features over a large area, Fig. 4.4. This was preferred to clean room fabrication from prior work [8] due to the larger available workspace and significantly reduced time

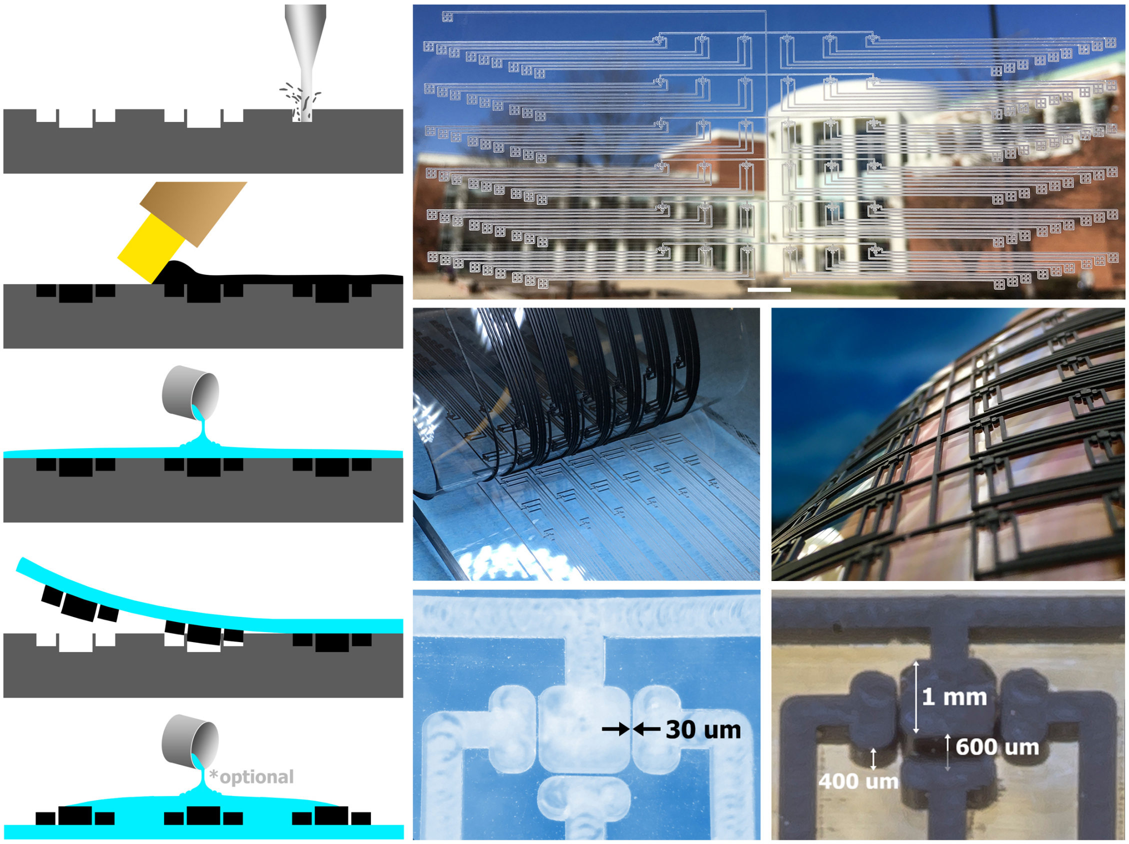

Figure 4.4: [Left] Manufacturing flow chart: acrylic is milled, refilled with CNT/PDMS, coated with PDMS, and peeled from mold. It can then be coated with additional PDMS to encapsulate the sensor for capacitive sensing. [Top] Acrylic mold after milling; scale bar is 1 cm. [Center] Robot skin being peeled from the mold. [Right] Isometric view of the robot skin. [Bottom] Close-up of a single taxel in the acrylic mold. [Bottom Right] Close-up of a single taxel after peeling from the mold.

and money required for fabrication. For example, clean room work requires the outsourcing of masks for photolithography, expensive machines and chemicals, and many hours of processing time by a highly trained individual all while being limited to the working area/volume of a silicon wafer. Meanwhile, a design cycle with the developed manufacturing process takes less than 12 hours to go from concept to in-hand and ready for testing without sacrificing microscale features. Milling has the added benefit of producing highly vertical sidewalls even in tall features (greater than 400 µm), which is difficult to achieve with clean room techniques such as deep reactive ion etching (DRIE).

A stock of acrylic (McMaster-Carr, 8560K355) was milled in a Roland MDX-540SA desktop mill, with a workspace of approximately 12 in by 16 in, using a 406 µm diameter endmill (Microcut USA, 82016). NC instructions were coded in Tool Path Language, and generated using CAMotics 1.0.0. No rough cutting for planarizing purposes was necessary as seen in other work [104]; the stock was sufficiently planar as received. Instead, it was mounted in the CNC machine and leveled by a manual procedure: trenches of varying depths, 0 µm, 100 µm, 200 µm, and 300 µm deep, were milled in the four corners of the stock followed by minor adjustments until each corner exhibited three trenches, Fig. 4.5. The stock was cut at 10 mm/min at 8,000 rpm in taxel areas, and 80 mm/min at 10,000 rpm elsewhere, and finished in approximately 2-3 hours. In the presented design, this method produced features that were 400 µm and 600 µm deep, had a minimum size of 30 µm, and create an array of 6 by 6 taxels spaced every 1 cm. The total area of the mold was 7 in by 4 in.

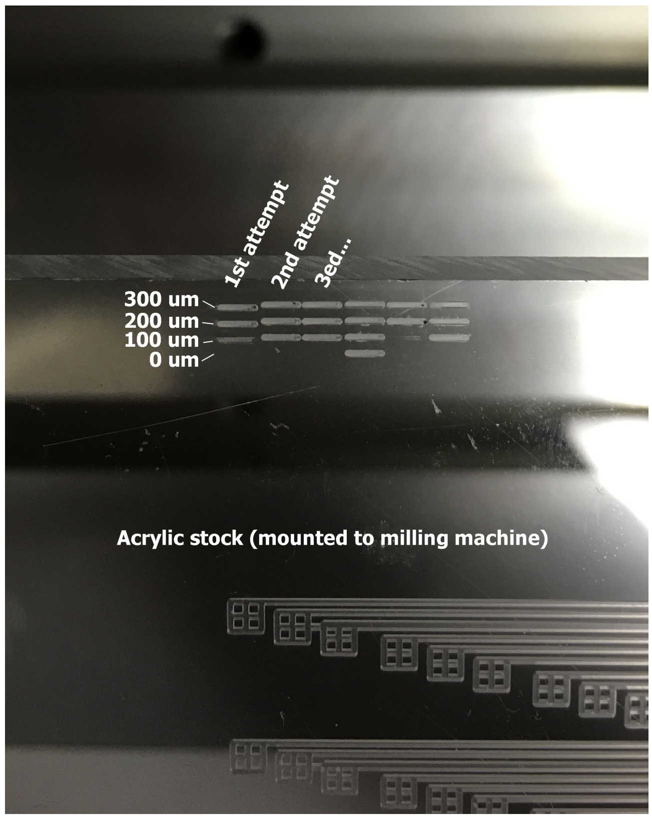

Figure 4.5: To perform leveling, trenches of varying depths, 0 µm, 100 µm, 200 µm, and 300 µm deep, were milled in the four corners of the stock followed by minor adjustments until each corner exhibited three trenches

The mold was refilled with a conductive elastomer. Carbon nanotubes (CNT) (Cheap Tubes, 030103) and 10:1 PDMS (Dow Corning, Sylgard 184) were mixed at a total weight percent of 7 wt.% carbon nanotubes in a centrifugal mixer (Thinky, ARE-310) at 2000 rpm for 90 sec. CNTs were found to be favorable over spherical particles, such as carbon black and silver nanopowder, and exhibited excellent mechanical and electrical properties in PDMS with high yield. Particles such as silver nanowires were too cost prohibitive and were not explored. After mixing, the resulting tar-like CNT/PDMS composite was spread over the mold and planarized using a screen printing squeegee (Ryonet). The mold was placed in an oven at 80°C, a temperature low enough to avoid thermal warping of the acrylic (i.e., below the glass transition temperature), for 30 min to partially cure the CNT/PDMS. After allowing to cool, 10:1 PDMS was poured over the mold and placed in vacuum for 20 min to remove air bubbles, then cured in an oven at 80°C for 90 min. Lastly, the entire robot skin was peeled from the mold, which can be reused, further saving time and money. For capacitive sensing, additional PDMS is poured over the skin, vacuumed, and cured to encapsulate the taxels in a dielectric.

Each taxel consisted of one pillar and three adjacent pads, with gaps of 30 µm between the pillar and pads. Four pads could not be accommodated due to the space requirements of the electrical routing to the pillar using the 406 µm endmill. The total contact resistive robot skin thickness was 980 µm, with a PDMS layer thickness of approximately 380 µm. The completed mold and robot skin can be seen in Fig. 4.4.

4.5.1 Back-side Milling for Electrical Vias

As the robot skin grows in area, the number of wires becomes a major practical barrier to system integration. For example, in a robot skin with n by n sensors, the number of wires scales with $3n^2$. A more streamline method to route the wiring away from the sensing area and interfacing with numerous wiring is therefore necessary. One potential solution is in the use of a flexible printed circuit board (PCB) coupled with an additional milling step to route electrical wiring to the back-side of the robot skin, Fig. 4.6. Once the robot skin is peeled from the mold, it is flipped upside-down onto a flat surface, such as acrylic, and placed within the milling machine. Freshly cured (i.e.: free of surface debris) PDMS also sticks well to acrylic to help hold the robot skin in place during milling. The back-side milling creates "vias" that route through the skin and directly into the conductive features. The vias are refilled with CNT/PDMS. A flexible PCB can then be adhered to the robot skin using additional CNT/PDMS to interface with all of the electrical leads simultaneous, which would be a great improvement over interfacing with the leads one-at-a-time by hand.

4.6 Robot Skin Characterization

4.6.1 Test Setup

Normal and shear displacements were applied using a Thorlabs PT3-Z8 3-axis stage equipped with a 3 by 3 mm acrylic probe, and resultant forces were collected with an ATI Nano17 6-axis force/torque sensor, Fig. 4.7. Contact resistances were measured

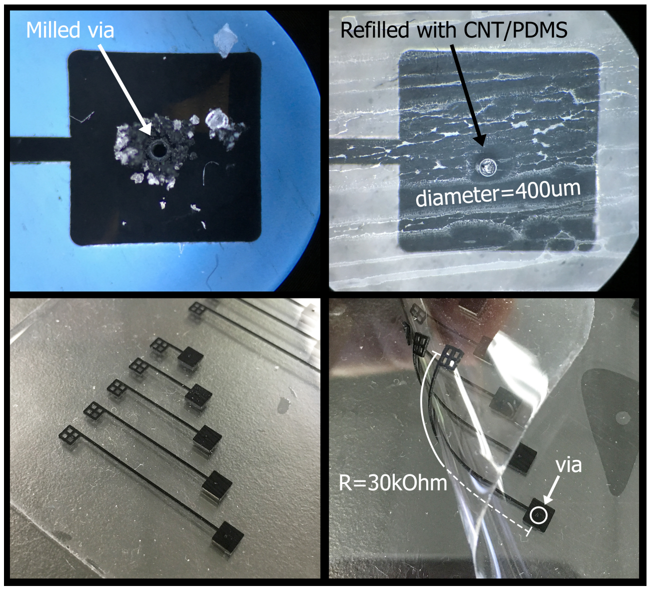

Figure 4.6: Vias were milled into the back-side of the robot skin and refilled with CNT/PDMS to create electrical connections to the sensing layer. A flexible PCB can be bonded to the back-side to make electrical connections across the entire skin. This approach may help alleviate the challenge posed by numerous electrical leads by simplifying the electrical interfacing.

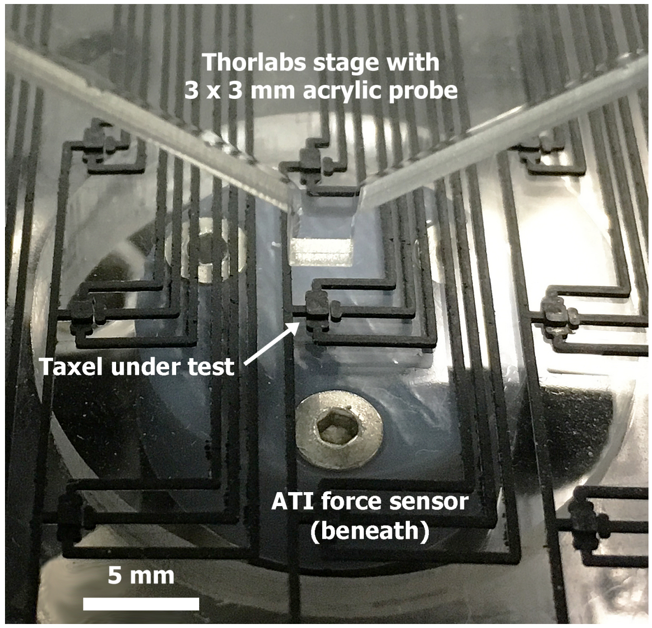

Figure 4.7: Experimental test setup. A Thorlabs 3-axis stage equipped with an acrylic probe, with a probe tip area of 3 by 3 mm, was used to apply displacements to the robot skin. The resultant forces were read with an ATI Nano17 6-axis force/-torque sensor. In the case of contact resistive sensing, an Arduino Uno and voltage divider were used to collect sensor voltages (not pictured). In the case of capacitive sensing, an AD7745/46 evaluation board was used to collect sensor capacitances (not pictured).

via an Arduino Uno and voltage divider, while capacitance was measured with an AD7745/46 evaluation board. 3-axis testing was performed on a single taxel over 5 trials for each sensing modality.

4.6.2 Normal Force

A normal force resulted in a decrease in voltage or decrease in capacitance across all 3 pads as intended, Fig. 4.8. In the contact resistive approach, the taxel was unresponsive below 1 N, saturated above 8 N, and had a resolution of approximately 1 N. This was because below 1 N the pillar and pads were not yet in contact, while above 8 N the sensor can compress no further. The range can be tuned by adjusting the pillar height, pad height, and gap between pillar and pads, and is still useful for robotic manipulation applications [88]. However, by using capacitive sensing the range and resolution were significantly improved, up to 10 N and 100 mN, respectively. In this case, the interstitial PDMS dielectric enables finer motion of the pillar and pads without reaching saturation. This normal force dynamic range, 100:1, was greater than prior work [8], 42:1, due to the taller pillar and pad heights enabled from the milling manufacturing process (from 300 µm and 100 µm to 600 µm and 400 µm for the pillar and pad, respectively), although the gap was slightly larger (from 20 µm to 30 µm).

4.6.3 Shear Force

Shear forces were applied in the direction of each pad, Fig. 4.8. A small normal force of approximately 1-2 N was applied before shearing to improve contact between the acrylic probe and the taxel, while minimizing the influence of normal force on the results. A decrease in voltage was observed across the intended pad in each shear case, while the voltage of the other pads remained relatively unchanged. Shear

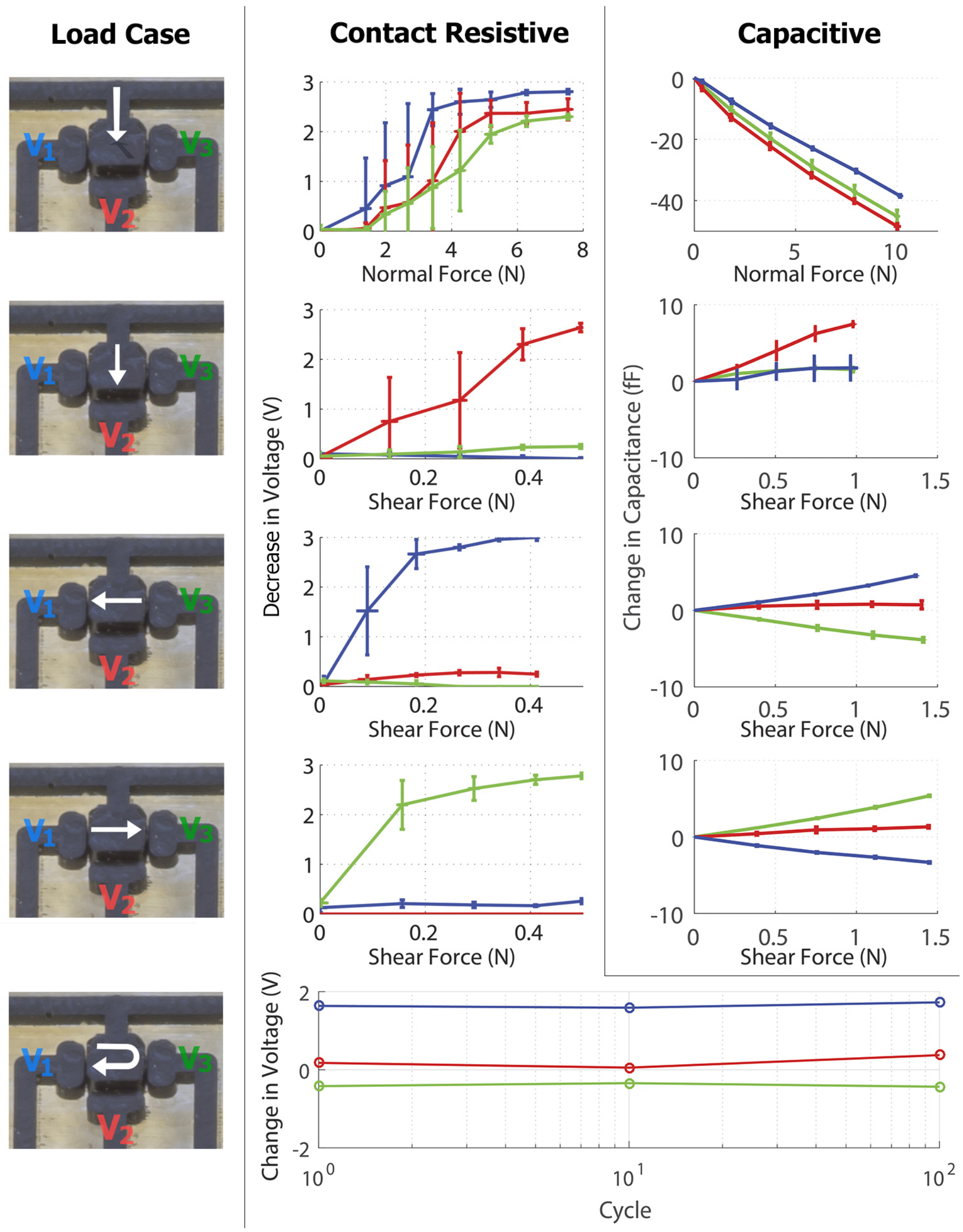

Figure 4.8: Sensor response to various load cases. Both contact resistive and capacitive transduction methods were characterized, and error bars represent 5 trials of a single taxel. Cyclic shear force testing was also carried out up to 100 cycles for the contact resistive sensor, and no hysteresis was observed.

force range and resolution were approximately 450 mN and 100 mN, respectively for the contact resistance sensors. Higher shear forces couldn't be tested as the probe was observed to slip. The dynamic range in the normal and shear directions were similar, which was expected due to the FEA guided design that selected a geometry that was a compromise between the two sensing directions. Using the capacitive approach, shear force range and resolution were 1500 mN and 50 mN, respectively. Higher shear forces were possible due to the increased surface area between the PDMS encapsulation and acrylic probe.

4.6.4 Cyclic Loading

Cyclic shear force testing was conducted on a contact resistive taxel by applying a moderate normal force of 4 N followed by loading and unloading of approximately 450 mN of shear force, Fig. 4.8 [Bottom]. The pad in the direction of loading, V_3, decreased in voltage while the opposite pad, V_1, increased in voltage, as intended. The magnitude of the increase in voltage was higher than the decrease due to the pad coming out of contact with pillar. The out-of-plane pad, V_2, experienced little change in voltage during testing with minor drift near the 100th cycle. No significant hysteresis was observed after 100 cycles.

4.6.5 Spatial Testing

A robot skin the size of an adult human hand was manufactured, and featured 12 contact resistive taxels with a total of 41 electrical leads, Fig. 4.9. Both normal

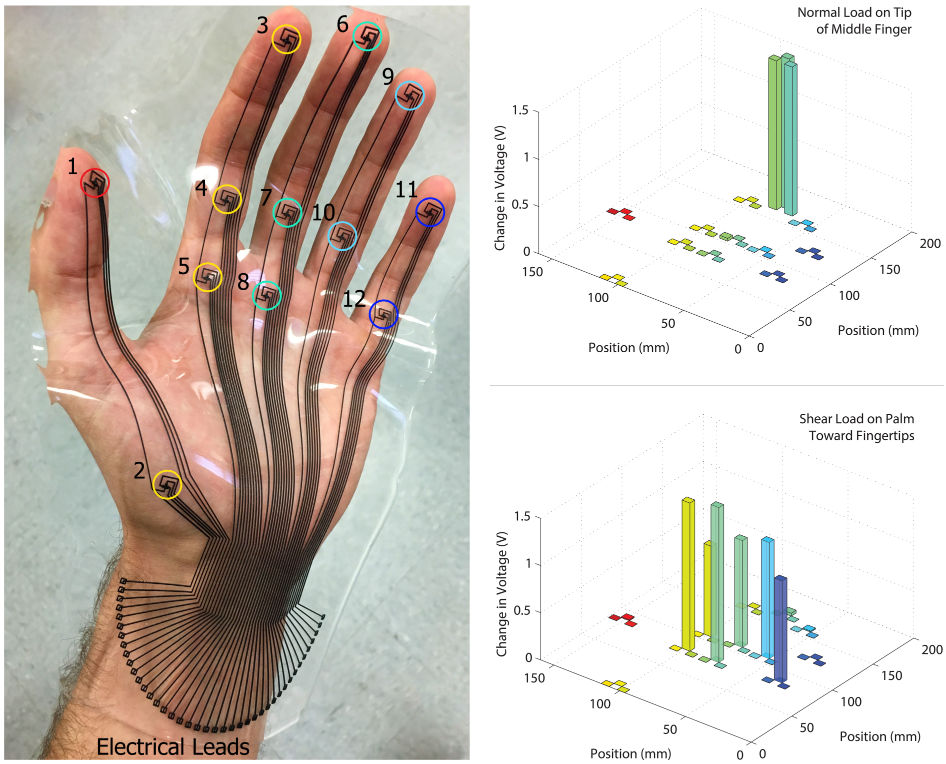

Figure 4.9: [Left] Robot skin covering an adult hand consisting of 12 contact resistive taxels with a total of 41 electrical leads. Taxels can sense shear and normal forces, and have features as small as 30 µm. [Top Right] Change in voltage of the robot skin when subjected to a normal load applied to the tip of the middle finger (taxel 6). Each pad at the taxel of interest changes in voltage with roughly the same magnitude. [Bottom Right] Change in voltage of the robot skin when subjected to an upward-pointing (toward the fingertips) shear load applied to the palm area (taxels 4, 5, 7, 8, 10, and 12). Pads in the direction of shear loading change in voltage while other pads remain relatively unchanged.

and shear tests were conducted while the robot skin was resting on a table. In normal testing, each taxel was pressed sequentially by hand, while in shear testing an acrylic plate was slid across the palm area. Snapshots of each test are show in Fig. 4.9. In all tests, low noise was seen in taxels not subjected to loading, where changes in voltage were less than 30 mV. In the normal force tests, all 3 pads at each taxel responded with roughly the same magnitude of change in voltage. Meanwhile, in the shear force tests, the pads which were being sheared towards experienced a change in voltage while out-of-plane pads remained relatively unchanged. This demonstrates the ability to achieve 3-axis force sensing over a large area using taxels with microscale features.

4.7 Closed-Loop Slip Detection

A one degree-of-freedom (DoF) gripper was prototyped to evaluate the robot skin's performance in a system, Fig. 4.10 [Top]. A single taxel using the contact resistive approach was mounted onto the tip of a robotic "thumb". Preliminary tests showed that the gripper was capable of producing a grasp force up to 7-8 N, and was operated around 2-4 N during testing. A closed-loop program was written to: 1) close the thumb until an object was gripped, 2) open the thumb if an object was gripped too tightly, and 3) grip tighter if a high downward-pointing shear force was detected. An Arduino Uno was used for controlling purposes, and the controller was looped through every 250 ms (i.e., 4 Hz sampling rate).

A test was designed to have the gripper grasp an object, and then load the

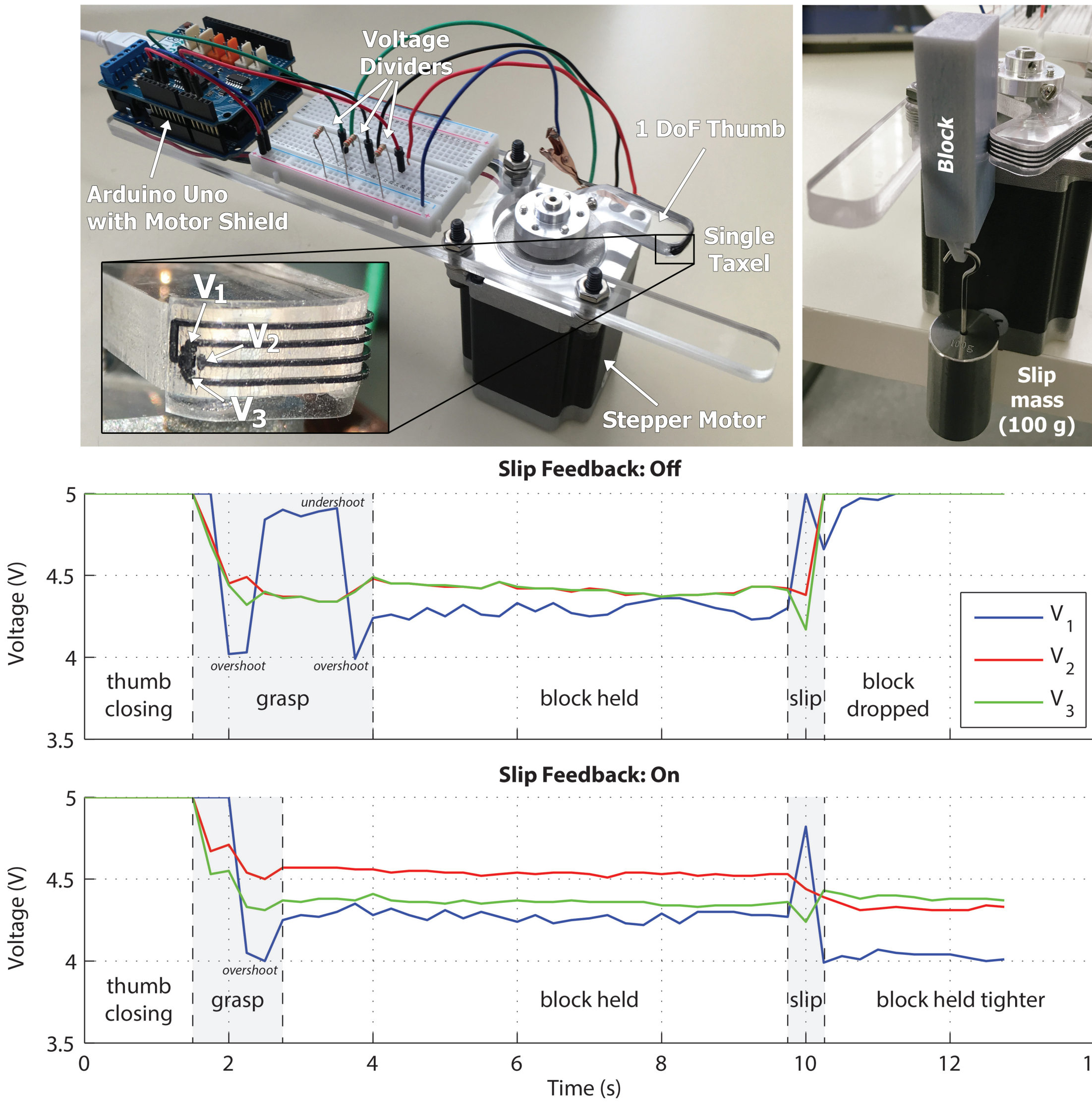

Figure 4.10: [Top] A one degree-of-freedom gripper equipped with a single contact resistive taxel controlled by an Arduino platform. A mass of 100 g was applied to the block after it was grasped to induce slip. [Bottom] Plots comparing the pad voltages without and with slip feedback control; the difference is evident in the gripper's response after 10 s.

object with a 100 g mass to induce slip. Two cases were tested: without and with slip feedback control, Fig. 4.10 [Bottom]. In both cases, the 3 pad voltages were nominal (5 V) while the thumb was closing, followed by undulations during thumb-object contact until a soft but stable grasp was reached. When the 100 g mass was applied (∼1 N of shear force), in both cases an increase in V_1 and decrease in V_3 was observed, which coincides with a downward-pointing shear force. In the first case, the object was dropped and the pad voltages returned to their nominal value. In the second case, the gripper grasped tighter to prevent dropping the block, and a decrease in the average pad voltage was observed indicating a higher normal force.

4.8 Extensions of Manufacturing Process

The developed milling-based manufacturing process and sensing modality is versatile and adaptable, and can be used to create other elastomer MEMS sensors. For example, the presented 3-axis tactile sensor architecture can be adjusted to accommodate a rat whisker adhered to the pillar, as well as four adjacent pads using a smaller 101 µm endmill (Microcut USA, 82004), Fig. 4.11. As the whisker is deformed in the shear directions, the pillar and pads come into physical contact resulting in a decrease in voltage. This could enable robots to navigate in the dark [105], or even be repurposed as a flow sensor in which a passing fluid deforms the whisker.

Another example is the creation of a flexible strain sensing skin, such as an artificial moth wing, Fig. 4.12. Using capacitive sensing, interdigitated structures elongate in the direction of strain and cause an increase in capacitance due to the

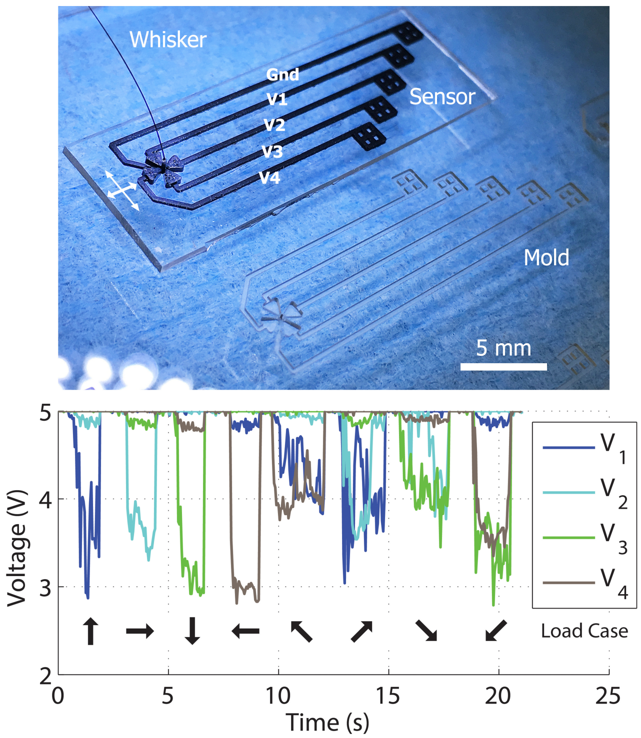

Figure 4.11: Rat whisker sensor. The taxel design was modified to accommodate 4 pads and a rat whisker press-fit into the center pillar. As the whisker is deflected, the pillar comes into physical contact with the adjacent pads. Eight load cases were tested: 4 cardinal directions and 4 diagonal directions.

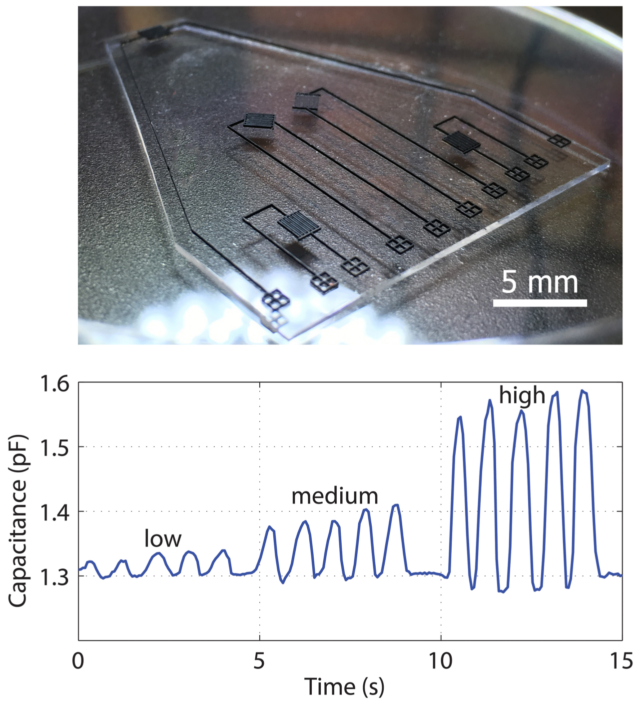

Figure 4.12: Artificial moth wing outfitted with an array of flexible strain gauges. A capacitive sensing modality was paired with interdigitated electrodes to sense low strains (100s of microstrain) across a wide range.

increase in interelectrode area [106]. In this case, a 101 µm in diameter endmill (Microcut USA, 82004) was used to create interdigitated structures with digit widths of 101 µm, depth of 200 µm, and electrode gaps of 90 µm. The mold covered an area of roughly 2 in by 4 in with strain gauges oriented in a fashion similar to other moth wing designs [107]. A single strain gauge on this wing was stretched by hand, and capacitance was collected using the aforementioned AD7745/46 evaluation board. Five cycles were stretched at low, medium, and high strains, where low strain was measured on the order of 100's of microstrain using digital calipers.

4.9 Limitations

Although rapid manufacturing of large area robot skins with 3-axis contact resistive sensing has been demonstrated, the most significant drawback of this particular modality was dynamic range. This can be partly mitigated by tuning the taxel geometry, but still lacks the dynamic range of some previous 3-axis sensors [21, 8]. In the future, dynamic range could potentially be improved by using a rounded contact area rather than flat; this may reduce the deviations between trials. However, capacitive sensing was able to dramatically improve dynamic range; from 8:1 to 100:1 in the normal direction, and from 5:1 to 30:1 in the shear directions. It was also found that at high normal forces (above 8 N), the taxels became relatively insensitive to shear forces as the compressed sensor could not deform further; this is an inherent limitation of the contact resistive approach.

During fabrication, a high amount of force is applied to the acrylic mold as the

CNT/PDMS is planarized by hand. During this step, it was found that small gaps tend to break. With a gap of 30 µm, yield was estimated at 80-90%. In the future, larger gaps could be fabricated to improve yield while also increasing the normal force range, or a more delicate planarization process could be employed using liquids like isopropyl alcohol (IPA). A metal instead of acrylic, such as aluminum or steel, could also be used as the stock material to improve gap yield strength.

The contact resistive sensor architecture left the sensing elements exposed to the environment, which could potentially lead to damage from repeated use. Also, conductive objects such as metals were not compatible with this architecture since they created an electrical short between the pillar and pads. A thin insulating film, such as plastic wrap, can be placed on top of the robot skin to mitigate this.

Electrical routing was fabricated in the same plane as the sensors, limiting the taxel areal density and number of pads per pillar. However, taxel density can increase if a smaller array (ex: 3 by 3 with a spacing of 3 mm, ideal for fingertips) is desired because the amount of routing is significantly less. A smaller diameter endmill for the routing could also be used, as was used in the rat whisker sensor to enable 4 pads per pillar. A more integrated approach would be to mill vias and traces directly into the backside of the robot skin. This step would be done just before peeling the robot skin from the mold (i.e., before the last step in Fig. 4.4). Then, the vias and traces would be refilled and planarized with CNT/PDMS.

4.10 Conclusion

This work presented a rapid and affordable manufacturing process based on CNC milling, and featured a 3-axis tactile sensor architecture that can use either contact resistance or capacitance to sense forces. The manufacturing process produced features as small as 30 µm, without the need of a clean room, over an area as large as an adult hand. Dynamic range was approximately 8:1 and 5:1 in the shear and normal directions when measuring contact resistance, while capacitive sensing can be used to drastically improve dynamic range up to 100:1. A robot skin was shown to measure shear and normal forces across a large area, and a one DoF gripper was built with a single taxel to demonstrate successful detection and prevention of slip. The ability to quickly manufacture flexible skins will help accelerate the pace of elastomer-based sensor research, and result in new conductive elastomeric sensors.

Acknowledgment

This work was supported by NASA's National Robotics Initiative (NRI) grant #NNX12AM02G. The authors would like to thank Anne En-Tzu Yang and Dr. Mitra Hartmann, of Northwestern University, for their assistance in the development of the rat whisker sensor. The authors would also like to thank Will Weston-Dawkes and Hee-Sup Shin for original demonstrations of the interdigitated strain sensor.

Chapter 5

Conclusions

5.1 Summary

A manufacturing process which utilizes a reusable mold to create various all-elastomer tactile sensors for robotics has been presented. The mold is refilled with a conductive polymer, and can be fabricated across multiple length scales from 10's of microns to millimeters. By orienting the conductive features in strategic ways, capacitors and contact resistive geometries were fashioned to measure tactile forces in three axes. Finite element simulations and analytical models of the sensor's response to deformation were developed and agreed well with the experimental data. A high dynamic force range in both shear and normal directions was achieved using capacitive sensing. A large area skin with microscale features was made using a CNC-based manufacturing process. A single contact resistive taxel was integrated into a 1 degree of freedom robotic gripper for closed-loop slip detection. This work serves to advance the field of elastomeric sensors for robotic applications, and may benefit other flexible applications including moth wings strain sensing, at-scale rat whisker sensing, fluid flow sensing, and human-exoskeleton interfacing.

5.2 List of Contributions

- Novel all-elastomer sensor geometries for normal and shear force sensing
- Modeling of sensor mechanics using both a reduced order analytical model and a multiphysics finite element model
- A rapid and inexpensive manufacturing process to produce microscale features over a large area

5.3 Comparison to Target Metrics and Future Work

A table of target metrics was detailed earlier, Table 1.1, and most of these values were met while others remain a challenge or haven't been attempted yet. The force range and resolution, 10 N and 50 mN respectively, have been met. A normal force range of 10 N was demonstrated, and a shear force resolution of 50 mN was also demonstrated. This was achieved by avoiding air-gap capacitors. A force accuracy of 10 mN has not yet been attempted or validated. Therefore, there is a need to calibrate the sensors and test whether they can accurately assess forces accurately. A spatial density of 1 mm spacing was targeted, and a sensor with 3 mm spacing was developed with a spatial resolution of 1.5 mm. A smaller density can be achieved with smaller sensors and wiring, but was mostly limited by the need for in plane wiring. The desired number of sensing axes was 3, and all 3 axes have been met using a novel sensor architecture. A thin sensor of less than 500 µm has been partially met; the PDMS layer was less than 500 µm, but including the conductive PDMS layer is still over 500 µm (but under 1 mm). A layer of PDMS can be spin coated in the future to further reduce overall skin thickness. The desired materials were to be compliant and conductive, and by using PDMS a qualitatively compliant sensor was achieved. However, conductivies on the order of 100 $\Omega \cdot \mu m$ were only achieved using Ag/PDMS but had low yield. CNT/PDMS was found to be approximately 1,000 times more conductive than carbon black/PDMS with high yield, and was sufficient for manufacturing and sensing purposes. Still, investigating ways to combine silver particles with elastomers like PDMS with high yield remains a subject of future work. With respect to electronics, power consumption and bandwidth were not investigated in this work. A sampling rate of more than 1 kHz was desired, however it was shown that slip can be detected with a sampling rate as small as 4 Hz. Future work will focus on simplifying electronics and strategies to minimize wiring for low power consumption, which is relevant to mobile applications such as prosthetics.

5.4 List of Completed Publications

- Alexi Charalambides and Sarah Bergbreiter. "All-elastomer in-plane mems capacitive tactile sensor for normal force detection." In Sensors, 2013 IEEE, pages 1-4. IEEE, 2013.

- Abraham Chen, Alexi Charalambides, and Sarah Bergbreiter. "High strength, low voltage microfabricated electroadhesives on nonconductive surfaces." In Hilton Head Workshop. Hilton Head Island, SC, 2014.

- Alexi Charalambides, Jian Cheng, Teng Li, and Sarah Bergbreiter. "3-axis all elastomer mems tactile sensor." In Micro Electro Mechanical Systems (MEMS), 2015 28th IEEE International Conference on, pages 726-729. IEEE, 2015.

- Alexi Charalambides and Sarah Bergbreiter. "A novel all-elastomer MEMS tactile sensor for high dynamic range shear and normal force sensing." Journal of Micromechanics and Microengineering. 25.9 (2015): 095009.

- Alexi Charalambides and Sarah Bergbreiter. "Milled micromolds for large area all-elastomer 'robot skin' with 3-axis tactile sensing via contact resistance." In Hilton Head Workshop. Hilton Head Island, SC, 2016.

- Kourosh M. Kalayeh, Alexi Charalambides (first co-author), Sarah Bergbreiter, Panos G. Charalambides. "Model and experimental validation of an all-elastomer in-plane capacitive tactile sensor." Provisionally accepted to IEEE Sensors Journal.

5.5 List of Future Publications

- Alexi Charalambides and Sarah Bergbreiter. "Rapid manufacturing of mechanoreceptive skins for slip detection in robotic grasping". In preparation.

5.6 List of Provisional Patents

- PS-2015-094, "All-elastomer 3-axis tactile sensing skin"

- PS-2015-176, "Micromilled manufacturing of all-elastomer 3-axis contact resistive tactile sensor arrays"

Appendix A

MATLAB

A.1 Find Step Values

This code was used to find the value of a step signal in the time domain. For example, in Fig. 3.11, a step signal can be seen which was collected from the AD capacitance board, and this code found the values of each step to greatly streamline post-processing.

```
function [values] = find_values(array,freq,tol)
% array - time domain step signal
% freq - length of chunks
% tol - tolerance between chunks of data
count = 1; % current value being sought
i = 1;
last_value = 1333337;
while i < length(array)
    signal_count = 0; % checking for 3 consecutive
        different values to signal a new value
    while signal_count < 3 && i < length(array)
        i_old = i;
```

```
        i = i + freq;
        if i < length(array) && abs(last_value -
            mean(array(i_old:i))) <= tol % tolerance
        else
            signal_count = signal_count + 1;
        end
    end
    if i < length(array)
        last_value = mean(array(i_old:i));
        values(count) = last_value;
        count = count + 1;
    end
end
```

A.2 Oxide Mask Calculator

During the microfabrication process, an oxide mask was etched with two precise depths. Knowing the etch rate of silicon dioxide in the Oxford Fluorine etcher, and knowing the desired DRIE depth, this code was used to calculate the depths of the oxide mask.

```
r = 1/187; % 1 um SiO2 per 187 um Si etched
d_p = 300; % depth of pillar (um)
d_t = 100; % depth of trace (um)
total_oxide = d_p*r % (um)
fluorine_etch = d_t*r % (um)
drie_time = d_p/2.1 % (min)
```

Appendix B

ANSYS

This script was run in ANSYS Mechanical APDL 14.0. It was used to study changes in capacitance of the 3-axis sensor as a function of normal displacement, shear displacement, and geometric parameters. These tasks and others were be performed by adjusting the "parameter sweep" variables, and "constants" variables. For additional material, see section 13.6 of the ANSYS manual "Low-Frequency Electromagnetic Analysis".

```
! ---- -------------------------- ----
! ---- Reset & prep output ----
! ---- -------------------------- ----

FINISH
/CLEAR

/CWD, 'C:\Users\Lab Admin\Documents\Alexi\ANSYS\scripting\JMM_FALL14\'

! ---- -------------------- ----
! ---- Parameter Sweep ----
```

```
! --- ------------------ ---

*DO,U_y,000.01E-6,000.01E-6,010E-6
*DO,U_x,000.01E-6,100.01E-6,050E-6

        ! --- Job name ---

        /FILNAME,output_1,0

        ! --- ---------------------- ---
        ! --- Mechanical Analysis ---
        ! --- ---------------------- ---

        /PREP7

        ! --- Constants ---

        dim_x=1600E-6
        dim_ybot=650E-6
        dim_ytop=1060E-6-dim_ybot

        pillar_x=1000E-6 ! pillar width (meter)
```

```
trace_x=250E-6 ! trace width
pillar_y=300E-6
trace_y=100E-6
electrode_g=20E-6

! --- Element type ---

ET,1,PLANE182,0,,2,,,0

! --- Material properties ---

! (1) cPDMS

TB,HYPER,1,,,OGDEN                ! TB,lab,mat,ntemp,npts,tbopt,eosopt,funcname
TBDATA,1,463106.593683            ! mu, shear modulus (Pa)
TBDATA,2,3.51526138807            ! a
TBDATA,3,1e-10                    ! d

! (2) PDMS

```

```
TB,HYPER,2,,,OGDEN               ! TB,lab,mat,ntemp,npts,tbopt,eosopt,funcname
TBDATA,1,225286.977321           ! mu, shear modulus (Pa)
TBDATA,2,3.97006318376           ! a
TBDATA,3,1e-10                   ! d

! --- Geometry and Meshing ---

! (0) prepare skeleton

RECTNG,-dim_x/2,dim_x/2,-dim_ybot,dim_ytop

MSHKEY,1
MSHAPE,0,2D
ESIZE,5E-6,
AMESH,ALL

! (1) pdms

NSEL,S,LOC,X,-9999E-6,9999E-6
ESLN,S,1,ALL
```

```
EMODIF,ALL,MAT,2

! (2) pillar

NSEL,S,LOC,X,-pillar_x/2,pillar_x/2
NSEL,R,LOC,Y,0,pillar_y
CM,elec1,NODE
ESLN,S,1,ALL
EMODIF,ALL,MAT,1

! (3) left electrode

NSEL,S,LOC,X,-trace_x-electrode_g-pillar_x/2,
    -electrode_g-pillar_x/2
NSEL,R,LOC,Y,0,trace_y
CM,elec2,NODE
ESLN,S,1,ALL
EMODIF,ALL,MAT,1

! (4) right electrode

```

```
NSEL,S,LOC,X,pillar_x/2+electrode_g,pillar_x/2
    +electrode_g+trace_x
NSEL,R,LOC,Y,0,trace_y
CM,elec3,NODE
ESLN,S,1,ALL
EMODIF,ALL,MAT,1

! --- Boundary conditions ---

! (1) displacements

NSEL,S,LOC,Y,dim_ytop
D,ALL,UX,U_x
D,ALL,UY,-U_y

! (2) fixed

NSEL,S,LOC,Y,-dim_ybot
CM,N_fixed,NODE
D,ALL,ALL,0

! --- Solve ---
```

```
ANTYPE,0 ! static analysis
ALLSEL,ALL
/SOLU
NLGEOM,ON
SOLVE
/POST1

! --- Plots ---

/SHOW,JPEG
PLNSOL,S,EQV

/SHOW,JPEG
PLNSOL,EPEL,EQV

! --- Reaction Force ---

CMSEL,S,N_fixed,
*GET,node_count,NODE,,count

F_x=0
```

```
F_y=0
N_i=0

*DO, i ,1 , node_count
        N_i=NDNEXT( N_i )

        F_xi=0
        *GET, F_xi ,NODE, N_i ,RF,FX
        F_x=F_x+F_xi

        F_yi=0
        *GET, F_yi ,NODE, N_i ,RF,FY
        F_y=F_y+F_yi
*ENDDO

! ——— ———————————————— ———
! ——— Electrical Analysis ———
! ——— ———————————————— ———

ALLSEL
/PREP7
UPCOORD,1 ,OFF            ! UPGEOM may also be used
```

```

! --- Element type ---

ET,2,PLANE121,,,0,0,0,0
EMODIF,ALL,TYPE,2

! --- Electrical properties ---

EMUNIT,MKS,
MP,PERX,1,2.5     ! C/PDMS
MP,PERX,2,2.5     ! PDMS

! --- Set Materials ---

NSEL,S,LOC,X,-9999E-6,9999E-6
ESLN,S,1,ALL
EMODIF,ALL,MAT,2

CMSEL,S,elec1
CMSEL,A,elec2
CMSEL,A,elec3
ESLN,S,1,ALL
```

```
        EMODIF,ALL,MAT,1

        ! --- Solve ---

        /SOLU
        ALLSEL
        CMATRIX,1,'elec',3,1,'capacitance'

        ! --- Reset ---

        FINISH
        PARSAV,SCALAR,LOOP_VARS,PARM,  ! save loop variables
        /CLEAR
        PARRES,NEW,LOOP_VARS,PARM,  ! load loop variables

*ENDDO
*ENDDO

FINISH
/CLEAR
*CFCLOS
```

Appendix C

CAMotics

This script was run in CAMotics 1.0.0. It's written in Tool Path Language, a proprietary language of CAMotics, and is able to automatically generate numerical control (NC) code that the milling machine can read and execute. This script creates a 6 by 6 array of 3-axis tactile sensors.

```

// 1) set constants

// machine
var h_safe = 0.7; // safe height above workpiece (mm)
var r_tool = 0.2032; // tool radius (mm) -- don't use more than 4 digits, and use good looking, not-long-reach 2 flute tools
tool(1); // Select tool

// sensor geometry
var gap = 0.03; // electrode gap (mm)
var length = 1; // pillar width (mm)
var depth_p = 0.600; // pillar depth (mm)
```

```
var depth_tr = 0.400; // trace depth (mm)
var spacing = 10; // spacing between sensors (mm)
var nodes = 6; // number of sensors (x by x, where x is Even)

// trace parameters
var dir = 0; // variable which adjusts direction of traces -- initialize to zero, define later
var offset = 0; // (mm) variable which adjusts distance that traces move away from the sensors -- initialize to zero, define later

// 2) set initial mill parameters

rotate(3.141592654/2); // rotate to align with milling X-axis (most sturdy)
translate((nodes-1)/2*spacing+0.0001, -(nodes-1)/2*spacing+0.0001 ,0.0001); // translate X, Y, and Z to add decimal points to output file
rapid({z: h_safe}); // Move to a safe height
rapid({x: 0, y: 0}); // Go to start position

```

```
// 3) mill mold

// taxels
feed(8.01);
speed(8000);

for (i = 1; i <= nodes; i = i + 1) {
  for (j = 1; j <= nodes; j = j + 1) {
    sensor((i-1)*spacing, (j-1)*spacing, length, length,
       depth_p, depth_tr, gap, h_safe, r_tool);
  }
}

// traces
feed(100.01);
speed(10000);

for (i = 1; i <= nodes; i = i + 1) {

  dir = 1;
  offset = 0;

```

```
  for (j = 1; j <= nodes; j = j + 1) {

    if (j == 1) {}
    else if (j <= nodes/2) {offset = offset + 2.5;}
    else if (dir == 1) {dir = -1;}
    else {offset = offset - 2.5;}

    trace((i-1)*spacing, (j-1)*spacing, length, length,
        depth_tr, gap, h_safe, dir, offset);

    // ground extension
    rapid({z: h_safe});
    rapid({x:(i-1)*spacing, y: (j-1)*spacing});
    icut({z: -h_safe-depth_tr});
    icut({x: -((length/2)+0.75)});

    //  ground lines
    if (j == nodes) {
      icut({y:-((nodes-1)*spacing)});
      if (i == nodes) {
        rapid({z: h_safe});
        irapid({y: ((nodes-1)*spacing/2)});
```

```
        icut({z: -h_safe-depth_tr});
        icut({x: -((nodes-1)*spacing+5)});
        icut({y: -((nodes-1)/2*spacing+50)});
        ipad()
      }
    }

  }
}

// 4) end milling

rapid({z: h_safe}); // Move back to safe height
speed(0); // Stop spinning

// %%%%%%%%%%%%%%%%%%%%%%%%%%%%%%%%%%%%%%%%%%%%%%%%%%

// rectangular cut function

function rectangle(pos_x, pos_y, length_x, length_y, depth,
   h_safe, r_tool) {
  // move into position
```

```
  rapid({z: h_safe});
  rapid({x: pos_x, y: pos_y});
  // lower, move to "inside" corner of square
  irapid({x: -(length_x/2)+r_tool, y:
     -(length_y/2)+(r_tool)});
  icut({z: -h_safe-depth});
  // remove perimeter material
  icut({x: length_x-2*r_tool});
  icut({y: length_y-2*r_tool});
  icut({x: -(length_x-2*r_tool)});
  icut({y: -(length_y-2*r_tool)});
  // if too big, call recursively at smaller length
     proportional to the tool radius
  if (length_x - 2*r_tool > 2*r_tool && length_y - 2*r_tool
     > 2*r_tool) {
    rectangle(pos_x, pos_y, length_x-2*r_tool,
       length_y-2*r_tool, depth, h_safe, r_tool)
  }
}

// %%%%%%%%%%%%%%%%%%%%%%%%%%%%%%%%%%%%%%%%%%%%%%%%%%

```

```
// sensor function

function sensor(pos_x, pos_y, length_x, length_y, depth_p,
    depth_tr, gap, h_safe, r_tool) {

  // make electrodes
  rectangle(pos_x, pos_y-(length_y/2+gap+length_y/4),
      length_x, length_y/2, depth_tr, h_safe, r_tool) //
      bottom
  rectangle(pos_x+(length_x/2+gap+length_x/4), pos_y,
      length_x/2, length_y, depth_tr, h_safe, r_tool) //
      right
  rectangle(pos_x, pos_y+(length_y/2+gap+length_y/4),
      length_x, length_y/2, depth_tr, h_safe, r_tool) // top
  //rectangle(pos_x-(length_x/2+gap+length_x/4), pos_y,
      length_x/2, length_y, depth_tr, h_safe, r_tool) // left

  // make pillar
  rectangle(pos_x, pos_y, length_x, length_y, depth_p,
      h_safe, r_tool)

}
```

```
// %%%%%%%%%%%%%%%%%%%%%%%%%%%%%%%%%%%%%%%%%%%%%%%%%%%%%%%

// sensor trace function

function trace(pos_x, pos_y, length_x, length_y, depth, gap, h_safe, dir, offset) {

  // bottom
  rapid({z: h_safe}); // safe position
  rapid({x: pos_x, y: pos_y}); // center over sensor
  irapid({y: -dir*(length_y/2 + gap + length_y/4)});
  icut({z: -h_safe-depth});
  icut({y: -dir*0.75});
  icut({x: 0.75+offset});
  icut({y: -dir*53});
  ipad()

  // right
  rapid({z: h_safe}); // safe position
  rapid({x: pos_x, y: pos_y}); // center over sensor
  irapid({x: length_x/2 + gap + length_x/4});
```

```
  icut({z: -h_safe-depth});
  icut({x: 0.7+offset});
  icut({y: -dir*51.5});
  ipad()

  // top
  rapid({z: h_safe}); // safe position
  rapid({x: pos_x, y: pos_y}); // center over sensor
  irapid({y: dir*(length_y/2 + gap + length_y/4)});
  icut({z: -h_safe-depth});
  icut({y: dir*0.75});
  icut({x: 2.25+offset});
  icut({y: -dir*50});
  ipad()

}

// %%%%%%%%%%%%%%%%%%%%%%%%%%%%%%%%%%%%%%%%%%%%%%%%%%%%%%%%%%%%%%%%%%%

// trace incremental pad function

function ipad() {
```

```
  var length = 2; // length of square pad (mm)
  icut({x: length});
  icut({y: -length/2});
  icut({x: -length});
  icut({y: length});
  icut({x: length});
  icut({y: -length/2});
  icut({x: -length/2});
  icut({y: -length/2});
  icut({y: length});
}
```

Appendix D

Arduino

The following code was used in the 1 degree of freedom gripper for closed-loop slip detection, and was implemented on an Arduino Uno with an Arduino Motor Shield. The Arduino collected 3 voltages from a single taxel, and used that data to actuate a stepper motor. The stepper motor was controlled based on open-source code by Randy Sarafan (http://www.instructables.com/id/Arduino-Motor-Shield-Tutorial/).

```

// voltage read pins
const int ReadSensor[] = {0, 2, 3, 4};

// circuit variables
const float Vin = 5;                    // Arduino voltage (V)
float Vout = 0;                         // measured voltage (V)
float V0[] = {0, 0, 0, 0};              // last array of measured voltages (V)
```

```
float V1[] = {0, Vin, Vin, Vin};    // current array of measured voltages (V)

// sampling variables
const float period = 250;  // sampling period (ms)
float t = 0;                               // current time (ms)

// logic variables
int JustSlipped = 0;                        // boolean if it just slipped
int JustOverGripped = 0;           // boolean if it just overgripped
const int StandByMax = 10;    // count of "gripped" samples until overgrip is disabled (set to 9999... to disable)
int StandBy = StandByMax;

// control parameters
const int SlipControl = 1;    // boolean that turns on/off slip feedback control during stand by
const float P1 = 4.75;         // below this average voltage is "gripped"
```

```
const float P2 = 4.42;        // below this average voltage is "over gripped"
const float P3 = 1.10;        // differential voltage that triggers "slip"
const float P4 = -0.2;        // change in top voltage that triggers "release"
const float P5 = 0.4;         // change in bot voltage that triggers "release"

// stepper motor phase
int phase = 1;

/////////////////////////////////////////////////////////////////////////////////////

void setup() {

  // text output setup
  Serial.begin(9600);
  Serial.println("");
  Serial.println("t V1 V2 V3");

  // motor setup
```

```
  pinMode(12, OUTPUT); //CH A -- HIGH = forwards and LOW =
      backwards
  pinMode(13, OUTPUT); //CH B -- HIGH = forwards and LOW =
      backwards
  pinMode(9, OUTPUT); //brake (disable) CH A
  pinMode(8, OUTPUT); //brake (disable) CH B

}

//////////////////////////////////////////////////////////////////////////////////////////////

void loop() {

  Serial.print(t);
  Serial.print(" ");

  // find voltages

  for (int i = 1; i <= 3; i++) {

    V0[i] = V1[i]; // store last samples' voltages

```

```
    Vout = analogRead(ReadSensor[i]);
    Vout = Vout * (Vin / 1023);

    // display values
    Serial.print(Vout);
    Serial.print(" ");

    V1[i] = Vout; // store current voltages

  }

  // close gripper
  if ((V1[1] + V1[2] + V1[3]) / 3 > P1) {
    phase = close_motor(phase);
    StandBy = StandByMax;
  }

  // feedback control
  else {
    Serial.print("Gripped. ");
    if (StandBy <= 0) {
          Serial.print("Stand By. ");
```

```
    }

    // proportion - too tight
    if ((V1[1] + V1[2] + V1[3]) / 3 < P2 && JustOverGripped
        == 0 && StandBy > 0) {
      Serial.print("Over-gripped. ");
      phase = open_motor(phase+2);
      JustSlipped = 0;
      JustOverGripped = 1;
      StandBy = StandByMax;
    }

    // proportional - down
    else if (V1[1] - V1[3] > P3) {
      if (StandBy > 0 || SlipControl == 1) {
        Serial.print("Slip. ");
        phase = close_motor(phase);
        JustSlipped = 1;
        JustOverGripped = 0;
      }
    }

```

```
    // derivative - up
    else if ( V1[1] - V0[1] < P4 && V1[3] - V0[3] > P5 &&
        JustSlipped == 0) {
      Serial.print("Release. ");
      for (int i = 1; i <= 15; i++) {
        phase = open_motor(phase);
        delay(100);
      }
      t = t + 1500;
      JustSlipped = 0;
      JustOverGripped = 0;
      StandBy = StandByMax;
    }

    else {
      JustSlipped = 0;
      JustOverGripped = 0;
      StandBy = StandBy - 1;
    }

  }

```

```
  // reset
  Serial.println("");
  delay(period);
  t = t + period;

}

//////////////////////////////////////////////////////////////////////////////

int close_motor(int phase) {

  if (phase == 1) {
    digitalWrite(9, LOW);   //ENABLE CH A
    digitalWrite(8, HIGH); //DISABLE CH B

    digitalWrite(12, HIGH);    //Sets direction of CH A
    analogWrite(3, 255);    //Moves CH A
  }

  if (phase == 2) {
    digitalWrite(9, HIGH);   //DISABLE CH A
    digitalWrite(8, LOW); //ENABLE CH B
```

```

    digitalWrite(13, LOW);    //Sets direction of CH B ***
    analogWrite(11, 255);    //Moves CH B
  }

  if (phase == 3) {
    digitalWrite(9, LOW);   //ENABLE CH A
    digitalWrite(8, HIGH); //DISABLE CH B

    digitalWrite(12, LOW);    //Sets direction of CH A
    analogWrite(3, 255);    //Moves CH A
  }

  if (phase == 4) {
    digitalWrite(9, HIGH);   //DISABLE CH A
    digitalWrite(8, LOW); //ENABLE CH B

    digitalWrite(13, HIGH);    //Sets direction of CH B ***
    analogWrite(11, 255);    //Moves CH B
  }

  phase = phase + 1;
```

```
  if (phase > 4) {
    phase = 1;
  }
  return phase;

}

////////////////////////////////////////////////////////////////////////////////

int open_motor(int phase) {

  if (phase == 1) {
    digitalWrite(9, LOW);  //ENABLE CH A
    digitalWrite(8, HIGH); //DISABLE CH B

    digitalWrite(12, HIGH);   //Sets direction of CH A
    analogWrite(3, 255);   //Moves CH A
  }

  if (phase == 2) {
    digitalWrite(9, HIGH);  //DISABLE CH A
    digitalWrite(8, LOW); //ENABLE CH B
```

```
    digitalWrite(13, HIGH);    //Sets direction of CH B ***
    analogWrite(11, 255);    //Moves CH B
  }

  if (phase == 3) {
    digitalWrite(9, LOW);   //ENABLE CH A
    digitalWrite(8, HIGH); //DISABLE CH B

    digitalWrite(12, LOW);    //Sets direction of CH A
    analogWrite(3, 255);    //Moves CH A
  }

  if (phase == 4) {
    digitalWrite(9, HIGH);   //DISABLE CH A
    digitalWrite(8, LOW); //ENABLE CH B

    digitalWrite(13, LOW);    //Sets direction of CH B ***
    analogWrite(11, 255);    //Moves CH B
  }

  phase = phase + 1;
```

```
    if (phase > 4) {
        phase = 1;
    }
    return phase;

}
```

Bibliography

[1] David J Beebe, Arthur S Hsieh, Denice D Denton, and Robert G Radwin. A silicon force sensor for robotics and medicine. *Sensors and Actuators A: Physical*, 50(1):55–65, 1995.

[2] Felix Beyeler, Simon Muntwyler, and Bradley J Nelson. A six-axis mems force–torque sensor with micro-newton and nano-newtonmeter resolution. *Microelectromechanical Systems, Journal of*, 18(2):433–441, 2009.

[3] Yong-Lae Park, Bor-Rong Chen, and Robert J Wood. Design and fabrication of soft artificial skin using embedded microchannels and liquid conductors. *Sensors Journal, IEEE*, 12(8):2711–2718, 2012.

[4] Hyung-Kew Lee, Jaehoon Chung, Sun-Il Chang, and Euisik Yoon. Normal and shear force measurement using a flexible polymer tactile sensor with embedded multiple capacitors. *Microelectromechanical Systems, Journal of*, 17(4):934–942, 2008.

[5] Jan Peirs, Joeri Clijnen, Dominiek Reynaerts, Hendrik Van Brussel, Paul Herijgers, Brecht Corteville, and Sarah Boone. A micro optical force sensor for force feedback during minimally invasive robotic surgery. *Sensors and Actuators A: Physical*, 115(2):447–455, 2004.

[6] George C Lopez, Alan J Rosenbloom, Victor W Weedn, and Kaigham J Gabriel. In situ fabricated microchannels using porous polymer and xenon difluoride etchant. In *Micro Total Analysis Systems 2002*, pages 934–936. Springer, 2002.

[7] Kourosh Kalayeh, Alexi Charalambides, Sarah Bergbreiter, and Panos Charalambides. Development and experimental validation of a non-linear, all-elastomer in-plane capacitive pressure sensor model. *IEEE Sensors Journal*, TBD, 2016.

[8] Alexi Charalambides and Sarah Bergbreiter. A novel all-elastomer mems tactile sensor for high dynamic range shear and normal force sensing. *Journal of Micromechanics and Microengineering*, 25(9):095009, 2015.

[9] Le Cai, Li Song, Pingshan Luan, Qiang Zhang, Nan Zhang, Qingqing Gao, Duan Zhao, Xiao Zhang, Min Tu, Feng Yang, et al. Super-stretchable, transparent carbon nanotube-based capacitive strain sensors for human motion detection. *Scientific reports*, 3, 2013.

[10] Mark H Lee and Howard R Nicholls. Review article tactile sensing for mechatronicsa state of the art survey. *Mechatronics*, 9(1):1–31, 1999.

[11] J Dargahi and S Najarian. Human tactile perception as a standard for artificial tactile sensinga review. *The International Journal of Medical Robotics and Computer Assisted Surgery*, 1(1):23–35, 2004.

[12] Johan Tegin and Jan Wikander. Tactile sensing in intelligent robotic manipulation-a review. *Industrial Robot: An International Journal*, 32(1):64–70, 2005.

[13] Sarah Walsh, Daniel Barta, Ryan Stephan, and Stephen Gaddis. Next generation life support (ngls): High performance eva glove (hpeg) technology development element. http://ntrs.nasa.gov/archive/nasa/casi.ntrs.nasa.gov/20150023265.pdf, 2015. [Online; accessed 12-May-2016].

[14] Aaron M Dollar and Hugh Herr. Lower extremity exoskeletons and active orthoses: challenges and state-of-the-art. *Robotics, IEEE Transactions on*, 24(1):144–158, 2008.

[15] Pinyo Puangmali, Kaspar Althoefer, Lakmal D Seneviratne, Declan Murphy, and Prokar Dasgupta. State-of-the-art in force and tactile sensing for minimally invasive surgery. *Sensors Journal, IEEE*, 8(4):371–381, 2008.

[16] Robert O Ambrose, Robert T Savely, S Michael Goza, Philip Strawser, Myron Diftler, Ivan Spain, Nicolaus Radford, et al. Mobile manipulation using nasa's robonaut. In *Robotics and Automation, 2004. Proceedings. ICRA'04. 2004 IEEE International Conference on*, volume 2, pages 2104–2109. IEEE, 2004.

[17] Ravinder S Dahiya, Giorgio Metta, Maurizio Valle, and Giulio Sandini. Tactile sensing from humans to humanoids. *Robotics, IEEE Transactions on*, 26(1):1–20, 2010.

[18] Hanna Yousef, Mehdi Boukallel, and Kaspar Althoefer. Tactile sensing for dexterous in-hand manipulation in roboticsa review. *Sensors and Actuators A: physical*, 167(2):171–187, 2011.

[19] Eun-Soo Hwang, Jung-hoon Seo, and Yong-Jun Kim. A polymer-based flexible tactile sensor for both normal and shear load detections and its application for robotics. *Microelectromechanical Systems, Journal of*, 16(3):556–563, 2007.

[20] Hyung-Kew Lee, Jaehoon Chung, Sun-Il Chang, and Euisik Yoon. Real-time measurement of the three-axis contact force distribution using a flexible capacitive polymer tactile sensor. *Journal of Micromechanics and Microengineering*, 21(3):035010, 2011.

[21] Chih-Fan Hu, Wang-Shen Su, and Weileun Fang. Development of patterned carbon nanotubes on a 3d polymer substrate for the flexible tactile sensor application. *Journal of Micromechanics and Microengineering*, 21(11):115012, 2011.

[22] Ming-Yuan Cheng, Chun-Liang Lin, Yu-Tse Lai, and Yao-Joe Yang. A polymer-based capacitive sensing array for normal and shear force measurement. *Sensors*, 10(11):10211–10225, 2010.

[23] Soonjae Pyo, Jae-Ik Lee, Min-Ook Kim, Taeyoung Chung, Yongkeun Oh, Soo-Chul Lim, Joonah Park, and Jongbaeg Kim. Development of a flexible three-axis tactile sensor based on screen-printed carbon nanotube-polymer composite. *Journal of Micromechanics and Microengineering*, 24(7):075012, 2014.

[24] Cheng-Wen Ma, Li-Sheng Hsu, Jui-Chang Kuo, and Yao-Joe Yang. A flexible tactile and shear sensing array fabricated using a novel buckypaper patterning technique. *Sensors and Actuators A: Physical*, 231:21–27, 2015.

[25] Yoshiyuki Ohmura, Yasuo Kuniyoshi, and Akihiko Nagakubo. Conformable and scalable tactile sensor skin for curved surfaces. In *Robotics and Automation, 2006. ICRA 2006. Proceedings 2006 IEEE International Conference on*, pages 1348–1353. IEEE, 2006.

[26] John A Pelesko and David H Bernstein. *Modeling Mems and Nems*. CRC press, 2002.

[27] Bart J Kane, Mark R Cutkosky, and Gregory TA Kovacs. Cmos-compatible traction stress sensor for use in high-resolution tactile imaging. *Sensors and Actuators A: Physical*, 54(1):511–516, 1996.

[28] Tao Mei, Wen J Li, Yu Ge, Yong Chen, Lin Ni, and Ming Ho Chan. An integrated mems three-dimensional tactile sensor with large force range. *Sensors and Actuators A: Physical*, 80(2):155–162, 2000.

[29] Cheng-Ting Ko, Sheng-Hsiang Tseng, and Michael SC Lu. A cmos micromachined capacitive tactile sensor with high-frequency output. *Microelectromechanical Systems, Journal of*, 15(6):1708–1714, 2006.

[30] Mária Ádám, Tibor Mohácsy, Péter Jónás, Csaba Dücső, Éva Vázsonyi, and István Bársony. Cmos integrated tactile sensor array by porous si bulk micromachining. *Sensors and Actuators A: Physical*, 142(1):192–195, 2008.

[31] Chang Liu. Recent developments in polymer mems. *Advanced Materials*, 19(22):3783–3790, 2007.

[32] Darren J. Lipomi, Michael Vosgueritchian, Benjamin C-K. Tee, Sondra L. Hellstrom, Jennifer A. Lee, Courtney H. Fox, and Zhenan Bao. Skin-like pressure and strain sensors based on transparent elastic films of carbon nanotubes. *Nature Nanotechnology*, 6(12):788–792, October 2011.

[33] M Kujawski, JD Pearse, and E Smela. Elastomers filled with exfoliated graphite as compliant electrodes. *Carbon*, 48(9):2409–2417, 2010.

[34] XZ Niu, SL Peng, LY Liu, WJ Wen, and Ping Sheng. Characterizing and patterning of pdms-based conducting composites. *Advanced Materials*, 19(18):2682–2686, 2007.

[35] Anuj R Madaria, Akshay Kumar, and Chongwu Zhou. Large scale, highly conductive and patterned transparent films of silver nanowires on arbitrary substrates and their application in touch screens. *Nanotechnology*, 22(24):245201, 2011.

[36] Feng Xu and Yong Zhu. Highly conductive and stretchable silver nanowire conductors. *Advanced Materials*, 24(37):5117–5122, 2012.

[37] James Wissman, Ariel Perez-Rosado, Alex Edgerton, Benjamin M Levi, Zeynep N Karakas, Mark Kujawski, Alyssa Philipps, Nicholas Papavizas, Danielle Fallon, Hugh A Bruck, et al. New compliant strain gauges for self-sensing dynamic deformation of flapping wings on miniature air vehicles. *Smart Materials and Structures*, 22(8):085031, 2013.

[38] Luc Maffli, Samuel Rosset, and HR Shea. Zipping dielectric elastomer actuators: characterization, design and modeling. *Smart Materials and Structures*, 22(10):104013, 2013.

[39] Aaron P Gerratt and Sarah Bergbreiter. Microfabrication of compliant all-polymer mems thermal actuators. *Sensors and Actuators A: Physical*, 177:16–22, 2012.

[40] Stephanie Perichon Lacour, Sigurd Wagner, Zhenyu Huang, and Z Suo. Stretchable gold conductors on elastomeric substrates. *Applied physics letters*, 82(15):2404–2406, 2003.

[41] Chao-Xuan Liu and Jin-Woo Choi. Patterning conductive pdms nanocomposite in an elastomer using microcontact printing. *Journal of Micromechanics and Microengineering*, 19(8):085019, 2009.

[42] PJ French and AGR Evans. Piezoresistance in polysilicon and its applications to strain gauges. *Solid-State Electronics*, 32(1):1–10, 1989.

[43] Jien Cao, Qian Wang, and Hongjie Dai. Electromechanical properties of metallic, quasimetallic, and semiconducting carbon nanotubes under stretching. *Physical review letters*, 90(15):157601, 2003.

[44] Al L Window, Geoffry S Holister, et al. *Strain gauge technology.* Applied science publishers, 1982.

[45] Michael D Dickey, Ryan C Chiechi, Ryan J Larsen, Emily A Weiss, David A Weitz, and George M Whitesides. Eutectic gallium-indium (egain): A liquid metal alloy for the formation of stable structures in microchannels at room temperature. *Advanced Functional Materials*, 18(7):1097–1104, 2008.

[46] Letizia Ventrelli, Lucia Beccai, Virgilio Mattoli, Arianna Menciassi, and Paolo Dario. Development of a stretchable skin-like tactile sensor based on polymeric composites. In *Robotics and Biomimetics (ROBIO), 2009 IEEE International Conference on*, pages 123–128. IEEE, 2009.

[47] Daniel J Cohen, Debkishore Mitra, Kevin Peterson, and Michel M Maharbiz. A highly elastic, capacitive strain gauge based on percolating nanotube networks. *Nano letters*, 12(4):1821–1825, 2012.

[48] Aaron P Gerratt, Hadrien O Michaud, and Stéphanie P Lacour. Elastomeric electronic skin for prosthetic tactile sensation. *Advanced Functional Materials*, 25(15):2287–2295, 2015.

[49] Roger Gassert, Roland Moser, Etienne Burdet, and Hannes Bleuler. Mri/fmri-compatible robotic system with force feedback for interaction with human motion. *Mechatronics, IEEE/ASME Transactions on*, 11(2):216–224, 2006.

[50] Gregory S Fischer, Iulian Iordachita, Csaba Csoma, Junichi Tokuda, Simon P DiMaio, Clare M Tempany, Nobuhiko Hata, and Gabor Fichtinger. Mri-compatible pneumatic robot for transperineal prostate needle placement. *Mechatronics, IEEE/ASME Transactions on*, 13(3):295–305, 2008.

[51] Miao Yu and B Balachandran. Acoustic measurements using a fiber optic sensor system. *Journal of Intelligent Material Systems and Structures*, 14(7):409–414, 2003.

[52] Hao Su and Gregory S Fischer. A 3-axis optical force/torque sensor for prostate needle placement in magnetic resonance imaging environments. In *Technologies for Practical Robot Applications, 2009. TePRA 2009. IEEE International Conference on*, pages 5–9. IEEE, 2009.

[53] Norihisa Takahashi, Mitsunori Tada, Jun Ueda, Yoshio Matsumoto, and Tsukasa Ogasawara. An optical 6-axis force sensor for brain function analysis using fmri. In *Sensors, 2003. Proceedings of IEEE*, volume 1, pages 253–258. IEEE, 2003.

[54] Roger Gassert, Ludovic Dovat, Olivier Lambercy, Y Ruffieux, Dominique Chapuis, G Ganesh, Etienne Burdet, and Hannes Bleuler. A 2-dof fmri compatible haptic interface to investigate the neural control of arm movements. In *Robotics and Automation, 2006. ICRA 2006. Proceedings 2006 IEEE International Conference on*, pages 3825–3831. IEEE, 2006.

[55] Avrum D Hollinger and Marcelo M Wanderley. Mri-compatible optically-sensed cello. In *Sensors, 2013 IEEE*, pages 1–4. IEEE, 2013.

[56] Barrett Heyneman and Mark R Cutkosky. Slip classification for dynamic tactile array sensors. *The International Journal of Robotics Research*, 2015.

[57] Koichi Nishiwaki, Tomomichi Sugihara, Satoshi Kagami, Fumio Kanehiro, Masayuki Inaba, and Hirochika Inoue. Design and development of research platform for perception-action integration in humanoid robot: H6. In *Intelligent Robots and Systems, 2000.(IROS 2000). Proceedings. 2000 IEEE/RSJ International Conference on*, volume 3, pages 1559–1564. IEEE, 2000.

[58] Ryosuke Tajima, Satoshi Kagami, Masayuki Inaba, and Hirochika Inoue. Development of soft and distributed tactile sensors and the application to a humanoid robot. *Advanced Robotics*, 16(4):381–397, 2002.

[59] Aaron P Gerratt, Nicolas Sommer, Stéphanie P Lacour, and Aude Billard. Stretchable capacitive tactile skin on humanoid robot fingersfirst experiments and results. In *Humanoid Robots (Humanoids), 2014 14th IEEE-RAS International Conference on*, pages 238–245. IEEE, 2014.

[60] Oliver Kerpa, Karsten Weiss, and Heinz Worn. Development of a flexible tactile sensor system for a humanoid robot. In *Intelligent Robots and Systems, 2003.(IROS 2003). Proceedings. 2003 IEEE/RSJ International Conference on*, volume 1, pages 1–6. IEEE, 2003.

[61] Haruhisa Kawasaki, Tsuneo Komatsu, and Kazunao Uchiyama. Dexterous anthropomorphic robot hand with distributed tactile sensor: Gifu hand ii. *Mechatronics, IEEE/ASME Transactions on*, 7(3):296–303, 2002.

[62] Giorgio Metta, Giulio Sandini, David Vernon, Lorenzo Natale, and Francesco Nori. The icub humanoid robot: an open platform for research in embodied cognition. In *Proceedings of the 8th workshop on performance metrics for intelligent systems*, pages 50–56. ACM, 2008.

[63] Gereon H Büscher, Risto Kõiva, Carsten Schürmann, Robert Haschke, and Helge J Ritter. Flexible and stretchable fabric-based tactile sensor. *Robotics and Autonomous Systems*, 63:244–252, 2015.

[64] Dana D Damian, Taylor H Newton, Rolf Pfeifer, and Allison M Okamura. Artificial tactile sensing of position and slip speed by exploiting geometrical features. *Mechatronics, IEEE/ASME Transactions on*, 20(1):263–274, 2015.

[65] Alexi Charalambides and Sarah Bergbreiter. All-elastomer in-plane mems capacitive tactile sensor for normal force detection. In *Sensors, 2013 IEEE*, pages 1–4. IEEE, 2013.

[66] S.C. Jacobsen, I.D. McGammon, K.B. Biggers, and R.P. Phillips. Design of tactile sensing systems for dextrous manipulators. *IEEE Control Systems Magazine*, 8:3–13, February 1988.

[67] R.S. Dahiya, G. Metta, M. Valle, and G. Sandini. Tactile sensing–from humans to humanoids. *IEEE Transactions on Robotics*, 26:1–20, February 2010.

[68] M Lee. Review article tactile sensing for mechatronicsa state of the art survey. *Mechatronics*, 9:1–31, February 1999.

[69] Joseph M. Romano, Kaijen Hsiao, Gunter Niemeyer, Sachin Chitta, and Katherine J. Kuchenbecker. Human-inspired robotic grasp control with tactile sensing. *IEEE Transactions on Robotics*, 27(6):1067 – 1079, 2011.

[70] Sami Haddadin, Alin Albu-Schaffer, Michael Strohmayr, Mirko Frommberger, and Gerd Hirzinger. Injury evaluation of human-robot impacts. In *IEEE International Conference on Robotics and Automation*, pages 2203–2204, Pasadena, CA, May 2008.

[71] Samson Phan, Zhan Fan Quek, Preyas Shah, Dongjun Shin, Zubair Ahmed, Oussama Khatib, and Mark Cutkosky. Capacitive skin sensors for robot impact monitoring. In *IEEE/RSJ International Conference on Intelligent Robots and Systems*, pages 2992–2997, San Francisco, CA, September 2011.

[72] L Ventrelli, L. Beccai, V. Mattoli, A. Menciassi, and P. Dario. Development of a stretchable skin-like tactile sensor based on polymeric composites. *IEEE Robotics and Biomimetics Conference Proceedings*, 26:123–128, December 2009.

[73] Darren J. Lipomi, Michael Vosgueritchian, Benjamin C-K. Tee, Sondra L. Hellstrom, Jennifer A. Lee, Courtney H. Fox, and Zhenan Bao. Skin-like pressure and strain sensors based on transparent elastic films of carbon nanotubes. *Nature Nanotechnology*, 6:788–792, December 2011.

[74] Aaron P. Gerratt, Bavani Balakrisnan, Ivan Penskiy, and Sarah Bergbreiter. Batch fabricated bidirectional dielectric elastomer actuators. In *Transducers*, pages 2422–2425, Beijing, 2011.

[75] Daniel J. Cohen, Debkishore Mitra, Kevin Peterson, and Michel M. Maharbiz. A highly elastic, capacitive strain gauge based on percolating nanotube networks. *Nano Letters*, 12(4):1821–1825, April 2012.

[76] Xize Niu, Suili Peng, Liyu Liu, Weijia Wen, and Ping Sheng. Characterizing and patterning of pdms-based conducting composites. *Advanced Materials*, 19:2682–2686, 2007.

[77] Phillip Kuhn, Klaus Eyer, Steffen Allner, Dario Lombardi, and Petra S Dittrich. A microfluidic vesicle screening platform: monitoring the lipid membrane permeability of tetracyclines. *Analytical chemistry*, 83(23):8877–8885, 2011.

[78] Leonard Mullins. Softening of rubber by deformation. *Rubber chemistry and technology*, 42(1):339–362, 1969.

[79] David M Siegel, Steven M Drucker, and Inaki Garabieta. Performance analysis of a tactile sensor. In *Proc. IEEE Conf. on Robotics and Automation*, volume 3, pages 1493–1499. Citeseer, 1987.

[80] Alexi Charalambides, Jian Cheng, Teng Li, and Sarah Bergbreiter. 3-axis all elastomer mems tactile sensor. In *Micro Electro Mechanical Systems (MEMS), 2015 28th IEEE International Conference on*, pages 726–729. IEEE, 2015.

[81] Troy A Chase and Ren C Luo. A thin-film flexible capacitive tactile normal/shear force array sensor. In *Industrial Electronics, Control, and Instrumentation, 1995., Proceedings of the 1995 IEEE IECON 21st International Conference on*, volume 2, pages 1196–1201. IEEE, 1995.

[82] JG Rocha, C Santos, JM Cabral, and S Lanceros-Mendez. 3 axis capacitive tactile sensor and readout electronics. In *Industrial Electronics, 2006 IEEE International Symposium on*, volume 4, pages 2767–2772. IEEE, 2006.

[83] Darren J Lipomi, Michael Vosgueritchian, Benjamin CK Tee, Sondra L Hellstrom, Jennifer A Lee, Courtney H Fox, and Zhenan Bao. Skin-like pressure and strain sensors based on transparent elastic films of carbon nanotubes. *Nature nanotechnology*, 6(12):788–792, 2011.

[84] Raymond W Ogden. *Non-linear elastic deformations*. Courier Corporation, 1997.

[85] Anubha Goyal, Ashavani Kumar, Prabir K Patra, Shaily Mahendra, Salomeh Tabatabaei, Pedro JJ Alvarez, George John, and Pulickel M Ajayan. In situ synthesis of metal nanoparticle embedded free standing multifunctional pdms films. *Macromolecular rapid communications*, 30(13):1116–1122, 2009.

[86] Mark D Frogley, Diana Ravich, and H Daniel Wagner. Mechanical properties of carbon nanoparticle-reinforced elastomers. *Composites Science and Technology*, 63(11):1647–1654, 2003.

[87] Zhenchuan Yang, Gang Li, Yilong Hao, and Guoying Wu. Dynamic capacitance extraction of a triaxial capacitive accelerometer. *Int ANSYS Conf*, 2004.

[88] Robert D Howe. Tactile sensing and control of robotic manipulation. *Advanced Robotics*, 8(3):245–261, 1993.

[89] Antonio Bicchi and Vijay Kumar. Robotic grasping and contact: A review. In *ICRA*, pages 348–353. Citeseer, 2000.

[90] Carmel Majidi. Soft robotics: a perspectivecurrent trends and prospects for the future. *Soft Robotics*, 1(1):5–11, 2014.

[91] Rui Li, Robert Platt, Wenzhen Yuan, Andreas ten Pas, Nathan Roscup, Mandayam A Srinivasan, and Edward Adelson. Localization and manipulation of small parts using gelsight tactile sensing. In *Intelligent Robots and Systems (IROS 2014), 2014 IEEE/RSJ International Conference on*, pages 3988–3993. IEEE, 2014.

[92] Stacy J Morris and Joseph A Paradiso. Shoe-integrated sensor system for wireless gait analysis and real-time feedback. In *Engineering in Medicine and Biology, 2002. 24th Annual Conference and the Annual Fall Meeting of the Biomedical Engineering Society EMBS/BMES Conference, 2002. Proceedings of the Second Joint*, volume 3, pages 2468–2469. IEEE, 2002.

[93] Christian Liedtke, Steven AW Fokkenrood, Jasper T Menger, Herman van der Kooij, and Peter H Veltink. Evaluation of instrumented shoes for ambulatory assessment of ground reaction forces. *Gait & posture*, 26(1):39–47, 2007.

[94] Dustyn P Roberts, Jack Poon, Daniella Patrick, and Joo H Kim. Testing pressurized spacesuit glove torque with an anthropomorphic robotic hand. In *Robotics and Automation (ICRA), 2012 IEEE International Conference on*, pages 1520–1525. IEEE, 2012.

[95] Eric V Eason, Elliot W Hawkes, Marc Windheim, David L Christensen, Thomas Libby, and Mark R Cutkosky. Stress distribution and contact area measurements of a gecko toe using a high-resolution tactile sensor. *Bioinspiration & biomimetics*, 10(1):016013, 2015.

[96] Vincent Duchaine, Nicolas Lauzier, Mathieu Baril, Marc-Antoine Lacasse, and Clément Gosselin. A flexible robot skin for safe physical human robot interaction. In *Robotics and Automation, 2009. ICRA'09. IEEE International Conference on*, pages 3676–3681. IEEE, 2009.

[97] Giorgio Cannata, Marco Maggiali, Giorgio Metta, and Giulio Sandini. An embedded artificial skin for humanoid robots. In *Multisensor Fusion and Integration for Intelligent Systems, 2008. MFI 2008. IEEE International Conference on*, pages 434–438. IEEE, 2008.

[98] Yong-Lae Park, Carmel Majidi, Rebecca Kramer, Phillipe Bérard, and Robert J Wood. Hyperelastic pressure sensing with a liquid-embedded elastomer. *Journal of Micromechanics and Microengineering*, 20(12):125029, 2010.

[99] Karsten Weiß and Heinz Wörn. The working principle of resistive tactile sensor cells. In *Mechatronics and Automation, 2005 IEEE International Conference*, volume 1, pages 471–476. IEEE, 2005.

[100] Andreas E Guber, Mathias Heckele, Dirk Herrmann, Alban Muslija, Volker Saile, Lutz Eichhorn, Thomas Gietzelt, Werner Hoffmann, Peter C Hauser,

Jatisai Tanyanyiwa, et al. Microfluidic lab-on-a-chip systems based on polymersfabrication and application. *Chemical Engineering Journal*, 101(1):447–453, 2004.

[101] Kosuke Iwai, Kuan Cheng Shih, Xiao Lin, Thomas A Brubaker, Ryan D Sochol, and Liwei Lin. Finger-powered microfluidic systems using multilayer soft lithography and injection molding processes. *Lab on a Chip*, 14(19):3790–3799, 2014.

[102] Dario Carugo, Jeong Yu Lee, Anne Pora, Richard J Browning, Lorenzo Capretto, Claudio Nastruzzi, and Eleanor Stride. Facile and cost-effective production of microscale pdms architectures using a combined micromilling-replica moulding (μmi-rem) technique. *Biomedical microdevices*, 18(1):1–10, 2016.

[103] Paul Day, Eric V Eason, Noe Esparza, David Christensen, and Mark Cutkosky. Microwedge machining for the manufacture of directional dry adhesives. *Journal of Micro and Nano-Manufacturing*, 1(1):011001, 2013.

[104] Philip N Duncan, Siavash Ahrar, and Elliot E Hui. Scaling of pneumatic digital logic circuits. *Lab on a Chip*, 15(5):1360–1365, 2015.

[105] SW Yan, Matthew M Graff, and Mitra JZ Hartmann. Mechanical responses of rat vibrissae to airflow. *Journal of Experimental Biology*, 219(7):937–948, 2016.

[106] Hee-sup Shin, Alexi Charalambides, Ivan Penskiy, and Sarah Bergbreiter. A soft microfabricated capacitive sensor for high dynamic range strain sensing. In *Intelligent Robots and Systems*. IEEE/RSJ, 2016.

[107] AL Eberle, BH Dickerson, PG Reinhall, and TL Daniel. A new twist on gyroscopic sensing: body rotations lead to torsion in flapping, flexing insect wings. *Journal of The Royal Society Interface*, 12(104):20141088, 2015.